Republic of Iraq
Ministry of Higher Education
and Scientific Research
University of Anbar
College of Engineering
Mechanical Engineering Department

Numerical and Experimental Study of Hydrothermal Performance in a V-Shape Grooved Channels

A Thesis
Submitted to the Council of the College of Engineering - University of Anbar in Partial Fulfilment for the Requirements of the Master Degree of Science in Mechanical Engineering

By

Saif Mohanad Thabit
(B.Sc. in Mechanical Engineering - 2017)

Supervised by

Asst. Prof. Dr. Waleed Mohammed Abed

1442 **2021**

SUPERVISOR'S CERTIFICATION

I certify that this thesis entitled "***Numerical and Experimental Study of Hydrothermal Performance in a V-Shape Grooved Channels***" was prepared by "Saif Mohanad Thabit" under my supervision in the Mechanical Engineering Department / College of Engineering / University of Anbar as a partial fulfillment of the requirements for degree of Master in Mechanical Engineering.

Signature
Name: Asst. Prof. Dr. Waleed Mohammed Abed
Date: / / 2021

In view of the available recommendation, I forward this thesis for debate by the examining committee.

Signature
Name: Dr. Mazin Yaseen Abbood
Head of Mechanical Engineering Department
Date: / / 2021

LINGUIST CERTIFICATION

This is to certify that I have read the thesis titled "***Numerical and Experimental Study of Hydrothermal Performance in a V-Shape Grooved Channels***" and corrected any grammatical mistake I found. The thesis is therefore qualified for debate as far as language is concerned.

Signature

Name: Khaldoon F. Brethee

Date: / / 2021

EXAMINATION COMMITTEE CERTIFICATION

We certify that we have read the thesis titled "***Numerical and Experimental Study of Hydrothermal Performance in a V-Shape Grooved Channels***" and as examining committee examined the student "***Saif Mohanad Thabit***" in relation to all aspects of this thesis. In our opinion, it meets the standards of a thesis for the degree of Master (M.Sc.) in Mechanical Engineering

Signature:
Asst. Prof. Dr. Saad Mohammed Jalil
Date: / / 2021
(Chairman)

Signature:
Asst. Prof. Dr. Hayder Mohammed Jaffal
Date: / / 2021
(Member)

Signature:
Asst. Prof. Dr. Amer Jameel Shareef
Date: / / 2021
(Member)

Signature:
Asst. Prof. Dr. Waleed Mohammed Abed
Date: / / 2021
(Member and supervisor)

Approval of The College of Engineering

Signature
Dr. Mazin Yaseen Abbood
(Head of Mechanical Engineering Department)
Date: / / 2021

Signature
Asst. Prof. Dr. Ameer Abdulrahman Hilal
(Dean of College of Engineering)
Date: / / 2021

DECLARATION

I hereby declare that this thesis, submitted to mechanical engineering department at University of Anbar as a requirement for master degree has not been submitted as an exercise for similar degree at any other universities. I also support this work that is qualified here is entirely my own except for excerpts and summaries whose sources are congruently cited in the references.

Saif Mohanad Thabit

2021

Acknowledgments

First of all, thanks to the great merciful ALLAH who gives me health, strength, and patience to accomplish this study (Alhamdulillah).

I would like to express my deep thanks and sincere gratitude to my supervisor ***Dr. Waleed Mohammed Abed*** *for his assistance, guidance, encouragement, and endless help throughout the steps of this study.*

Sincere thanks are also expressed to the staff of Mechanical Engineering Department / University of Anbar, especially the head of the department ***Dr. Mazin Yaseen Abbood*** *for the encouragement during this work.*

Great thanks to ***my family*** *for the patience and support without them, life would get much more difficult.*

Finally, I would like to thank everyone who helped me directly or indirectly to achieve this study.

Saif Mohanad Thabit

2021

Dedication

To the source of pride and great heath,…My father without your support any of this would have not been achieved.

To the source of love and pure heart,…..My mother

To whom I have beautify by his prayer (God bless you)….My Grandfather

To whom I grew up with her laps and tenderness,….My Grandmother

To those who were their support surrounded me every moment,….My Brothers and sisters

To those who were with me and encourage me,…. My uncles

To whom I carry his name inside me and missing him

To those who have overwhelmed me with their love and devotion, …. My friends.

To everyone who has taught me….

Saif M. Thabit

List of Contents

CHAPTER FOUR: EXPERIMENTAL SETUP

CHAPTER FIVE: RESULTS AND DISCUSSION

CHAPTER SIX: CONCLUSIONS AND RECOMMENDATIONS

List of Figures

List of Tables

Nomenclatures

Symbols	Definitions	Units
a	Groove width	m
A_c	Cross-section area	m^2
A_s	Surface area	m^2
AR	Aspect ratio	----
b	Space among grooves	m
BCs	Boundary conditions	----
C_f	Skin friction coefficient	----
C_p	Specific heat	$J/kg\,.\,^{\circ}C$
d	Groove depth	m
D_h	Hydraulic diameter	m
e	Wide arms of the herringbones	m
$\bar{h}$	Average heat transfer coefficient	$W/m^2.^{\circ}C$
H	Channel height	m
I	Current	Amp
k	Thermal conductivity	$W/m\,.\,^{\circ}C$
L	Length of channel	m
$\dot{m}$	Mass flow rate	kg/s
$\overline{Nu}$	Average Nusselt number	----
P	Pressure	Pa
p	perimeter of rectangular channel	m
q	Heat flux	W/m^2
Q_{in}	Heat source	W
Q_{out}	Heat received by the base fluid	W
Q_{loss}	Heat loss	W
Re	Reynolds number	----
t	Wall thickness	m
T	Temperature	$^{\circ}C$
T_b	Bulk fluid temperature	$^{\circ}C$
T_s	Surface temperature	$^{\circ}C$
$u\,,v\,,w$	Velocity components	m/s
U	Mean velocity	m/s
V	Voltage	Volt
W	Channel Width	m
$x\,,y\,,z$	Cartesian coordinates	m
n	Local coordinate normal to the wall	----

Greek Symbols

Symbols	Definitions	Units
μ	Dynamic viscosity	kg/ m .s
ρ	Density	kg/ m^3
ΔP	Pressure drop	Pa
α	Angle of attack	°
β	Inclination angle of hole	°
θ	Inclined angle	°

Subscripts

av	Average value
f	Base fluid domain
G	Grooved surface
in	Inlet
out	Outlet
s	Solid domain
S	Straight surface

List of Abbreviations

CFD	Computational Fluid Dynamic
FS	Full Scale
FEM	Finite Element Method
FVM	Finite Volume Method
SCH	Straight Channel
B-VGCH	Backward V-shaped Grooved Channel
F-VGCH	Forward V-shaped Grooved Channel
45°-IGCH	45°-Inclined Grooved Channel
PEC	Performance Evaluation Criteria
RP	Rib Pitches
TEF	Thermal Enhancement Factor
SHM	Staggered Herringbone Mixer

Abstract

The convective heat transfer characteristics of fully-developed laminar forced flow in a rectangular channel equipped with inclined and V-shaped grooves have been investigated throughout a combination of numerical and experimental approaches. Three different shapes of grooved channels were systematically tested to measure thermal performance in the range of Reynolds numbers of 100-1000 with an applied heat flux of 15000 W/m^2 on the bottom surface of the grooved channels and using water as a working fluid. A comparison between the experimental and the numerical results was proposed and it showed a good agreement between them and the averaged deviation of skin friction coefficient and average Nusselt numbers for all grooved channels is within 8.73% and 9.13% respectively. The results show that the average Nusselt numbers and the pressure drop in all grooved channels increase with increasing Reynolds numbers according to the straight channel data. For low Reynolds numbers (less than 200), the skin friction coefficient in the grooved channels is approximately less than that of the straight channel. This indicated that the channels with the groove shapes can reduce the friction of flow at a certain level. The F-VGCH has relatively high efficiency of heat transfer rate for different groove depths because of the efficient mixing of fluid as compared with 45°-IGCH and B-VGCH and the peak value of the average Nusselt numbers is 8.98 at *Re = 1000* and groove depth 3.5 mm. The 45°-IGCH shows a significant enhancement in heat transfer at high range of Reynolds numbers with reasonable penalty of pressure-drop. Finally, the use of F-VGCH offers the highest value of the *PEC* as compared with the other shapes of grooved channels and the peak value of *PEC* is 2.244 at *Re* = 600 and groove depth 3.5 mm.

CHAPTER ONE
INTRODUCTION

CHAPTER ONE
INTRODUCTION

1.1 Background:

The conversion, employment, and recovery of energy in every commercial, industrial, and domestic applications involve a heat transfer process. Recently, the rising demand for high thermal efficiency devices has led researchers to look for techniques to boost heat transfer. For this purpose, researchers divided enhancement techniques into two main categories namely, *active* techniques and *passive* techniques.

Active improvement techniques are required to add external power such as, DC or AC electrostatic fields, acoustic fields, vibration of surface at either high or low frequencies, removal or suction of vapors in nucleate boiling and mechanical aids. While, in passive improvement methods for instance, extended and coated surfaces, ridges in the form of ribs and grooves, devices of swirl flow and treated or roughed surfaces, external power is not required.

In many engineering applications, passive technologies are preferred because of the concerns about safety, cost, noise and reliability that are associated with the active technologies. It is possible to combine two or more enhancement techniques from the active and passive methods and so called "*hybrid techniques*", which can lead to better enhancement in heat transfer [1]. Several procedures have been adopted for promoting and augmenting of heat transfer such as, increased surface area either by using extended surfaces or manipulating of the channel shapes from straight to wavy or curved shapes [2]. The use of grooves or ribs in the channels is deemed one of the most successful techniques.

The flow in small channels is usually laminar (relatively small Reynolds number) because of the dominance of viscous forces in the fluid flow [3]. However, the rate of heat transfer in these small-diameter passages is always associated with a high penalty of pressure-drop for fluid flow. Many researchers [4-10] have recently reported an improvement in the laminar forced convection heat transfer. Roughened surfaces such as rib, groove, and helical rib have been used to disrupt the flow and provide transverse/longitudinal vortices or three-dimensional mixing to augment heat transfer in heat exchangers. The ribbed/ grooved channels have been studied in a variety of geometric shapes and arrangements by many researchers. Many types of ribbed-grooved channels were used in many engineering applications, including cross-flow heat exchanger, gas turbine airfoil cooling design, and solar air heater blade cooling systems. Grooved/ ribbed channel flow is also used in many practical applications such as, air conditioning systems, cooling system in electrical and electronic components, computer chips, biomedical devices, steam condenser, high-performance aircraft gas turbine engines, solar heater, and heat exchangers [11].

1.2 Flow in Patterned-Grooved Channels

In general, patterned-groove channel utilizes the grooves on one side of the channel to produce transverse components and thereby enlarge the fluidic interface to improve mixing. Fluid is directed to move onto the bottom of the main channel by grooves on one side (bottom grooves), which resulting in a relatively weak helical motion with a long pitch for each cycle, as illustrated in Figure 1 (a) [12]. As a result, the concept of connected grooves was introduced, which used grooves on the bottom and sometimes on the sides of the channel to initiate the fluid mixing. Connected grooves are composed of bottom grooves and sidewall grooves that are conjoined around neighboring walls, as seen in Figure 1 (b) [12].

The fluid is directed from the bottom grooves around the sidewall grooves to the top of the main channel and then flows into the main stream. According to this flow pattern, a helical flow with a short pitch and an extreme transverse field will be generated.

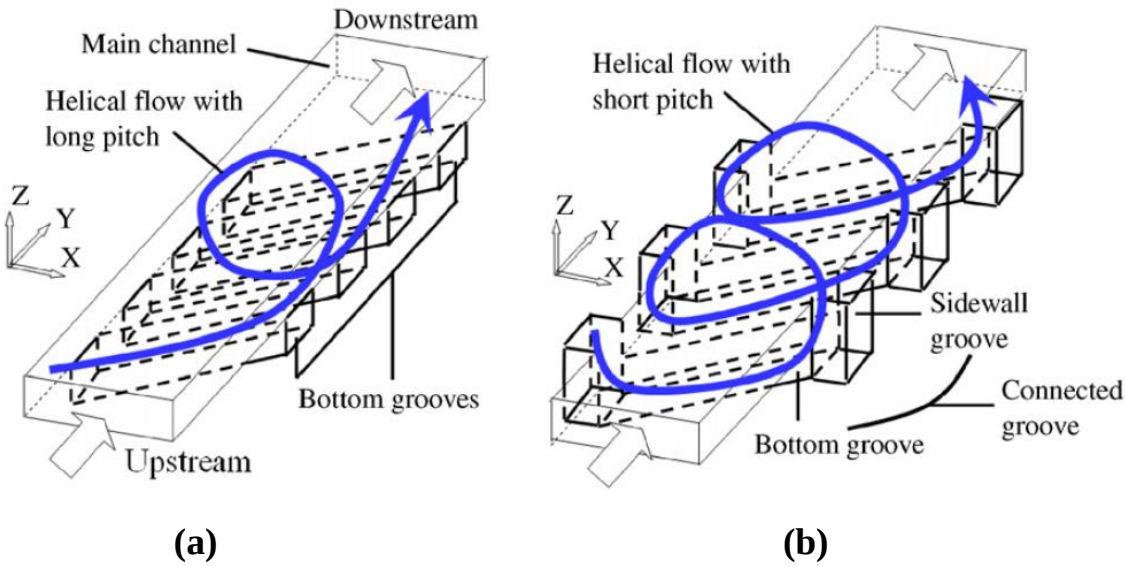

Figure 1.1: Schematic of the flow features within patterned-grooved channels [12]

Previous numerical investigations for flow inside the staggered herringbone channel have revealed particle pathline plots with a small scale helical motion directly across the patterned grooves [13]. It is important to show that the fluid flow inside the grooves is oriented toward the channel walls has a viscous influence on the fluid flow directly over the grooves, while the flow between the grooves (over the ridges) has a viscous influence on the fluid flow in the opposite direction. Therefore, the fluid directly over the ridges tends to prevent overall non-axial fluid transport in the grooves, and reduce the total amount of helical flow inside the channel[14,15].

1.3 Secondary Flows

In cases where there is a three dimensional flow field, the flow is often regarded as comprising two components, a primary flow and a secondary flow. The primary flow is parallel to the main direction of fluid motion and the secondary flow is perpendicular to this. Such flows are commonly produced by the effect of drag in the boundary layers, and some of the more important situations in which such flows arise are discussed here[16].

Secondary flows occur where there is a flow around a bend in a pipe and this is illustrated in Figure 1.2 (a). At the bend, there is a transverse pressure gradient, which provides the centripetal force for the fluid elements to change direction. However, the pressure gradient required for the faster moving fluid near the center of the pipe to follow the curve of the bend is greater than that required for the slower moving fluid near to the wall. This results in the fluid near the center of the pipe moving toward the outside of the pipe and the fluid near the wall moving inwards. Another common situation in which secondary flows arise is in spinning fluids, for example, in a weather system or a stirred teacup. In these systems, there is a balance between the radial pressure gradient and the centrifugal force. However, near a boundary, drag on the fluid leads to a lower velocity and the centrifugal force can no longer balance the pressure gradient. This results in a secondary flow of the fluid in the radial direction. Figure 1.2 (b) illustrates this for the case of a cyclonic weather system[17, 18].

Turbulent flows through pipes or channels of noncircular cross-section also give rise to secondary flows. There is a movement of fluid away from the corners along the walls and a movement toward the corners near the bisector of the comer. Examples for rectangular and triangular channels are shown in Figure 1.2 (c). This phenomenon is known as "secondary

flow of the second kind" [19, 20]. There is also a "third kind" of secondary flow which results from oscillations in a stationary fluid. These oscillations may be due to, for example, an oscillating body or ultrasonic waves. If there is a variation in the amplitude, as will be the case with standing sound waves, then a secondary flow is induced which moves in the direction of decreasing amplitude.

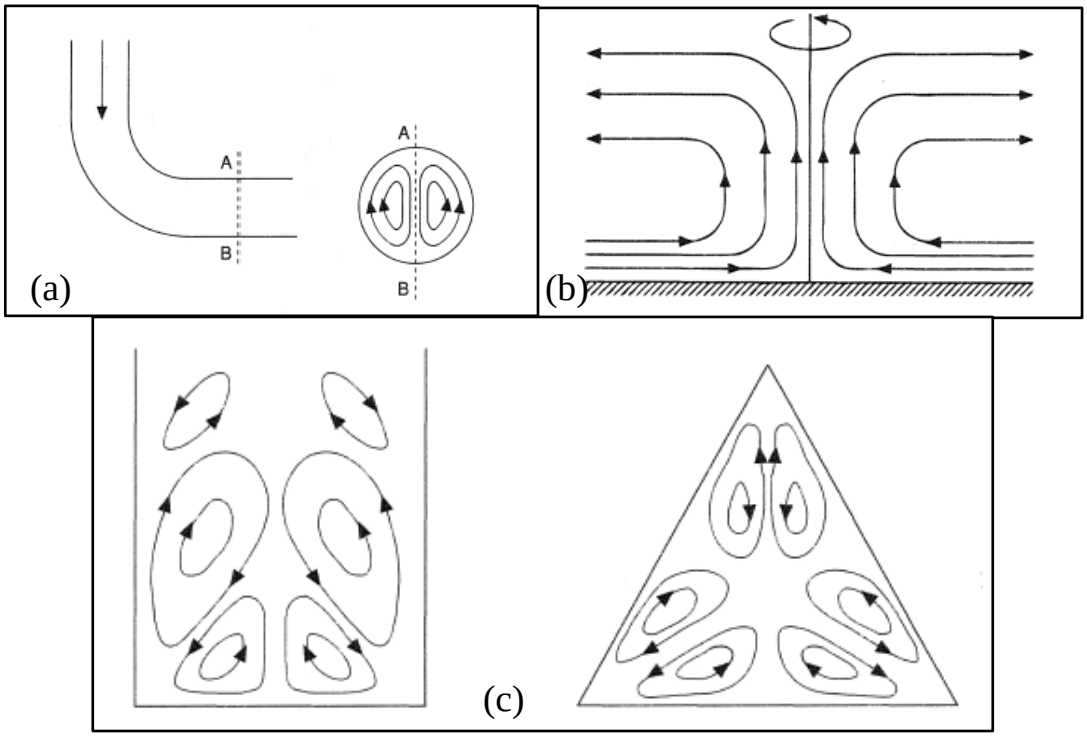

Figure 1.2: Secondary flow (a) around a bend, (b) in a cyclone, (c) in channels [16]

Herringbone or ridge structure (passive derivative mixers) was first introduced to rapidly mix flowing fluids in a straight microchannel with the absence of turbulence and inertial effects at low Reynolds number (Re < 1) (Stokes flow). Stroock et al.[21] presented the pioneering microchannel with ridges placed on the top floor at the oblique angle of 45°, and they found that the transverse secondary vortices were generated due to the steady axial pressure gradient. The generated twisting flow was also observed to be independent of Re in Stokes flow regime. They successfully demonstrated that the Staggered Herringbone Mixer (SHM)

with ridged topography could realize effective microfluidic mixing at Re between 0 to 100. Different patterns of secondary flow have been observed including single ellipse shape vortex, asymmetric double vortices and Dean-like vortices. Through experimental studies, parameters of cross-sectional aspect ratio, groove- or ridge-pattern style, amplitude ratio between two layers' heights and flow rate have shown effects on the geometry-induced secondary flow[22].

1.4 Problem Statement:

Several methods for enhancing fluid mixing based on inertia instabilities (creating chaotic flows) have been reported and demonstrated in small-scale channels. However, more experimental and numerical investigations are needed in order to understand and improve the thermal performance of these channels. To enhance the heat transfer in these channels by generating transverse flows (secondary flows), inclined and V-shape grooves (staggered herringbone) are printed on the bottom wall of the channel at an oblique angle with respect to the long axis of the channel. Therefore, the fluid mixing will be enhanced and hence improve thermal performance.

This work has numerically and experimentally addressed the convection heat transfer for hydrodynamically fully-developed and thermally developing laminar forced flow within rectangular grooved channels. In particular, the grooves were formed on the bottom wall of the channel and heated from its bottom at a constant uniform heat flux. The key goal of the current analysis is to analyse the flow and the heat transfer characteristics of the grooved channels numerically and experimentally by using ANSYS FLUENT 2020R1[23].

A large amount of friction and heat transfer data, for different arrangement and heights of rectangular shape grooves have been simulated for flow with Reynolds numbers ranged between 100 and 1000.

1.5 Aim and Objectives of Current Research

The aim of this research is to experimentally and numerically study the performance of fully-developed and thermally developing laminar forced convection heat transfer within a V-shape and inclined grooved channels using water as a working fluid.

The objectives of this research are to fill the gap in the literature towards accomplishment of a patterned-groove channel for practical applications that demand reasonable fluid mixing in the channel under laminar flow regime. To achieve this goal, the following specific objectives will be attempted:

1. To evaluate the fluid flow behaviour and heat transfer characteristics through straight channel [SCH], Forward/backward V-shape grooves channel [F/B-VGCH], and inclined grooves channel [45˚-IGCH].
2. To study numerically and experimentally the effect of arrangement and shape of the grooves (Forward/backward V-shape grooves and Inclined grooves) on the flow and thermal fields.
3. To setup an experimental test for analysing the performance of convection heat transfer within a V-shape grooved channel and to validating the numerical simulation model.
4. To investigate the effect of geometric groove parameters such as, groove depth on the fluid flow behaviour and heat transfer characteristics as well as the performance evaluation criterion.

1.6 Outline of the Thesis

Basically, this thesis involves six chapters and each chapter will be briefly introduced as follows:

- ✓ **Chapter one** defines the main applications of fluid flow through grooved channels and gives a background of the research problem statement with the aim and objectives of the current study.
- ✓ **Chapter two** presents a review of the prior published relevant studies that focused on enhancing fluid mixing and heat transfer performance.
- ✓ **Chapter three** deals with the description of numerical simulation such as research approach, computational model description, conservation equations and boundary conditions, grid independence test, solution method and solving procedure.
- ✓ **Chapter four** presents experimental setup such as test rig description, measurement instruments, experiment test procedure, acquiring data, and uncertainty analysis.
- ✓ **Chapter five** presents a verification of the developed numerical model and compare the numerical and experimental results that investigate the effect of grooves on the flow characteristics, heat transfer, and performance evaluation criterion. It also presents numerical results for the effect of groove shape and groove depth on the characteristics of flow and heat performance.
- ✓ **Chapter six** provides the main conclusions of the current study and highlights some suggested recommendations for the future studies.

At last, references, which are cited in this study, are listed.

In addition, appendixes A, B, and C are added to explain the calibration of measuring instruments, uncertainties analysis procedure, and code program of measuring instruments, respectively. A methodology flow chart of this research is presented in Figure 1.3.

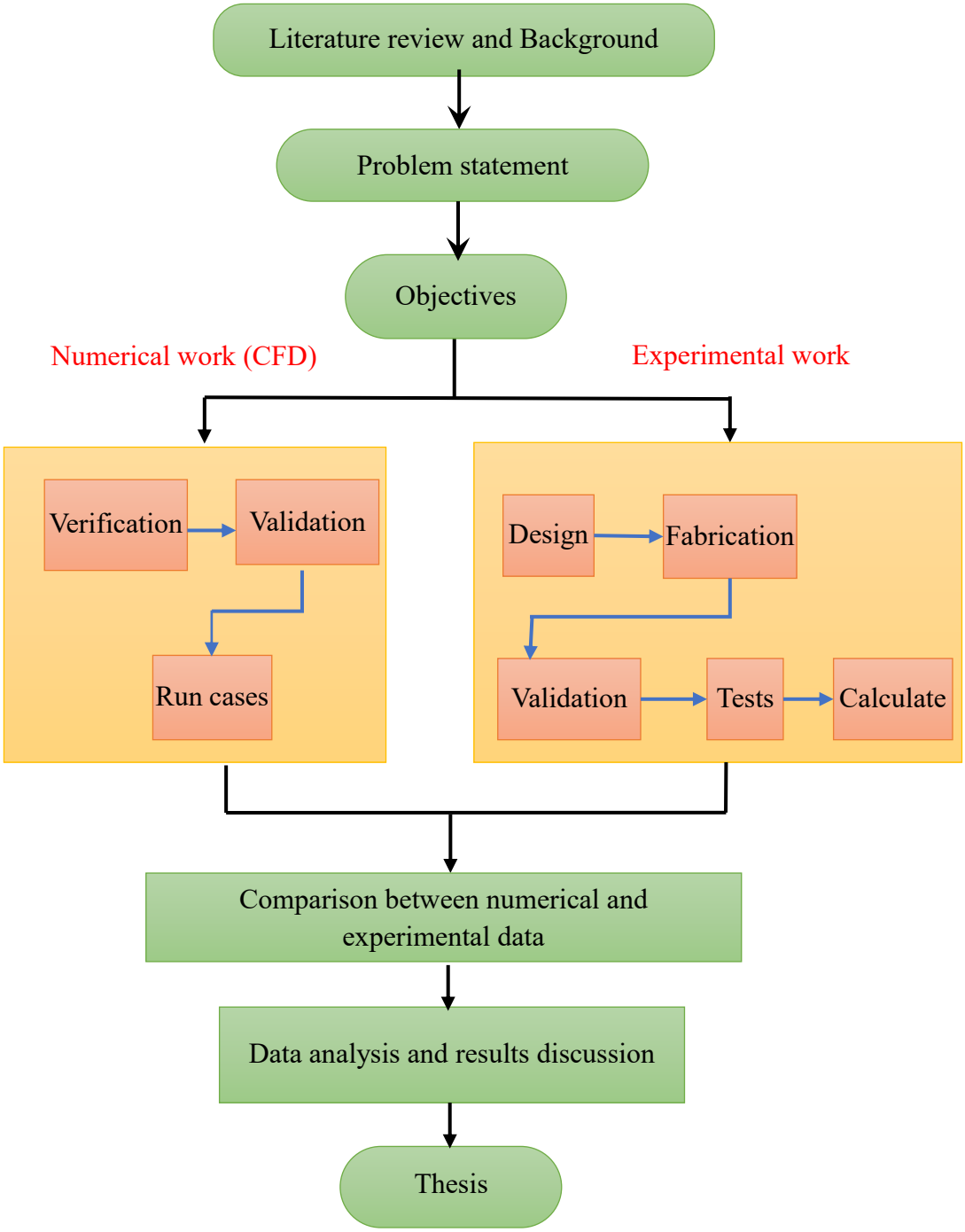

Figure 1.3: Flowchart of thesis structure

CHAPTER TWO
LITERATURE REVIEW

CHAPTER TWO
LITERATURE REVIEW

2.1 Introduction

This chapter outlines the previous studies on fluid flow and heat transfer characteristics using a variety of passive techniques such as fins, dimples, ridges, ribs, and grooves. The first section reviews the experimental and numerical studies for the passive surface modifications of heat transfer and fluid flow in various shapes of channels. The second section focuses on the numerical and experimental studies for the passive surface modifications by employing V-shape and inclined groove shapes to enhance mixing of fluid flow while the third section focuses on the numerical and experimental for improve heat transfer using V-shape and inclined grooves.

2.2 Passive Surface Manipulations for Enhancing Heat Transfer

This section concentrates on the previous works that are related to the heat transfer enhancement based on the main passive techniques. Farhanieh et al. [4] experimentally and numerically studied the heat transfer characteristics of laminar fluid flow in a channel with rectangular grooves on its wall. The surface of the grooved wall was heated and kept at a uniform temperature with Reynolds numbers ranging from 100 to 1760. The governing equations were numerically solved by a Finite Volume Method (FVM). Their results indicated that there is an improvement in the local Nusselt number as compared with the corresponding straight channel due to the destruction of thermal boundary layers and the formation of re-circulating flows within the grooves. They also reported that the heat transfer improvement was accompanied by an increase in the pressure drop.

Yutaka et al. [5] numerically investigated the characteristics of heat transfer and the fluid flow behaviour in a corrugated duct with round corners. The numerical analysis was performed for three different corrugation angles (45˚, 30˚, and 15˚) and Prandtl number of 0.7 under a range of Reynolds number between 100-1000. Only a single wave was considered in this study based on the assumption of thermal conditions and periodic flow. For both sharp and round corners in the corrugated channel, the pressure drop was found to be greater than that of straight channel. Moreover, for corrugated duct with round corners, the pressure drop was 80% lower than that of corrugated ducts with sharp corners for 1000 Reynolds numbers. Additionally, Sundén and Sköldheden [24] performed an experimental study to investigate the hydrothermal performance of smooth and trapezoidal-corrugated channels. The upper and lower channel walls were heated using oil baths at a uniform surface temperature. In their experiments, air was used as a working fluid and the range of Reynolds numbers varied from 800 to 5000. The experimental results revealed that the enhancement ratio of the heat transfer increased by a factor of 3.5 and the penalty of pressure-drop increase by a factor of 5 to 6 as compared with those for smooth channel.

Other numerical work was achieved by Webb and Ramadhyani [6] to investigate the characteristics of heat transfer and the behaviour of fully-developed laminar fluid flow through a parallel plates channel fitted with staggered transverse ribs under constant heat flux along both parallel walls. The influence of rib height to height of channel was analyzed in the range from 0.0625 to 0.375, and the rib spacing was varied from 0.5 to 2.0 with the range of Reynolds numbers between 340 to 2000. Their numerical results showed that significant augmentation of convection heat transfer was obtained for fluids with a high Prandtl number such as, water or fluorocarbons, due to lateral redistribution of energy flow with relatively

low friction factor. Furthermore, Kelkar and Patankar [7] conducted a numerical study of hydrothermal performance within a two-dimensional parallel plates channel equipped with staggered baffles. The parallel plates were kept under constant temperature boundary conditions. The streamwise periodic difference of the cross-sectional area causes the flow and temperature fields to duplicate periodically after the developing length. The study was fulfilled for various values of the Prandtl number, the Reynolds numbers, geometric parameters and the fin-conductance parameters. The fins were found to significantly deflect the flow and impinge upon the opposite wall surface with a noticeable raise in the performance of heat transfer. However, the associated rise in the pressure drop magnitude was greater than the rise in the heat transfer.

Huang et al. [8] carried out experimental and numerical investigations on the characteristics of pressure-drop and the improvement of heat transfer for laminar pulsatile flow in a grooved channel with different groove lengths. Five configurations of grooved channels were tested with a wide range of non-dimensional groove lengths (1.6, 2.4, 3.2, 4.0 and 4.8). The experimental and numerical results showed that the best heat transfer enhancement in the grooved channel occurred at the groove length of 1.6, whilst the mean plenty of pressure-drop at 1.6 was comparatively less than the other studied grooved channels.

Moreover, Ridouane and Campo [9] numerically analyzed the heat transfer and pressure drop characteristics of laminar air flows in a parallel plate channel with transverse hemi-cylindrical cavities. Two cavity configurations were studied, one with symmetrically opposing cavities onto the upper and bottom walls, another with non-symmetric or staggered cavities onto the two parallel walls. A 1200 mm long channel contains two series of 3, 6, and 12 transverse cavities having ratios of cavity depth to cavity print diameter of 0.125, 0.25, 0.375, and 0.5. Reynolds numbers

based on the hydraulic diameter ranged from 1000 to 2500. Their results showed that the relative heat transfer was increased by 30% as compared with the smooth surface while pressure loss increased by 19%.

Lafta [10] numerically investigated laminar flow and heat transfer through a rectangular channel with different obstacles configurations. The obstacles were arranged alternately on the lower and upper walls of the channel. Air was selected as a working fluid and the range of Reynolds numbers varied from 100 to 700, under a constant heat flux. The numerical results indicated that the obstacles have a clear effect on the enhancement parameters of the fluid flow and heat transfer rate. The results showed that as the number of obstacles increases, the heat transfer was more improves. Using of rectangular obstacles raises the heat transfer rate for every Reynolds number tested higher than the other types.

Herman and Kang [25] experimentally investigated the behaviour of fluid flow and heat transfer performance in grooved channels with curved vanes using holographic interferometry. The experimental result clarified that the heat transfer was risen by a factor of 1.5 - 3.5 due to increase in the flow velocity in the grooved region when compared with the basic grooved channel. Moreover, the pressure drop was found to be 3-5 times higher than that for the basic grooved channel.

Eiamsa-ard and Promvonge [26] carried out an experimental study to analyze combined effects of rib-grooved tabulators on the turbulent forced convection heat transfer and friction characteristics in a rectangular channel under a uniform heat flux boundary condition. Three different types of rib-groove arrangements and three pitch ratios were examined (rectangular-rib and triangular-groove (RR–TG), triangular-rib and rectangular-groove (TR–RG), and triangular-rib with triangular-groove (TR–TG)). Channel measurements were executed for aspect ratio, AR =

W/H = 20 and channel height, *H* = *9* mm , with rib height = *3* mm at three pitch ratios = 6.6, 10 and 13.3 at Reynolds number range from 3000 to 10,000. The experimental results showed that all rib-groove arrangements were significantly enhanced the heat transfer rate in comparison with the smooth channel. The rib-groove turbulator with PR=6.6, 10, and 13.3 for the TR–RG can increase the heat transfer up to 80%, 60%, and 46%, respectively. The results showed that using Triangular-Rib with a Triangular-Groove shaped (TR–TG) gives the highest values of thermal enhancement obtained for all pitch ratios at a constant pumping power.

2.3 V-shaped and Inclined Grooves for Augmenting Fluid Mixing

This section focuses into the use of V-shaped and inclined grooves for fluid mixing enhancement that has been considered by previous researches. Stroock et al. [21] presented a pioneered experimental study for testing the effect of V-grooved and inclined ridges on fluid mixing by using two different passive designs. The first mixer design included diagonally slanted grooves whereas the second mixer design involved staggered V-grooved (herringbone) ridges that printed on a bottom wall of rectangular channel in order to augment the efficiency of fluid mixing. They reported that these passive mixers were capable for promoting helical fluid motion with widening the interfacial surface area and enhancing the mixing process. In addition, these different structures of grooved mixers (slanted grooves and V-groove transverse ridges) are capable of performing efficient mixing at relatively low *Re* ($0 < Re < 100$). Therefore, it was concluded that both diagonal mixer and staggered herringbone mixer possess mixing performance better than a channel without grooves owing to generate chaotic flow and short mixing lengths.

In 2004, Stroock and McGraw [27] developed an analytical model of a 3D staggered herringbone mixer in which the cross-section of the channel is

treated as a lid-driven cavity flow. They stated that this model was able to reproduce the advection patterns that were experimentally observed in their tested flow with the same dimensions of Stroock [21]. The analytical model is adopted to investigate the quality of the fluid mixing in the flow as a function of the groove geometry.

In addition, other numerical investigation has been conducted by Lynn and Dandy [28] to study the efficiency of fluid mixing in a micromixer with grooves and its dependence is based on ridge length, groove depth ratio, and channel aspect ratio. The investigation included over 700 cases, which detailed the quantity of helical flow across unsymmetrical patterned grooves in the slanted or inclined grooved micromixer for forming staggered herringbone mixer. A three-dimensional CFD models were developed to simulate velocity fields through planar slanted and staggered herringbone devices by employing a commercial software package FLUENT-CFD. The optimized groove geometries were shown to have a large dependence on the channel aspect ratio, the groove depth ratio, and the ridge length. The change in the geometric parameters of the mixing channel caused a variation in the transverse advection flow to be as large as 50%.

Sabotina et al. [29] experimentally and numerically studied the optimization design of a bottom grooved micromixer. The optimization was performed using CFD numerical simulations for solving incompressible Navier-Stokes equations and convection-diffusion equations. The design of mixer geometry was fitted with staggered herringbone grooves. The grooves were patterned at 45° angle with the *x*-axis and the asymmetry index of the staggered herringbone groove, which was one-third of the channel width. The magnitude of the average transversal flow velocity after one groove was used to develop a basic new optimization criterion. The numerical simulation of flow was

experimentally validated and a good agreement was found between the experimental and numerical results. Various designed prototypes were compared with the original design of staggered herringbone mixer. The results showed that adding just six grooves to the bottom of the microchannel can improve the mixing performance and the suggested design of grooved geometries could be much easier to be fabricated by micro-engineering technologies.

Recently, Kwak et al. [30] have experimentally and numerically examined the impact of staggered herringbone grooves on the fluid mixing of laminar flow regime. Both negative (with ribs) and positive (with grooves) staggered herringbone patterns were tested to investigate the effect of the rib and groove geometry structure on the flow behaviour. Furthermore, the influence of flow directions (forward and backward) on the fluid mixing of laminar flow regime was also studied. The numerical simulation was performed using COMSOL Multiphysics, which based on the finite element method (FEM), to solve incompressible fluid flow by Navier Stokes equations and convection-diffusion equations. The results of both numerical and experimental work specified that the positive staggered herringbone pattern was more efficient in fluid mixing than the negative pattern. Also, the forward direction flow illustrated higher mixing efficiency than the backward direction flow with negative pattern.

2.4 V-shaped and Inclined Grooves for Enhancing Hydrothermal Performance

This section presents the previous published work that related with V-shaped and inclined grooves for enhancing heat transfer. An experimental investigation has been performed by Taslim et al. [31] for testing the influence of inclined, V-shaped, and discrete ribs attached on two opposite sides of the duct on heat transfer and flow characteristics. Thirteen rib

geometries representing three blockage ratios in a practical range and four different configurations were tested in the range of Reynolds numbers from 5000 to 30000. The results showed that the V-down ribs at relative roughness height (e/D = 0.0833) produced the highest heat transfer coefficient among all the investigated rib geometries. Maximum thermal performance was reported for straight ribs at rib angle of attack ($\alpha = 45°$) with a blockage ratio of 0.125.

Promvonge and Kwankaomeng [32] investigated the characteristics of periodic laminar flow and heat transfer within a horizontal (with channel aspect ratio = 2) channel fitted with 45° V-shaped baffles in tandem, staggered arrangements on two opposite channel walls. The numerical results illustrated that thermal enhancement factors were much higher than unity and the maximum values were in a range of 2.6–2.75 indicating higher thermal performance over the smooth channel.

Experimental measurements and numerical simulations have been executed by Peng et al. [33] in order to investigate the convection heat transfer with different types of ribs in a rectangular channel. Six configurations of ribs are tested (90° continuous rib, 90° interrupted rib, 45° V-shaped continuous rib, 45° V-shaped interrupted rib, 60° V-shaped continuous rib, and 60° V-shaped interrupted rib). Their findings observed that the V-shaped ribbed plate provided greater thermal and hydraulic performances than the 90° ribbed plate because it was not only disrupting the boundary layer but also produced secondary longitudinal vortices, which caused an enhancement of heat transfer. Also, a comparison of continuous and interrupted ribs showed that the heat transfer with the V-shaped interrupted ribs was lower than with the V-shaped continuous ribs, while the 90° ribs had the opposite result. Promvonge et al. [34] presented a numerical investigation on laminar flow and heat transfer characteristics in three-dimensional isothermal walls square-channel fitted with inline

45° V-shaped baffles on two opposite walls. Air was used as a working fluid and the range of Reynolds number was between 200 and 2000. The inline V-baffles with its V-tip pointing downstream and the attack angle (or half V-apex angle) of 45° relative to the flow direction were mounted repeatedly on the lower and upper walls. The counter-rotating V-baffle longitudinal vortex flows were apparently caused attachment and impingement flow over the walls, leading to an increase in heat transfer over the test section. Additionally, they pointed out that the V-baffle with pitch ratio PR = 1.5 and blockage ratio BR =0.2 produce the maximum Thermal Enhancement Factor (TEF) about 3.8, while the enhancement of Nusselt number was around 14 times above the smooth channel at higher Reynolds numbers.

Numerical study of fluid flow and heat transfer in a two-pass square channel equipped with different rib configurations was reported by Ravi et al. [35]. Thermal-hydraulic performance of four different rib geometries namely, 45°- inclined , V- shaped, M-shaped and W-shaped rib, was tested. The rib height to channel hydraulic diameter ratio and the rib pitch to rib height ratio were 0.125 and 16, respectively, and Reynolds numbers varied from 20,000 to 70,000. The result showed that the heat transfer enhancement offered by V-shaped ribs was 7% higher than 45°- inclined ribs, 35% higher than M-shaped ribs and 28% higher than W-shaped ribs. Although, the pressure drop for V-shaped ribs was 19% higher than 45°- inclined ribs, 24% higher than W-shaped ribs and 28% higher than M-shaped ribs. Jedsadaratanachai and Boonloi [36] reported numerical investigations for laminar forced convection heat transfer and fluid flow behaviours in a square channel with inline 30° double V-baffles vortex generator placed on both two opposite walls of the channel. The investigation including the effects of blockage ratios (BR=0.05–0.25), and pitch ratios (PR=1–2), with Reynolds numbers ranging between 100

to1200. They summarized that the maximum thermal performance was around 3.2, which is found at blockage ratio, pitch spacing ratio, and Reynolds numbers of 0.10, 1, and 1200, respectively.

Promvonge and Skullong [37] experimentally investigated the influence of combined turbulence promoters on forced convection and fluid flow resistance in a solar air heater duct with combined punched-V-ribs and chamfer-V-grooves with Reynolds numbers 5,300-23,000. The rib parameters had three relative rib-pitches (RP = 1.0, 1.5 and 2.0), three inclination angles (β = +45°, 0° and -45°) of rib-punched holes having a single relative rib height or blockage ratio, RB = 0.5. The groove parameters included three relative groove-pitch lengths (RP = 1.0, 1.5 and 2.0) similar to the V-rib case. The maximum thermal performance factor was around 2.47 (at β = 45° and RP = 1.5), where Nusselt number and friction factor were increased by 6.52 and 38.67 times over the smooth duct.

Jansangsuk et al. [38] experimentally studied heat transfer and pressure drop characteristics in a rectangular channel fitted with periodic triangular V-pattern ribs. The ribs were tested for pointing downstream (V-down) to the flow. The tested channel possessed 30 mm height, the rib to channel height = 10, 0.1, 0.2, and 0.3, the rib pitch to channel height = 3 and 4, the attack angle of 30° relative to the flow direction. Air was used as a working fluid and the Reynolds number range varied from 5000 to 20000. The results showed that enhancement in Nusselt numbers and friction factor were reported to be 3.5 and 11.49 times higher than that for a flat plate at rib to channel height = 0.4 and pitch to channel height = 3. The maximum thermal performance and mean thermal performance values were observed to be 1.75 and 1.53 for rib to channel height = 0.4 and rib pitch to channel height = 3, respectively.

Leung et al. [39] conducted an experimental investigation of heat transfer and pressure drop characteristics in a horizontal triangular sectional channel with V-grooves. These channels have the same axial length and hydraulic diameter, which were made from duralumin alloy. The inner surfaces of each channel were either flat or machined with V-grooves uniformly spaced. These grooves had a depth of 1 mm for each examined channel and all had the same apex angle ($0° \leq \theta \leq 150°$). The uniform separation was constantly kept at 34 mm between the centre lines of two adjacent V-grooves. The entire inner wall of the channel was uniformly heated, while its outer surface was thermally insulated and the Reynolds number of the flow was within the range of 2800 to 9500. The optimum value of Nusselt number was obtained for groove apex angle between 15˚ and 18˚ and the maximum frictional factor was observed at higher value of groove apex angle order of 110.

Promvonge et al. [40] experimentally studied the thermohydraulic behavior of a channel enhanced with the V-shaped and chamfered V-grooved ribs. Air as the test fluid flowed through the channel for Reynolds number ranging from 5300 to 23,000 under constant heat flux on the top wall. The variable parameters included the rib pitch and rib height, whereas the attack angle of the ribs was considered 45°. The results indicated that using smaller rib pitch and larger rib height accelerates both frictional loss and heat transfer rate. The maximum TEF around 1.907 is found for the combined rib-groove at Rib blockage ratio equal to 0.4 and a Relative rib/groove pitch ratio equal to 1.5.

Alam et al. [41] experimentally investigated heat transfer augmentation using V-shape perforated blockages machined on a uniform heat flux heated surface over a range of Reynolds numbers from 2000 to 20000. Perforated blocks were offered higher secondary flow levels that facilitate turbulent mixing with the main flow. Experimental results indicated that

33% enhancement was observed in Nusselt numbers while the friction factor decreased by 32% for perforated blocks as compared with the solid blocks. Also, they reported that the enhancements were around 6.76 and 28.84 times higher than the smooth channel for the Nusselt number and friction loss, respectively. They spotted that the maximum enhancement of Nusselt number occurred at a relative blockage height of 0.8 and the maximum friction factor was at a relative blockage height of 1.0. Later on, the rate of heat transfer, pressure-drop penalty, flow instabilities, Critical Heat Flux (CHF) and flow patterns were experimentally studied by Yang et al. [42]. They studied a rectangular microchannel involved 7 cycles with 12 staggered herringbone grooves to form four different configurations of staggered herringbone mixers. The experimental findings mentioned that single- and two-phase heat transfer rate and CHF were augmented up to 221%, 160%, and 61%, respectively in microchannel utilizing micro-scale staggered herringbone mixers compared with a plain-wall microchannel. Additionally, the location and coverage of the micromixers possess significant effects on the single- and two-phase heat transfer in the microchannels.

In other experimental work, the enhancement of heat transfer caused by herringbone micro-structure ridges in microfluidic channels was quantified by Marschewski et al. [43]. Three different configurations of flow promoters in the tested microchannels (symmetric herringbones promoters, symmetric herringbones plus solid ridge in the centre, symmetric herringbones plus vacant center zone) were utilized for illustrating the effect of these flow promoters on the heat transfer augmentation. Micron-resolution laser induced fluorescence (μLIF) and on-chip resistance thermometers were employed to quantify the temperature of streamed fluid and channel surfaces, respectively. Their experimental results indicated that because of the efficient triggering

helicoidal motion of fluid particles, a considerable thermal performance enhancement of 220 percent at Reynolds number 350 was obtained using herringbone flow promoters compared with a straight smooth microchannel at the same pumping power. In spite of the difficulty of manufacturing the staggered herringbone mixers in fluid cooling systems into micro-scale, a four-fold increase in thermal performance enhancement compared to a smooth channel was achieved.

Lee and Teo [44] have numerically investigated the effects of inclined grooves on the wall of the rectangular microchannel. They induced the flow to swirl by adding additional components to the otherwise laminar flow. Constant heat flux boundary condition was applied in this study. The heat transfer was found to enhance and rise up to 12% without incurring substantial additional pressure drop.

2.5 Summary of Literature Review

Great efforts have been carried out by various researchers for passive heat transfer enhancement techniques using various shapes of passive surface modifications like, ridges, ribs, and grooves. The following points are raised from the previous comprehensive literature survey:

1. Heat transfer inside flow passages can be enhanced by using passive surface modifications such as, ridges, ribs and grooves due to an increase in the fluid mixing by vortex stretching and chaotic advection.
2. Various heat transfer enhancement techniques have different advantages and limitations. They can be achieved based on using varying geometrical configurations and construction complexity while operating under different flow and thermal conditions.
3. The majority of the previous studies were focused on the fluid mixing process with using V-shaped grooves and inclined grooves.

The other studies focused on heat transfer enhancement for turbulent flow regime. However, few experimental and numerical studies were performed for studying the heat transfer enhancement for laminar flow.

2.5. Scope of The Current Study

The scope of the current study is as follows:

1. The flow is varied with Reynolds number of (*Re* = 100, 200, 400, 600, 800, 1000) (6 cases).
2. The formed V-shape grooves are (Forward / Backward -Staggered herringbone) and the inclined grooves was formed at inclined angle of ($\theta = 45°$).
3. The working fluid is water and the channel material is aluminum.
4. The channel is designed with height (*H = 0.01 m*), width (*W = 0.02 m*), length (*L = 0.3 m*) and the thickness of its bottom plate (*t = 0.006 m*)
5. Number of cycle = 5 (5 grooves in each cycle).
6. Depth of grooves (*d = 1.5, 2.5, 3.5 mm*).
7. Space among grooves (*b = 0.005 m*) and groove width (*a= 0.005 m*).

The V-shape grooves (Staggered herringbone) and ratio of these parameters chosen according to reference [21] as shown in Figure 2.1.

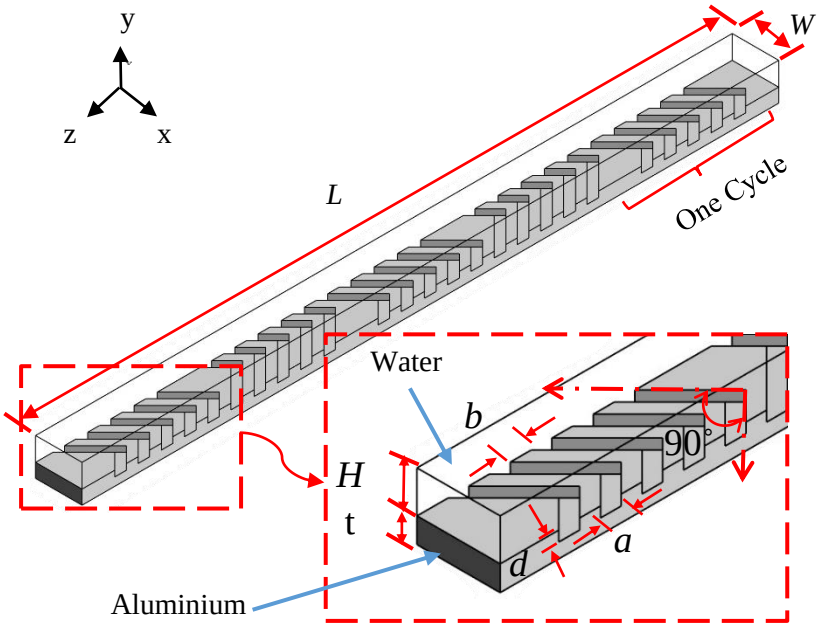

Figure 2.1: Physical geometry of the current study with details

CHAPTER THREE

NUMERICAL SIMULATIONS

CHAPTER THREE
NUMERICAL SIMULATIONS

3.1 Introduction

This chapter includes of the following sub-sections: Research approach, description of computational model, conservation equations and assumptions, numerical calculations, boundary conditions, numerical solution procedure, and meshing of geometric model and grid independent test.

3.2 Research Approach

A three-dimensional CFD model has been developed to simulate the flow behaviour and heat transfer characteristics in grooved channels using a commercial software package (ANSYS FLUENT-CFD V.2020R1). The Fluent code is based on the Finite Volume Method (FVM) to solve the applied governing equations [23]. Three important stages of ANSYS FLUENT-CFD analysis are implemented as follows: The first stage, which is called "*pre-process stage*", which involves generating and developing the geometrical shape as well as meshing of the studied geometry and adjusting the boundary conditions. The second step called "*solver stage*" or "*processing stage*", which includes solving the applied governing equations. Finally, the "*post-processing step*" includes the simulated results and representation of these results via graphics, plots and animations. Figure 3.1 illustrates the flow chart of the current numerical study path.

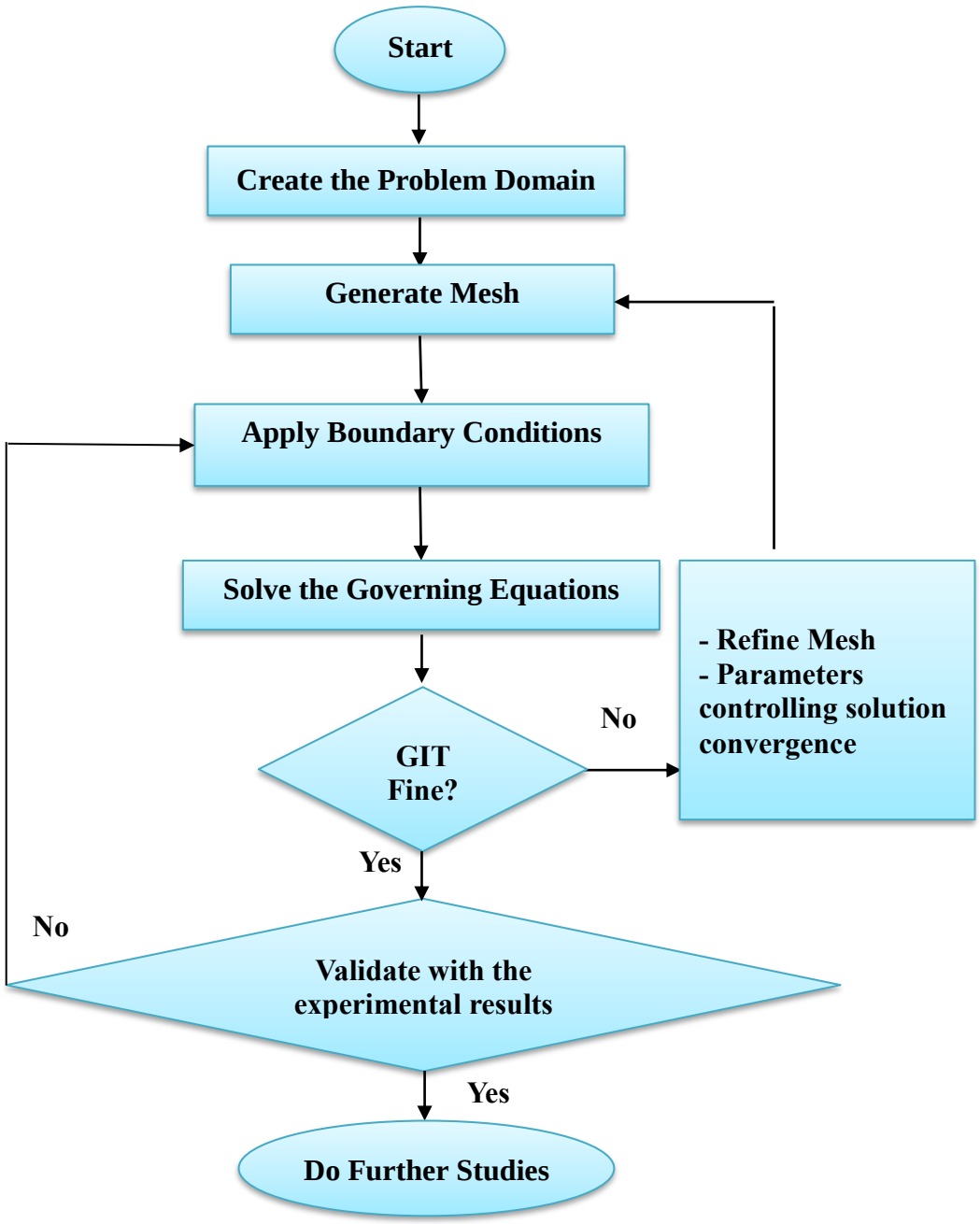

Figure 3.1: Flow chart of the current numerical study

3.3 Description of Computational Model

The first step for any numerical investigation is the construction of geometrical shape for the studied case. The entire dimensions of the conventional rectangular channels, also called here "straight or standard channel (SCH)" were chosen based on previous works published in literature with considering the ease of manufacturing. Moreover, the same manner was followed for fabricating the grooved rectangular channels. SOLIDWORK PREMIUM 2016 commercial software, which seamlessly integrates powerful design tools and drawing capabilities with built-in simulation, was utilized for constructing the computational model of the studied channels. The computational models of grooved and straight channels consist of two computational domains namely, the working fluid domain (water) and the solid wall domain (the aluminium bottom wall), as shown in Figure 3.2. The channel dimensions are modelled with height (H = 0.01 m), width (W = 0.02 m), length (L = 0.3 m) and the aluminium bottom wall thickness (t = 0.006 m) as outlined in Figure 3.2. The first step in this computational model is to simulate the straight channel (SCH), which consists of rectangular cross-section channel (0.01×0.02 m^2), as a standard case in order to compare with the selected grooved channels as shown in Figure 3.2 (a).

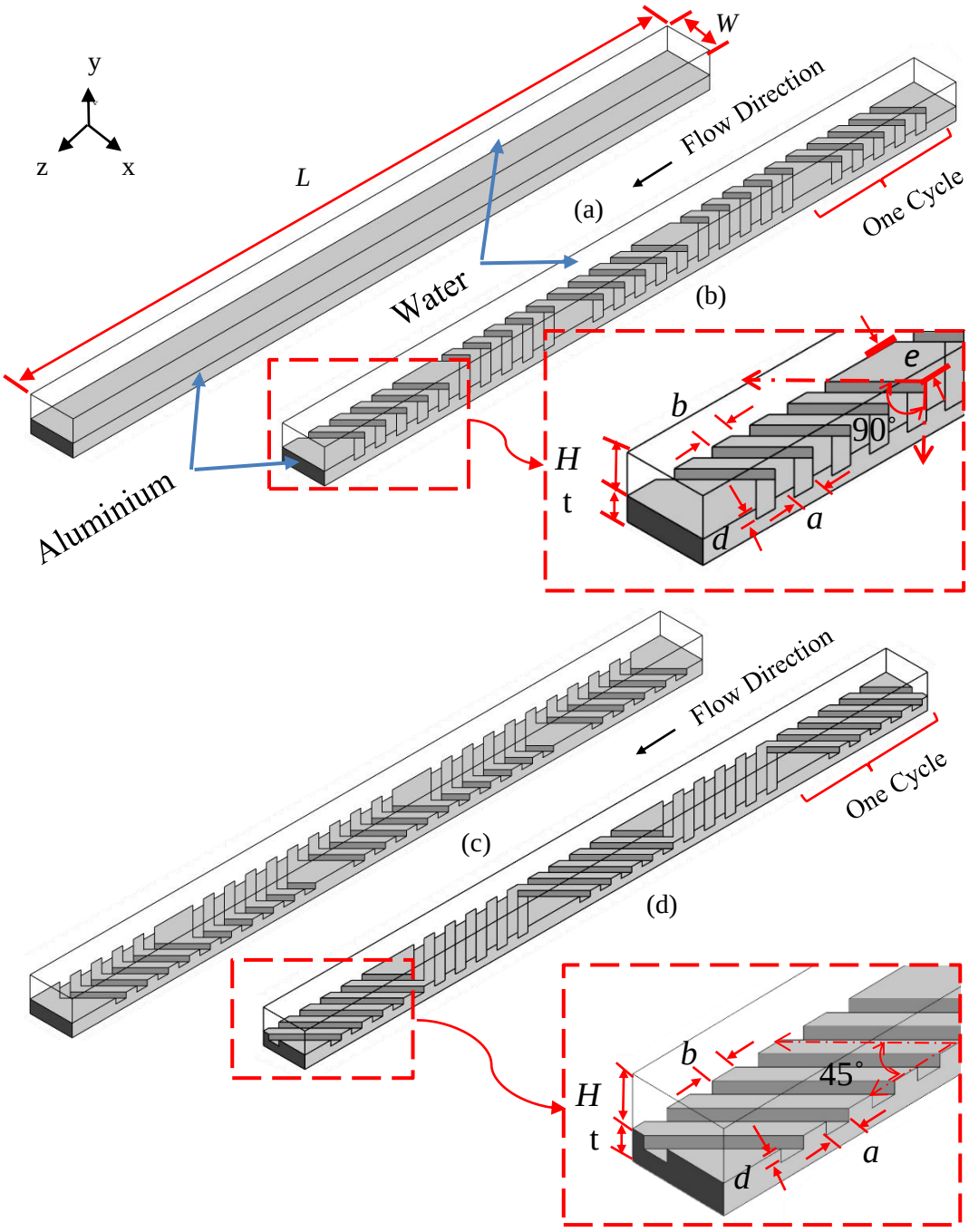

Figure 3.2: Physical geometry of the current studied channels: (a) Straight channel (SCH), (b) Forward V-shaped grooved channel (F-VGCH), (c) Backward V-shaped grooved channel (B-VGCH), (d) 45°-Inclined grooved channel (45°-IGCH)

Secondly, 45°-inclined grooved channel (45°-IGCH) is established. The number of grooves printed on the bottom heated walls is 25 grooves where these grooves are arranged in five cycles (5 grooves in each cycle) as shown in Figure 3.2 (d). The direction of these 45°-Inclined grooves is staggered per each cycle. Thirdly, V-shaped grooved channel, hereafter by VGCH, is comprised of 5 cycles in each cycle 5 staggered V-shaped asymmetric grooves (the depth of grooves (d = 0.0015, 0.0025, 0.0035 m), space among grooves (b = 0.005 m), groove width (a = 0.005 m), and the fraction of the width of the channel occupied by the wide arms of the herringbones (e = 2/3)). The bottom of the V-shaped grooved (herringbone) channel is lined up with asymmetric grooves for which the apex position switches from one side of the channel to other, midway through the channel. According to the flow direction, in the forward direction the V-shaped grooved channel is characterized by (F-VGCH) whereas for the backward flow direction (opposite direction) it is stated by (B-VGCH) see Figure 3.2 for more details.

3.4 Conservation Equations and Assumptions

The main assumptions of the heat transfer and fluid flow can be defined as follows:

1. Study a 3D model under steady-state condition.
2. The fluid is incompressible, forced laminar flow regime with single phase flow.
3. Constant thermophysical properties of the working fluid (water).
4. Ignore viscous dissipation and gravity.
5. Negligible radiation transfer.
6. No-slip condition on the walls.

The governing equations are described as follows[45]:

- Continuity Equation

$$\frac{\partial u}{\partial x}+\frac{\partial v}{\partial y}+\frac{\partial w}{\partial z}=0 \qquad (3-1)$$

- Momentum Equation in x-axis (with constant properties ρ_f has to be eliminated)

$$\rho_f\left(u\frac{\partial u}{\partial x}+v\frac{\partial u}{\partial y}+w\frac{\partial u}{\partial z}\right)=-\frac{\partial P}{\partial x}+\mu_f\left(\frac{\partial^2 u}{\partial x^2}+\frac{\partial^2 u}{\partial y^2}+\frac{\partial^2 u}{\partial z^2}\right) \qquad (3-2)$$

- Momentum Equation in y-axis

$$\rho_f\left(u\frac{\partial v}{\partial x}+v\frac{\partial v}{\partial y}+w\frac{\partial v}{\partial z}\right)=-\frac{\partial P}{\partial y}+\mu_f\left(\frac{\partial^2 v}{\partial x^2}+\frac{\partial^2 v}{\partial y^2}+\frac{\partial^2 v}{\partial z^2}\right) \qquad (3-3)$$

- Momentum Equation in z-axis

$$\rho_f\left(u\frac{\partial w}{\partial x}+v\frac{\partial w}{\partial y}+w\frac{\partial w}{\partial z}\right)=-\frac{\partial P}{\partial z}+\mu_f\left(\frac{\partial^2 w}{\partial x^2}+\frac{\partial^2 w}{\partial y^2}+\frac{\partial^2 w}{\partial z^2}\right) \qquad (3-4)$$

where P is the local pressure of fluid, and μ_f and ρ_f are the dynamic viscosity and density of water.

- Energy Equation (for the fluid) (with constant properties $\rho_f C_{P,f}$ have to be eliminated)

$$\rho_f C_{P,f}\left(u\frac{\partial T}{\partial x}+v\frac{\partial T}{\partial y}+w\frac{\partial T}{\partial z}\right)=k_f\left(\frac{\partial^2 T}{\partial x^2}+\frac{\partial^2 T}{\partial y^2}+\frac{\partial^2 T}{\partial z^2}\right) \qquad (3-5)$$

where T is the local temperature of the fluid, $k_f$and $C_{P,f}$ are thermal conductivity and the specific heat of water, respectively.

- Energy Equation (for the solid) (with constant properties k_s has to be eliminated)

$$k_s\left(\frac{\partial^2 T}{\partial x^2}+\frac{\partial^2 T}{\partial y^2}+\frac{\partial^2 T}{\partial z^2}\right)=0 \qquad (3-6)$$

where k_s is the aluminium conductivity.

3.5 Numerical Calculations

The pressure drop (Pa) along conventional rectangular channel is calculated as follow:

$$\Delta P = P_{out} - P_{in} \qquad (3-7)$$

The skin friction coefficient is evaluated as, [46]:

$$C_f = \Delta P \frac{D_h}{2\rho_f U^2 L} \qquad (3-8)$$

Reynolds number can be calculated as the following formula [46]:

$$Re = \frac{\rho.U.D_h}{\mu} \qquad (3-9)$$

Where D_h (m) has represented the hydraulic diameter of grooved rectangular channel, can be found as follows [46]:

$$D_h = 4\frac{A_c}{p} = \frac{2W.H}{(H+W)} \qquad (3-10)$$

Where A_c (m^2) and p (m) are represented the cross sections area and perimeter of conventional rectangular channel.

The average heat transfer coefficient $\bar{h}$ ($W/m^2.^{\circ}C$) and the average Nusselt number $\overline{Nu}$ can be calculated based on the total internal surface area A_s (m) of the grooved rectangular channel respectively [47]:

$$\bar{h} = \frac{Q}{A_s\left[T_s - \left(\frac{T_{b,out}+T_{b,in}}{2}\right)\right]} \qquad (3-11)$$

Where $T_{b,out}$ and $T_{b,in}$ are outlet and inlet temperature of the fluid, A_s the total internal surface area of the Conventional rectangular channel.

$$\overline{Nu} = \bar{h}\frac{D_h}{k_f} \qquad (3-12)$$

To estimate the improvement techniques used in the present study. The Performance Evaluation Criterion can be expressed as[48]:

$$PEC = \left(\frac{\overline{Nu}_G}{\overline{Nu}_S}\right) \Big/ \left(\frac{C_{f,G}}{C_{f,S}}\right)^{1/3} \qquad (3-13)$$

3.6 Boundary Conditions

The boundary conditions (BCs) are necessary in order to solve the governing equations. In general, the flow criteria are defined inside the flow field, which is essential to achieve a converged solution. For meaningful solutions, the BCs must be carefully defined. The applied BCs in this investigation are listed in Table 3.1 (see figure 3.3 for more details). Constant axial wall heat flux through the aluminium bottom wall of straight channel and grooved channels is employed with the applied value of constant heat flux of 15000 W/m^2. Two physical domains are selected for both straight channel and grooved channels namely, fluid domain and solid domain. Conjugate heat transfer is utilized for the characterization of heat flow, which involves the variation in temperature within solid and fluid that could happen due to thermal interaction between them, for both straight channel and grooved channels. Fully-developed hydrodynamic flow (fully-developed velocity profile) is imposed at the channel inlet (inflow BCs). The rectangular cross-section channel was simulated with the length equalling to the estimated entrance length to achieve the hydrodynamically fully-developed according to the highest studied value of Reynolds number. a required length calculates according to the following equation [47]:

$$L_{Laminar} \approx 0.05 \times Re\ D_h \qquad (3-14)$$

Then, the fully-developed velocity components were exported to the studied grooved channel for representing the inflow velocity

corresponding to the desired Reynolds number (see Figure 3.4). The studied range of Reynolds number is 100 -1000 at a constant inlet temperature (T_{in}) 27 °C (300 K). The constant thermophysical properties of the working fluid (water) and solid part (aluminium) are set in the ANSYS FLUENT software as shown in Table 3.2. In addition, a Neumann boundary condition was applied at the outflow of the channel ($P_{out} = P_{gauge}$) to avoid the diverged solution and block the reversed backflow.

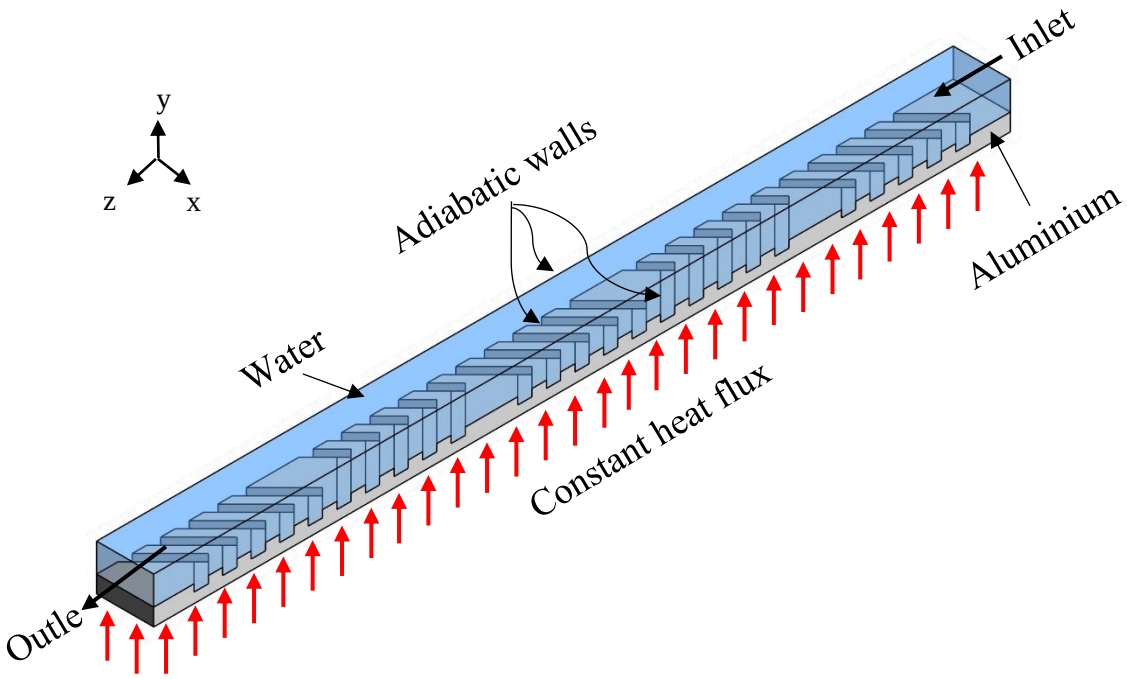

Figure 3.3: Physical geometry with applied boundary conditions

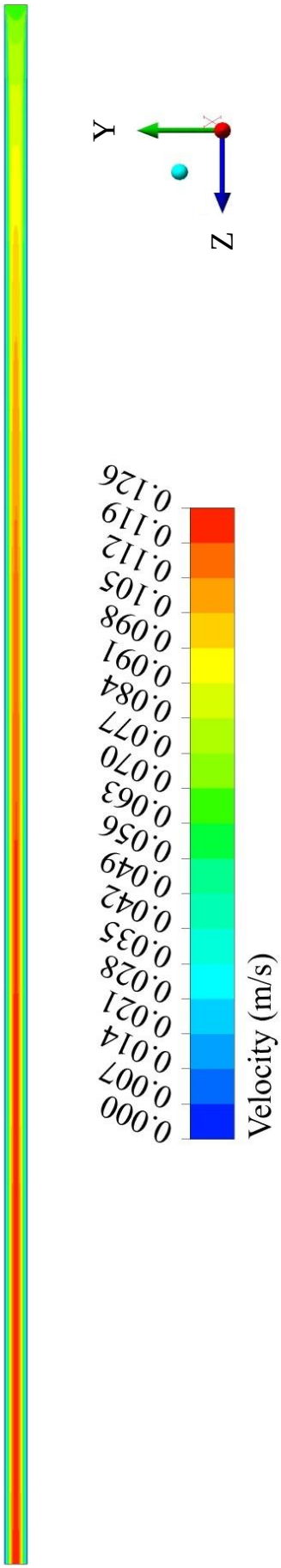

Figure 3.4: velocity profile for developing simulation at Re=1000 and length 0.7m

Table 3.1: The applied boundary conditions of the studied numerical model

Boundaries	Flow B.Cs	Heat transfer B.Cs
Inlet	*Fully developed velocity profile, Re = 100 -1000*	T_{in}= 27 °C
Outlet	$P_{gauge} = 0$	$\frac{\partial T}{\partial z} = 0$
Top and side walls of channel	$u = v = w = 0$	$k_f \frac{\partial T_f}{\partial n} = 0$ *or* $k_s \frac{\partial T_S}{\partial n} = 0$
Bottom surface of channel	$u = v = w = 0$	$-k_s \frac{\partial T_S}{\partial n} = q$=15000 W/m^2
Grooved wall	$u = v = w = 0$	$-k_f \frac{\partial T_f}{\partial n} = -k_s \frac{\partial T_S}{\partial n}$

Table 3.2: The thermophysical properties for water and Aluminium

Materials	ρ (kg/ m^3)	C_p (J/kg . ˚C)	k (W/m . ˚C)	μ (kg/ m .s)
Water	*995.8*	*4182*	*0.607*	*0.00086*
Aluminium	*2719*	*871*	*202.4*	---

3.7 Solution Methodology

In order to solve the continuity and energy equations, Finite Volume Method (FVM) was utilized with the corresponding boundary conditions. The second-order upwind differencing scheme is adopted for the convective terms, while Coupled algorithm was used to link the pressure and velocity fields. The coupled algorithm solves the momentum and pressure-based continuity equations together. The full implicit coupling was achieved through an implicit discretization of pressure gradient terms in the momentum equations, and an implicit discretization of the face mass flux, including the Rhie-Chow pressure dissipation terms. The gradient calculation uses green-gauss cell based. The term of diffusion in the

energy and momentum equations was approximated by second-order central difference. The default under relaxation factors provided in Fluent was used for momentum, pressure, energy calculations. The convergence criterion for the continuity was set to 10^{-7} at first, then reduced to 10^{-5} and it was found that there was no change in the results. While the residual criteria for the momentum and energy equations was set to 10^{-7}

3.8 Numerical Solution Procedure

In the commercial code Fluent V.2020R1 of the numerical solution for each simulation, it was noticed that the processing time is about 1-5 h (Intel Core i7-7500U, 4 processors) and the following steps are taken into account [23]:

1. After exporting the geometric mesh to the Fluent under ANSYS-FLUENT Workbench, the desired mesh appears then automatic starting mesh reading, mesh checking and giving the quality report. Select Pressure-Based approach as a Solver Type, where in this approach, the pressure field is extracted by solving a pressure correction equation, which is obtained by manipulating both continuity and momentum equations. Select laminar flow model and activate the energy equation.
2. Define materials and cell zones conditions: Water (liquid) for fluid domain and Aluminum for solid domain.
3. Apply the boundary conditions (section 3.6)
4. Select the following options for the solution method:
    - Pressure–velocity coupling = Coupled

(Solution algorithms for pressure-velocity coupling in steady-state flow are the standard prepossessing methods utilized for solving steady problems in CFD.)

- Pressure = Second order
- Momentum = Second order upwind
- Energy = Second order upwind

(The second-order central scheme is implemented for the discretization of the diffusion terms.)

5. Set Residual values (maximum error) as following:
   - Residual of continuity = 1×10^{-5}
   - Residual for velocities = 1×10^{-7}
   - Residual for energy = 1×10^{-7}
6. Initialize the flow field, inter a suitable number of iteration (more than 10000) and run the case.
7. Save data and the appropriate results in order to be displayed and explained in chapter five.

3.9 Meshing of Geometric Model and Grid Independent Test (GIT)

The quality of mesh has significant effects on the accuracy of the numerical results and the time required to reach the final solution of the numerical simulation. Therefore, when establishing the mesh, consideration must be given to the mesh quality and number. In general, a denser mesh takes more time and more memory in the computer, so the results are tested for stability and accuracy with the least number of meshes.

Figure 3.5 shows the pure hexahedral mesh for both solid domain and fluid domain of the selected 45˚-IGCH, and F-VGCH. The orthogonal and skewness quality of mesh are also tested and it is found that the orthogonal and skewness quality of 45˚-IGCH are equal to 0.8 and 0.3, respectively. Furthermore, the orthogonal and skewness quality of F-VGCH is equal to 0.99 and 0.06, respectively.

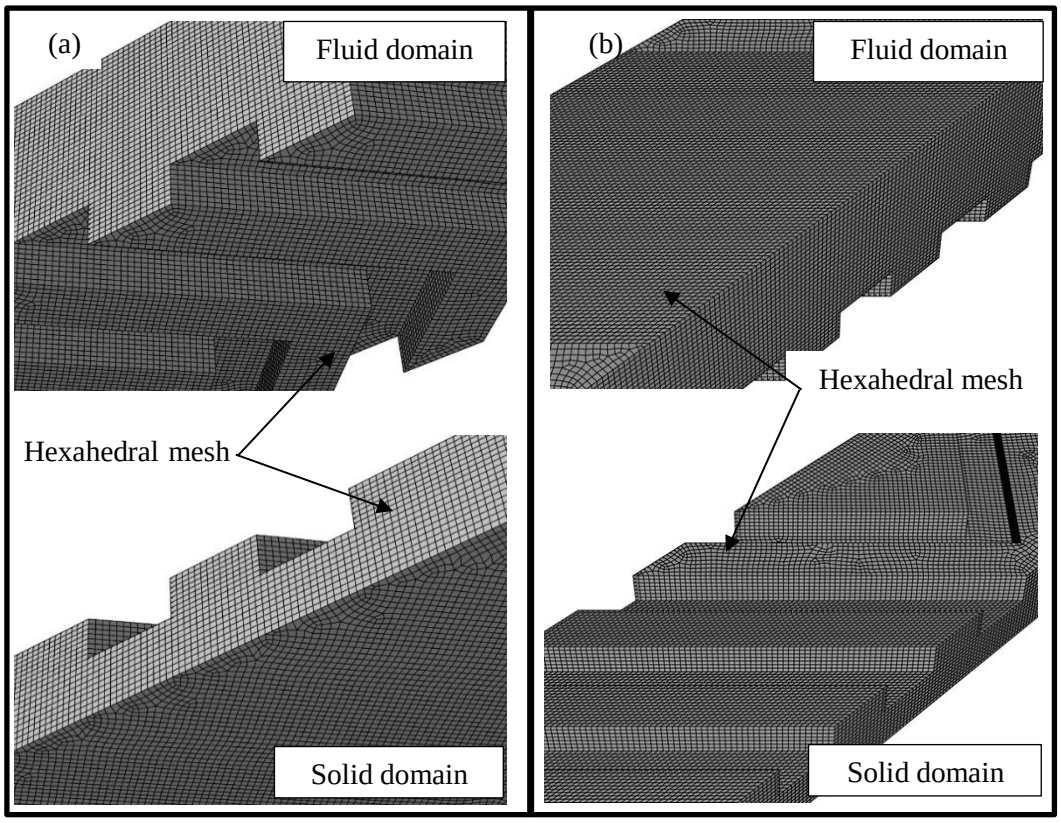

Figure 3.5: Computational mesh for the grooved channels
(a) VGCH, (b) 45°-IGCH

(45°-IGCH) and (F/B-VGCH) were designed using SOLIDWORK as mentioned previously, then the CAD model is imported to the ANSYS Design Modular[23]. The geometry was defined to fluid domain and solid domain, and then divided it into 102 bodies to get a suitable mesh for (F-VGCH), (B-VGCH) and 106 bodies for (45˚-IGCH). The faces of the solid and fluid domains are named as inlet, outlet, insulated walls and heated wall, after that export the geometric file to ANSYS meshing.

In ANSYS meshing[23], Grid Independent Test (GIT) procedure is performed to estimate the number of required nodes in the current study. This technique is used to test the effect of increasing the node number on the stability of computational data such as Nusselt number, surface temperature and friction factor. From details list of ANSYS meshing, CFD was choice for physics performance and Fluent for solver performance.

MultiZone mesh method was selected for meshing the model geometry with element size varied from 0.3 to 0.5 mm. The MultiZone mesh method provides an automatic decomposition of the geometry into mapped (structured) regions and free (unstructured) regions. It automatically generates a pure hexahedral mesh where possible. MultiZone has different capabilities that make it more suitable for a class of problems for which the sweep method would not work without extensive decomposition. The GIT was performed for (45°-IGCH), (F-VGCH), and (B-VGCH) before the simulation is carried out for the highest Reynolds number (Re = 1000) while the node number is varied from 0.82×10^6 to 3.55×10^6 as shown in Table 3.3. The relative error is calculated based on the following equation:

$$e\% = \left|\frac{J_{new}-J_{old}}{J_{old}}\right| \times 100 \qquad (3-14)$$

where, J represents any selected parameter such as average Nusselt number, skin friction coefficient, or surface temperature. Since, the increase of cells number after 2.33×10^6 of (F -VGCH), 2.42×10^6 of (B-VGCH), and 2.54×10^6 for (45˚-IGCH) leads to less than 1.6 % of $\overline{Nu}$, T_s, and C_f. Thus, the nodes number 2.33×10^6, 2.42×10^6, and 2.54×10^6 are considered as mesh independence for (F-VGCH), (B-VGCH), and (45˚-IGCH), respectively (see Figure 3.6 for more details).

Table 3.3: Grid independent test for 45°-IGCH, F-VGCH, B-VGCH with different number of nodes

No. of node $\times 10^6$	$\overline{Nu}$	e %	$C_f Re$	e %	T_s (°C)	e %
45°-IGCH						
1.45	6.102	5.01	15.076	8.2	47.325	1.95
2.08	6.408	3.31	16.321	4.29	46.402	1.27
2.54	6.62	0.65	17.012	0.63	45.811	0.28
2.97	6.577	0.2	16.905	0.04	45.938	0.03
3.55	6.564	0	16.911	0	45.951	0
F-VGCH						
0.82	8.064	4.40	17.172	4.71	42.219	1.39
1.62	8.419	5.89	17.98	4.99	41.631	1.78
2.33	8.915	0.69	18.878	1.55	40.892	0.22
2.81	8.854	0.58	18.585	0.13	40.982	0.21
3.22	8.802	0	18.61	0	41.068	0
B-VGCH						
0.85	6.626	4.13	15.305	0.66	44.884	1.53
1.68	6.899	2.7	15.407	5.26	44.198	0.98
2.42	7.085	0.08	16.217	1.26	43.767	0.01
2.88	7.08	1.32	16.421	0.2	43.773	0.73
3.35	6.986	0	16.387	0	44.091	0

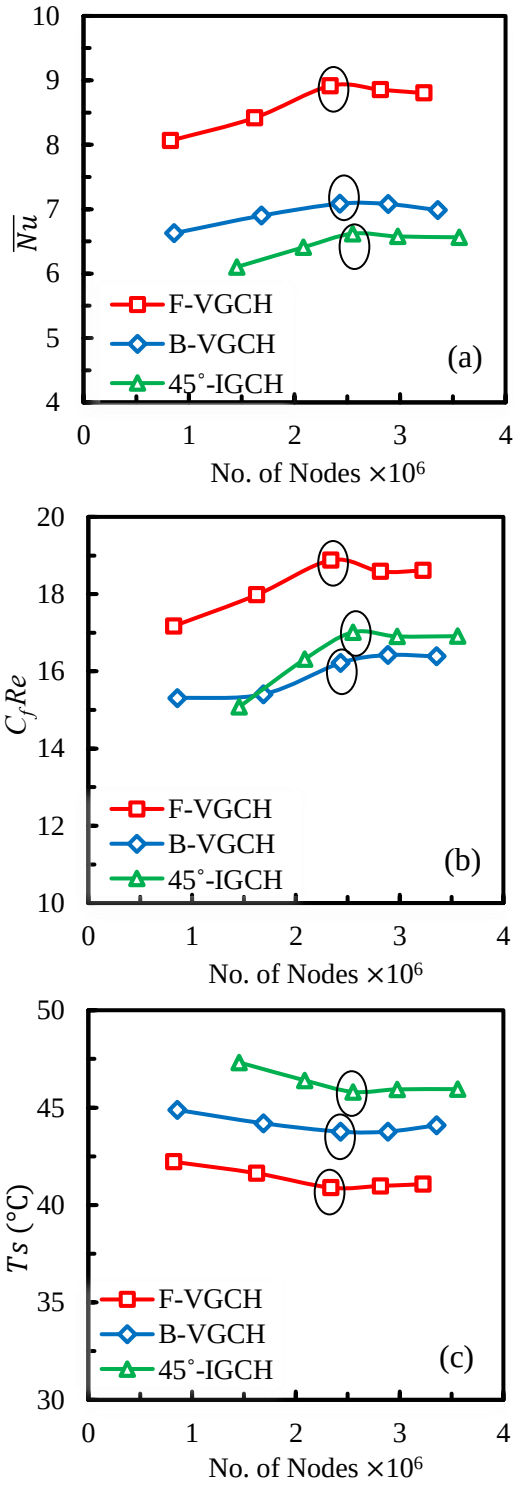

Figure 3.6: Grid independent test of grooved channels: (a) average Nusselt number, (b) skin friction coefficient-Reynolds number, (c) surface temperature

CHAPTER FOUR
EXPERIMENTAL SETUP

CHAPTER FOUR
EXPERIMENTAL SETUP

4.1 Introduction

This chapter display the experimental arrangements, measurement instruments and the test procedures to quantify the pressure drop and heat transfer in grooved channels. The arrangement of test rig was constructed in a modular method, capable of accommodating different setups depending on the particular requirements of the intended experimental research. This chapter is divided into three sections to describe the experimental test rig, experiment procedure and data reduction.

4.2 Experimental Test Rig

This section explains the entire details of the experimental test rig (manufacture, connection, and installation) comprising integrated closed-loop. The closed-loop includes a water tank, water pump, control valves, flowmeter, test section, thermocouples, temperature data recorder, pressure manometer, radiator, power regulator, and electric heater as depicted in Figure 4.1. Distilled water was supplied from a water tank into the test section using a centrifugal booster pump. Glob valve was installed to regulate the water flow rate after the pump. Flexible plastic tubes (Tygon tube, outer diameter 5 mm) were used to connect the test section with the water tank and also for discharging fluid out to the radiator. Flowrates of experimental tests were selected to preserve the flowrate of working fluid within the laminar flow regime.

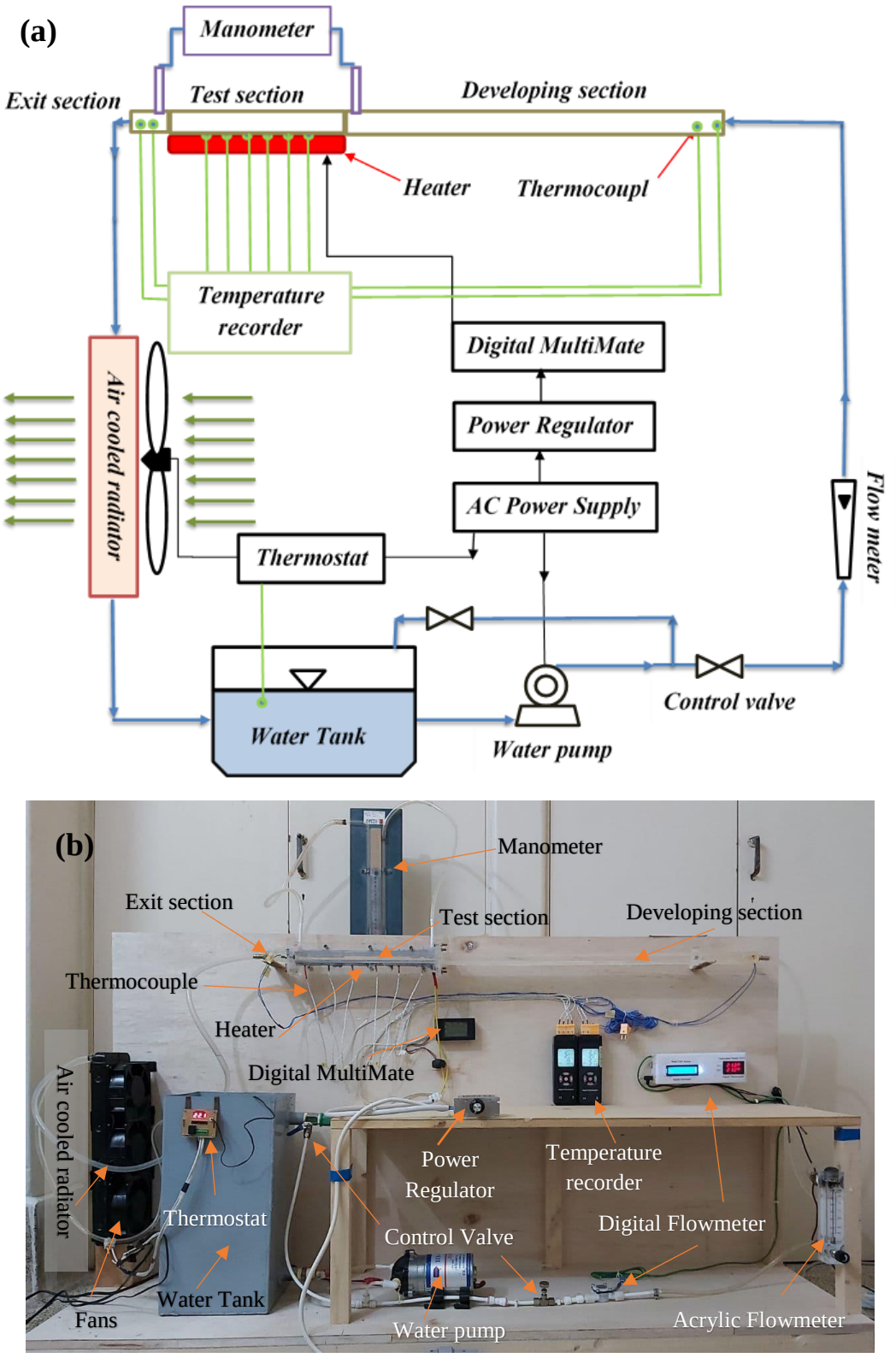

Figure 4.1: (a) Schematic diagram of the experimental test rig. (b) Photographic picture for the experimental test rig

The water flowrate was extremely balanced by the flowmeter and control valves in order to achieve steady-state and smooth flow even with changing the flow rate. This is done via a control valve located before the digital flowmeter, obtaining 0.155 LPM to 0.777 LPM flow rates, which corresponds to 200–1000 Reynolds numbers, respectively. The controlled fluid flow is then entered into the developing section.

4.2.1 Developing Section

The smooth and adiabatic developing section were constructed to guarantee a fully-developed velocity profile for water before entering the test section. This section was made from an acrylic sheet (with 0.006 m thickness). The developing section has a length of 0.7 m and has a cross-sectional area of 0.01 m height and 0.02 m width, which remained identical with the inlet cross section. The length of developing section was chosen to be proportional to the highest value of Reynolds number and to ensure that the whole tested flowrates have a fully-developed velocity profile (according to equation 3.14). The test section was connected with the developing section by flanges, which were manufactured by acrylic sheet. The test section was directly mounted to the developing section by using match flanges with bolts and nuts. Silicone gasket sealant was used between the mounted flanges to prevent leakage in these joints and it was ensured that no leakage in the supply water may occur. As a result, it is so easy to change the test section and install four different shapes of channels with different geometries. In addition, two thermocouples were installed at the beginning of the developing section for measuring the average inlet temperature of the working fluid.

4.2.2 Test Section

The test section consists of three walls (two side walls and top wall), which are made from acrylic. The acrylic was carefully insulated (*k = 0.2 W/m.s*) to ensure providing adiabatic boundary conditions on these walls (see Figure 4.2). While the bottom wall of the channel was fabricated from aluminum, which is a sheet plate with 0.006 m thickness. The grooves are machined into a (0.3 m × 0.02 m) piece of aluminum (~202.4 W/m.k) using Computer Numerical Control (CNC) machining (see Figure 4.3) with five grooves on each cycle (5 cycles). In addition, two acrylic flanges with 6 mm thickness were used to join both ends of the test section, as shown in Figure 4.2. The cross-section dimensions of each groove are 2.5 mm and 5 mm for depth and width, respectively, and the space between the grooves is 5 mm. The three acrylic walls and the bottom grooved aluminum wall are assembled together to form a rectangular grooved channel. Two different patterns of grooves are machined on the bottom wall of the channel namely, V-grooved channel (in two flow ways: forward (F-VGCH) and backward (B-VGCH)) and 45-inclined grooved channel (45˚-IGCH) as well as the straight standard channel (SCH) (see Figure 4.4). Six holes with a diameter of 2 mm and a depth of 3 mm are made into the down surface of the bottom wall of the channel in order to embed K-type thermocouples for measuring the average wall temperature. The bottom wall can be heated by using attached electric heater, whereas the other walls are supposed to be adiabatic. Two pressure taps with a diameter of 5 mm are installed in the entering and exiting zones of the top wall of the channel to measure the pressure difference between the inlet and outlet.

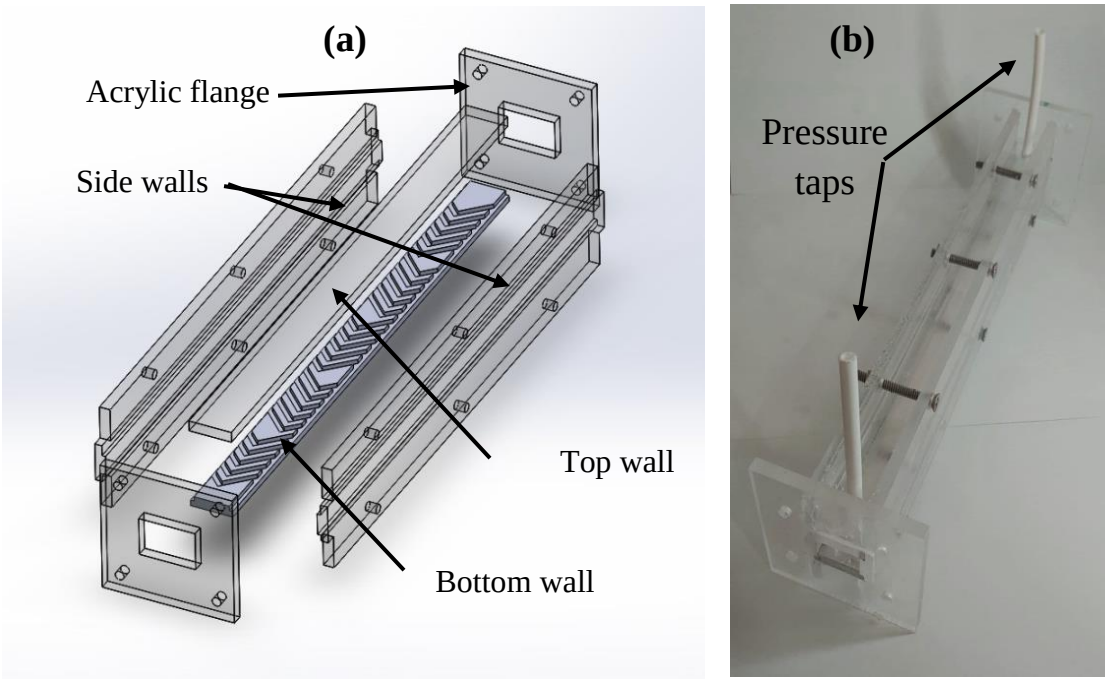

Figure 4.2: (a) A schematic diagram of the main components of the test section, (b) assembled components of the experimental test section

Figure 4.3: Photographs illustrate the forming process of the grooved channel on the bottom wall of the channel by using CNC machining.

4.2.3 Exit Section

This section joins with the test section via the flanges, as depicted in Figure 4.1, and it has the same cross-section dimensions of the test section with a length of 50 mm. In addition, this section contains two K-type thermocouples to measure the outflow temperature. The end of the exit section is perfectly connected with the Air-cooled radiator by plastic pipe.

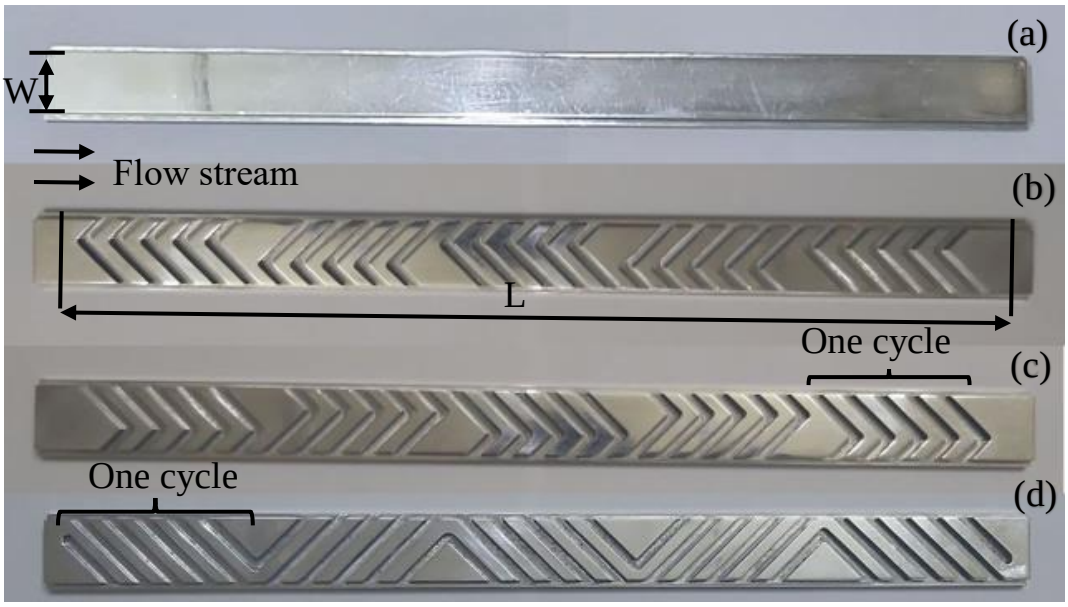

Figure 4.4: Photographs showing the fabricated pieces of grooved channels with different patterns: (a) SCH, (b) F-VGCH, (c) B-VGCH, and (d) 45-IGCH

4.2.4 Power Regulator and Electric Heaters

An electric heater with a length of 0.3 m, a width of 0.02 m and a thickness of 0.004 m is equipped for heating the bottom wall of the grooved channel, as illustrated in Figure 4.5. In order to place the thermocouples within the bottom wall of the channel as mentioned previously, six holes with a diameter of 3 mm were drilled into the electric heater. The maximum power of the heater is 340 W. The input power of the heater can be manually adjusted by a voltage regulator (AC voltage regulation 0-220V).

Rock wool isolator was used as an insulating material of the grooved channels, which is made from fiberglass and arranged by using a binder into a texture, as shown in Figure 4.6. . The test section is covered with this material in order to reduce the heat losses from the walls and the supplied power for the electric heater.

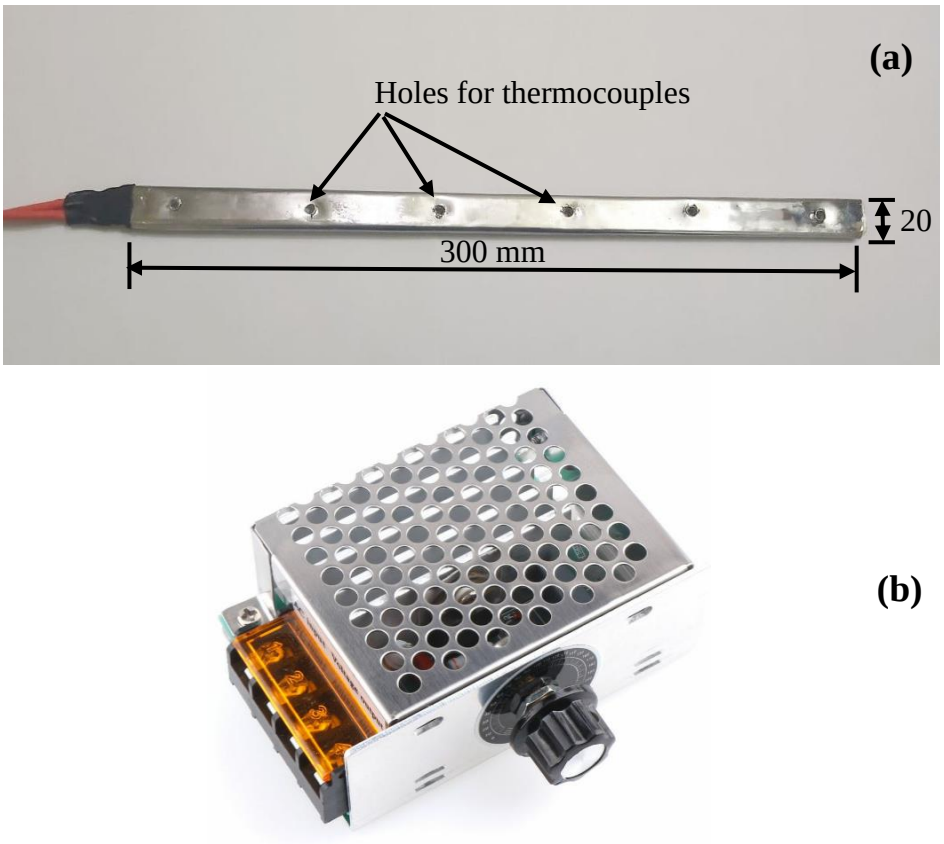

Figure 4.5: Photograph showing (a) electric heater (b) voltage regulator

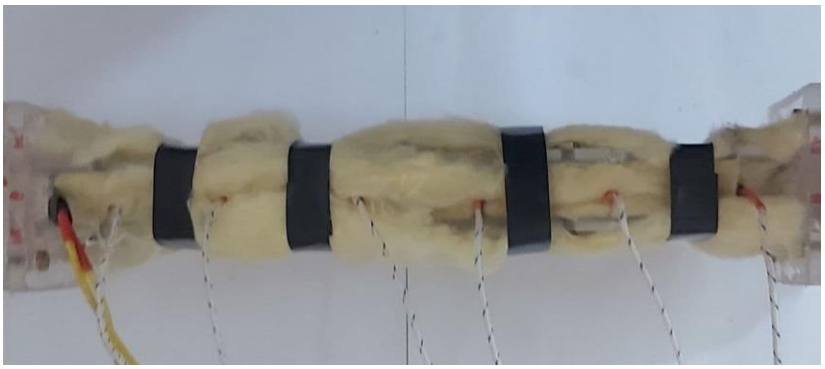

Figure 4.6: Rock wool for insulating the test section and electric heater

4.2.5 Air-Cooled Radiator and Thermostat

The hot water exiting from the outflow of the test section is circulated and cooled by an air-cooled radiator in order to keep the inflow water at a constant temperature. In order to control the temperature of the water inside the tank, a thermostat (XH-W1209 thermostat temperature control with DC 12V mini temp control switch board) is directly connected to the sensor of the fans used in the air-cooled radiator. The water temperature is set at 27 $^{\circ}C$ and the temperature is quantified and controlled by a thermostat sensor, which is placed in the water tank. It is worthwhile mentioned that the air-cooled radiator made of aluminum with dimensions of 390×118×30 mm, occupied with three AC axial fans (Size:120×120×38 mm, Power: 22W) , as depicted in Figure 4.7.

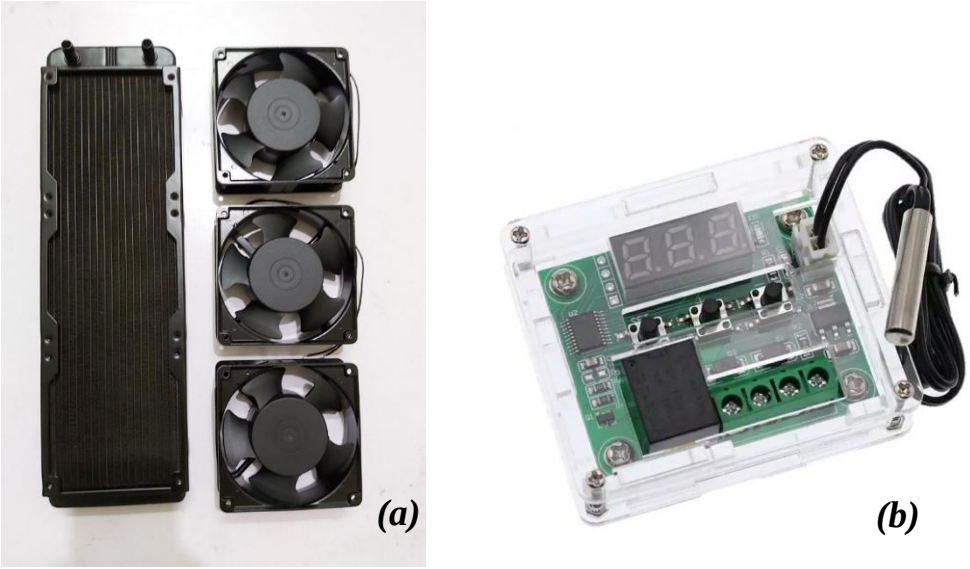

Figure 4.7: (a) The air-cooled radiator (b) Thermostat

4.1.6 Water Tank and Water Pump

A tank with dimensions of 0.2 m×0.2 m×0.4 m and a capacity of 16 litres is utilized to store and supply the water. The water tank is made of galvanized iron, as shown in Figure 4.8 (a). A centrifugal pump (HI-QU-50G) is used to deliver the water from the tank to the other parts of the

experimental test rig, as shown in Figure 4.8 (b). The pump specifications are listed in Table 4.1. The working fluid (water) removes heat from the bottom wall of the channel. Then, the warm water passes through the channel to be cooled by the air-cooled radiator and then disposed to the tank again to complete its cycle.

Table 4.1: Pump specifications

Model	**Quantity**	**Unit**
Flow Rate	≥ 0.8	LPM
Working Pressure	4.8	bar
Rated Voltage	24 DC	Volt
Self-Suction Height	2	m

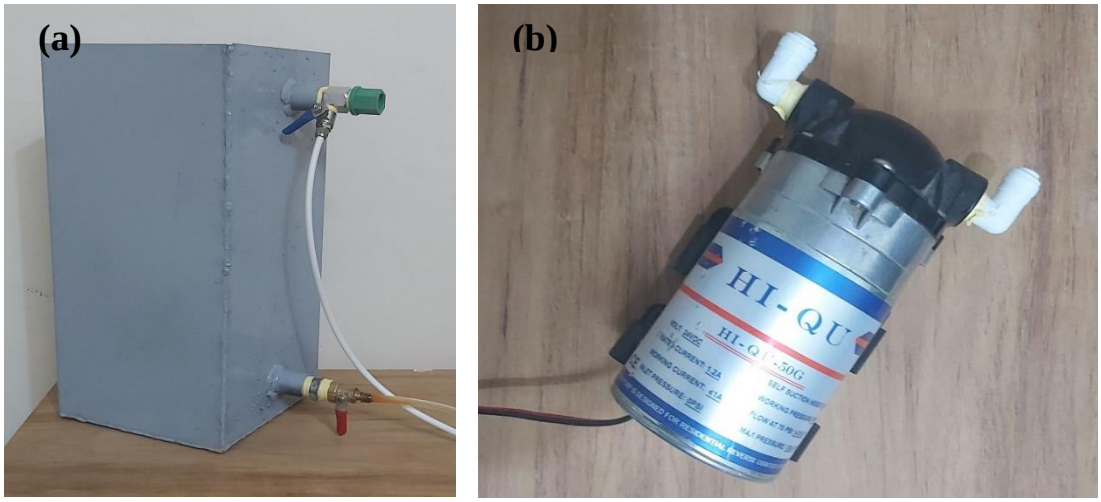

Figure 4.8: (a) Water tank and (b) Water pump

4.3 Measurement Instrumentations

Various measurement instruments were employed for measuring the studied parameters from the experimental test. The experimental test rig is equipped with ten thermocouples, water flowmeter, manometer, and AC power monitor for power measurement of the electrical heater, as showed in Figure 4.1. Basically, all these instruments are systematically calibrated before using. The calibration details of these instruments are explained in Appendix (A), and the calculations of uncertainty analysis for

experimental measurements are shown in Appendix (B). The measurement instrumentations are explained as follows:

4.3.1 Thermocouples and Digital Thermometer

Ten K-type thermocouples are utilized to monitor the temperatures of the fluid flow in different positions along the experimental test rig in the range of (-50°C to 1350°C, as supplier quote). These thermocouples are connected with two digital thermometer (model number: PD_6), as shown in Figure 4.9. The digital thermometer is able to visualize the temperatures in three different scale units °C, °F, and K, with an accuracy of (± 0.15% reading + 1°C/1.8°F). The thermocouples that are used in the current study were calibrated with a mercury bulb thermometer with accuracy (±0.1°C) in the range of temperature from 0°C to 100°C. The maximum error in the reading was found to be in about of ±1.98%. These thermocouples was installed in the following positions:

Two thermocouples were fixed at the inlet of the developing section (see Figure 4.1). Thermocouples inserted in the fluid flowing at the beginning of the test section, in order to measure the temperature of the incoming water. The thermocouples were located at a certain distance from the test section in order to ensure that the flow inside the channel was not obstructed and thus the velocity profile of water was maintained under a fully developed before entering the test section.

Six thermocouples were embedded in the back surface of the bottom wall of the grooved channel to measure the temperature distribution along the test section (see Figure 4.10). These thermocouples were inserted in the holes, which are drilled with a diameter of 2 mm from the rear side of the bottom grooved channel wall. The thermocouples are fixed using thermal glue (type of epoxy). The holes were centered on the channel wall and located with 1 mm apart from the inner grooved wall of the channel. These

holes were located at 25, 75, 125, 175, 225, and 275 mm from the inlet of the test section.

Additionally, two thermocouples are placed at the outlet of the exit section in order to measure the outflow water temperature.

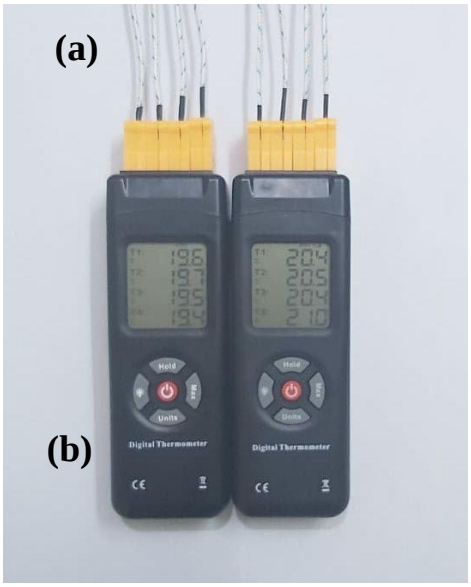

Figure 4.9: K-Type thermocouples connected to the digital thermometers

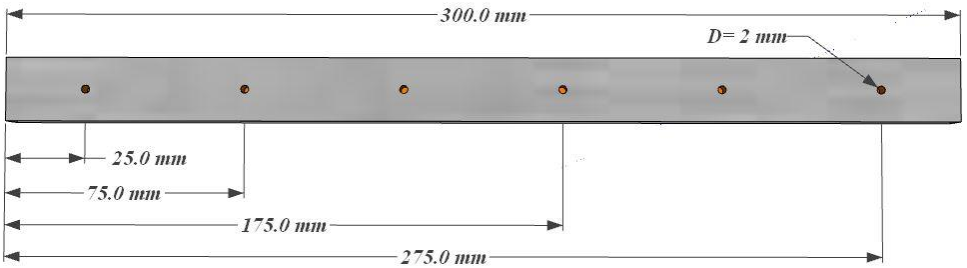

Figure 4.10: Positions of thermocouples in the back surface of the bottom wall of the grooved channel

4.3.2 Pressure difference manometer

In order to evaluate the skin friction coefficient through the tested channels, the pressure drop across the test section is measured. Two taps with a diameter of 5 mm are installed on the top wall between the inlet and outlet of the test section (see Figure 4.2 for more details). The

longitudinal distance between these taps is 280 mm. These taps are connected with U-tube manometer. The maximum error of reading was found about of ±9.2%.

4.3.3 Flowmeter

The flowrate of working fluid is quantified by using a digital flowmeter within a range of 0.15 - 6 LPM. This digital meter has a flow sensor, turbine wheel, which rotates as the water flows from the inlet opening gate to the outlet section, as shown in Figure 4.11 (a). The turbine wheel has a magnet field, which gives pulses to the Hall Effect Sensor. The flow sensor connects to the microcontroller board (Arduino Uno R3) and LCD display (LCD 16X2 Blue Backlight 5V with l2C) in order to display the readings with a high-quality Hall Effect Sensor, as shown in Figure 4.11 (b). The connection diagram and the details of the programming code are depicted in Appendix (C). In addition, the digital flowmeter is calibrated with a standard precision-machined acrylic flowmeter for water of accuracy (±0.25) in the range of flow rate from 0.2 L/min to 2.0 L/min. An accuracy of ±5% was found in the flow rate calibration experiments.

(b)

(a)

Figure 4.11: (a) digital flowmeter sensor, (b) microcontroller board (Arduino Uno R3) with LCD

4.3.4 AC Power Monitor

An AC power monitor is utilized to measure the electrical heater power by estimating the inlet current, voltages and power. The data is directly displayed on the LCD screen, as illustrated in Figure 4.12. The specifications of the power monitor (as mentioned by supplier) are powered within test range 0 - 4.5 kW, working voltage (test range 80 - 260 VAC), working current (test range: 0 - 20 A), operating frequency (45 - 65 Hz. All measured parameters have accuracy around (1.0 grade).

Figure 4.12: AC power monitor module with monitor screen

4.4 Experiment Procedure

This section provides a detailed description for the experimental procedure that has adopted in the experiments. The experimental measurements are performed over a range of Reynolds numbers of 200-1000 and the constant heat flux (15000 W/m^2) is applied on the bottom wall of the grooved channels. After calibration, the following experimental protocol is systematically applied for performing the experiments:

1. The tank was filled with water and all pipe connections were tested to ensure that there was no leakage. The pump was switched on for circulating the working fluid throughout the experimental rig.
2. After the flow rate was monitored with a flowmeter, the control valve was appropriately set in order to reduce the flow rate to the

desired amount. The electric heater was switched on to adjust the constant heat flux, which was applied on the down surface of the bottom wall of the grooved channel by adjusting the input voltage given by the DC power supply using power regulator.

3. The inflow and outflow bulk temperature of the working fluid were monitored by the placed thermocouples after reaching a steady-state condition, then the constant readings were recorded with time. Also, the wall temperatures were recorded after reaching the regularity of heated surface temperature readings.
4. The pressure-drop readings across the inlet and exit regions of the test section were simultaneously evaluated by manometers.
5. Steps 2-4 were repeated for each test case to cover all ranges of the flow rates (Reynolds number range of 200-1000).
6. The steps (1-5) were repeated with the using of different configurations of the channels.
7. To minimize the variance in the measuring instruments, each reading was repeated several times at the same operating conditions until the readings or calculations produce similar or equivalent results.

4.5 Data Reduction

The average Nusselt number, the skin friction coefficient can be determined thus the performance evaluation criterion of the experimental test can be determined by relying on the experimental data such as inlet and outlet temperature, average wall temperature, pressure drop, voltage, and current. The total power input to the electric heater is calculated as follows[47]:

$$Q_{in} = I \times V \qquad (4-1)$$

Where, I is the current (Amp) and V is the voltage (Volt). The heat absorbed by flowing water is estimated by [47]:

$$Q_{out} = \dot{m}\, C_{P,f} \left(T_{b,out} - T_{b,in}\right) \qquad (4-2)$$

Where, $\dot{m}$ (kg/s) is the mass flow rate:

$$\dot{m} = \rho U A_c \qquad (4-3)$$

Where, $C_{P,f}$ is the specific heat of the fluid, $T_{b,out}$ and $T_{b,in}$ are the average bulk temperatures at the inlet and outlet of the test section, respectively.

The average heat transfer coefficient $\bar{h}$ can be expressed as follows[47]:

$$\bar{h} = \frac{Q_{out}}{A_s\left(T_{s,av} - T_{b,av}\right)} \qquad (4-4)$$

Where, A_s is the surface area of the grooved wall, $T_{s,av}$ and $T_{b,av}$ are the average surface temperature and average bulk fluid temperature, respectively, which are calculated as follows:

$$T_{s,av} = \frac{\sum_{i=1}^{n=6} T_{s,i}}{6} \qquad (4-5)$$

$$T_{b,av} = \frac{T_{b,in} + T_{b,out}}{2} \qquad (4-6)$$

The average Nusselt number is estimated according to equation (3-12).

The skin friction coefficient C_f is determined by the pressure drop ($\Delta P = P_{out} - P_{in}$) along the flow direction of grooved channel as shown in equation (3-8):

To estimate the improvement techniques proposed in the present study, performance evaluation criterion (*PEC*) has been used (see equation (3-13)).

The grooved channels with different groove patterns have been applied in industrial applications in order to enhance heat transfer efficiency due to their capability to encourage inertial instability (forming secondary flow).

4.6 Uncertainty Analysis

The measured data from the experimental test is usually influenced by various types of errors, including random, precision, and systematic errors. Precision and systematic errors are two types of errors that cannot be reduced by repeating measurements or combining large numbers of readings, while calibration of measurement instruments is a popular approach to reduce the systematic error [49]. Accordingly, without a determination of measurement uncertainty, which determines the appropriate range of values for the final results within a given degree of confidence, experimental results are considered incomplete. Therefore, in order to assess the measurement uncertainty, it is important to identify the measurement's uncertainty sources and its magnitude arising from each source. Then, the measurement uncertainty must be calculated due to an inherent error in the measured values from each source parameter.

In the present work, the uncertainties in the Reynolds number, Nusselt number, and the skin friction coefficient are estimated. There are many methods can be used to analyze the experimental errors. The analysis is carried out based upon the basis of the suggestion made by Kline and McClintock [50], as one of these methods.

Let the result (R) be a function of n independent variables: $X_1, X_2, X_3, \ldots\ldots X_n$

$$R = R(X_1, X_2, X_3, \ldots\ldots X_n) \qquad (4-7)$$

Hence, the uncertainty interval (U_R) in the results can be estimated as:

$$U_R = \pm\sqrt{\left(\frac{\partial R}{\partial X_1}U_{X_1}\right)^2 + \left(\frac{\partial R}{\partial X_2}U_{X_2}\right)^2 + \left(\frac{\partial R}{\partial X_3}U_{X_3}\right)^2 + \cdots + \left(\frac{\partial R}{\partial X_n}U_{X_n}\right)^2} \quad (4\text{-}8)$$

Where, U_{X_1}, U_{X_2}, U_{X_3},..., U_{X_n} are the uncertainties of independent parameters.

Moreover, the uncertainties in the measurements were calculated for the forward V-grooved channel under the highest value for Reynolds number (*Re* = 1000). An example of calculation procedure for the uncertainty of dependent parameters is explained in Appendix (B). The maximum uncertainties associated with the Reynolds and Nusselt numbers and the skin friction coefficient are estimated to be ±5.26%, ±10.6%, and ±9.55 %, respectively.

CHAPTER FIVE

RESULTS AND DISCUSSIONS

CHAPTER FIVE
RESULTS AND DISCUSSION

5.1 Introduction

In this chapter, the results of the numerical simulations and experimental work for the steady forced laminar flow through the grooved rectangular channels are systematically presented. The fluid flow behaviour and heat transfer characteristics are represented in terms of pressure drop, skin friction coefficient, surface temperature, and Nusselt number. In addition, the performance evaluation criterion is displayed and evaluated for optimizing the hydrothermal performance improvement in such channels.

5.2 Verification of The Numerical Model

In order to assess the reliability and accuracy of numerical methods, the verification of obtained numerical results for the straight channel is performed. The numerical data of the average Nusselt number ($\overline{Nu}$) and the skin friction coefficient (C_f) are firstly compared with the analytical results that are reported by Shah and London [51], for thermally fully-developed laminar flow under constant heat flux boundary condition with one wall heated while the other three walls are adiabatic. The maximum deviation in the numerical results is 0.43 % for average Nusselt number and 0.51% for the skin friction coefficient (see Figure 5.1) at the aspect ratio ($AR = H/W$) of *0.5*, for the channel length (L) of 400 mm and Reynolds number (Re = 100).

Other alternative comparison between the present numerical $\overline{Nu}$ and the published $\overline{Nu}$ for thermally fully-developed forced laminar flow and four walls under constant heat flux boundary conditions with an aspect ratio of 0.2 are implemented. The maximum deviation in the $\overline{Nu}$ is 3.50%, 4.71%, and 6.49%, as compared with the corresponding data reported by Shah and

London [51], Bennett [52] and Lee et al. [53], respectively, at *Re* = 1100, for more details see Table 5.1 and Figure 5.2.

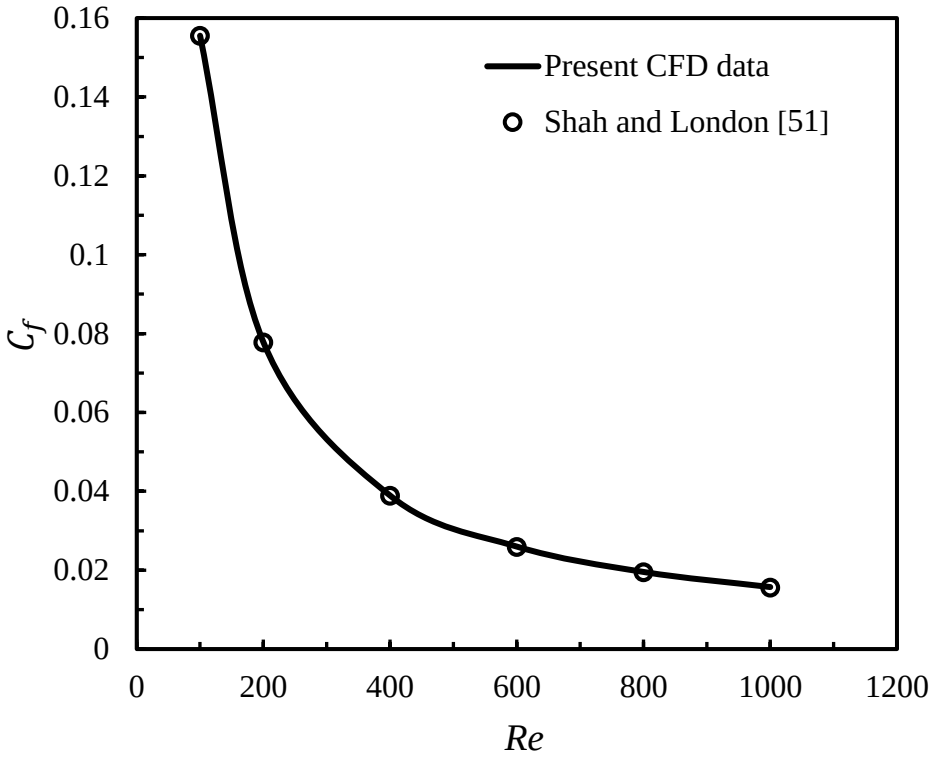

Figure. 5.1: Comparison the numerical results of the present CFD data with previous analytical data of Shah and London [51] for skin friction coefficient

Table 5.1: Comparison between the present computational simulation data of $\overline{Nu}$ and published results for fully-developed laminar flow under constant heat flux.

Present CFD data	1W, AR = 0.5 *Re* = 100	4W, AR = 0.2, *Re* = 1100		
	Shah and London [51]	Shah and London [51]	Bennett [52]	Lee et al. [53]
5.537	----------	5.738	5.811	5.921
1.846	1.854	----------	----------	----------
Dev. (%)	0.43	3.50	4.71	6.49

1W means one side heated and 4W means four sides heated.

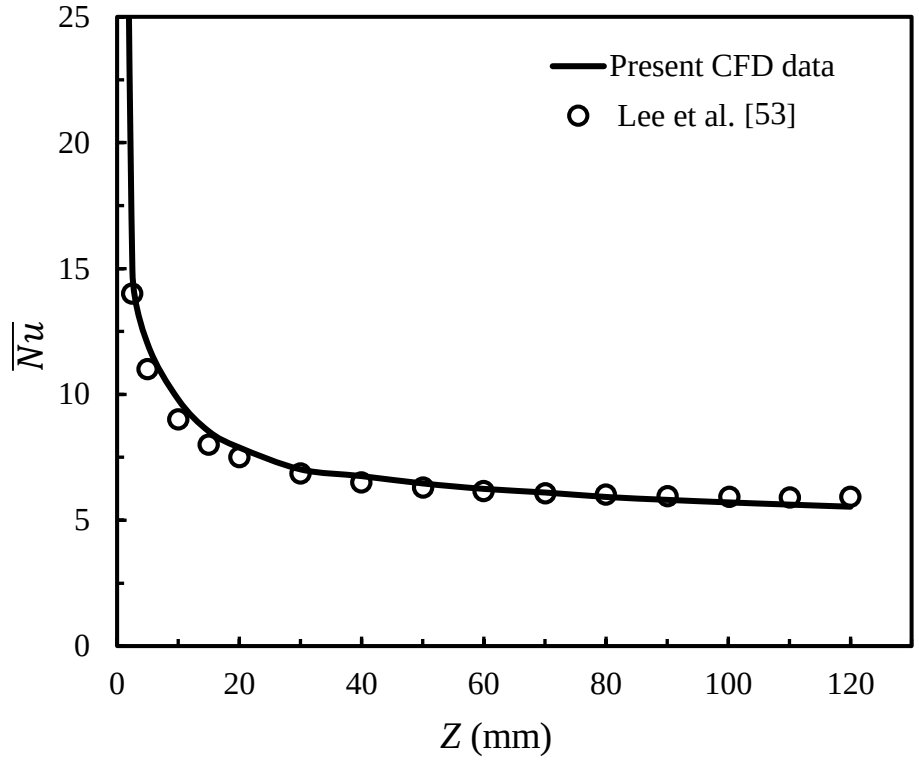

Figure. 5.2: Comparison between the present numerical data and previous numerical data of Lee et al. [53] for $\overline{Nu}$.

5.3 Comparison Between Numerical and Experimental Results

In this section, a comparison between the data of numerical simulation and the experimental results for the laminar fluid flow within the rectangular channel fitted with various shapes of grooves is presented. The results are shown for a Reynolds number range from **100(200) to 1000**, groove depth d = 2.5 mm and 15000 W/m^2 heat flux applied on the bottom surface of grooved channels. The behaviour of fluid flow and heat transfer are plotted in terms of pressure drop, skin friction coefficient, surface temperature, and Nusselt number.

5.3.1 The Influence of The Grooves on Flow Characteristics

Figures 5.3 and 5.4 illustrates the comparison between the numerical data and the experimental results for pressure-drop penalty (ΔP) and the skin friction coefficient (C_f). Three different shapes of grooved channels, which named 45°-inclined grooved channel (45°-IGCH), forward V-shape

grooved channel (F-VGCH) and backward V-shape grooved channel (B-VGCH), have been studied as well as the conventional case of the straight channel (SCH). It is clearly showed that the rate of pressure drop (ΔP) increases with the rise of Reynolds numbers for all shapes of the grooved channels for both the experimental and numerical results. From Figure 5.3, the pressure drop data for all studied grooved channels is slightly greater than the straight channel as expected in both the numerical and experimental results.

On the other hand, it can be seen that the values of skin friction coefficient (C_f) decrease with increasing Reynolds number for both the experimental and numerical results, as shown in Figure 5.4. The difference between straight and grooved channels turns to become more obvious with increasing Reynolds numbers. The maximum deviation between the numerical and experimental findings appears at low values of Reynolds number and the deviation gradually decreases with increasing Reynolds numbers. The justification behind this deviation, from experimental perspective, is due to instrument uncertainties with the measured parameters. Moreover, the pressure manometer is not sensible to accurately measure the very low pressure values.

In general, the experimental results are in a good agreement with the numerical data. The averaged deviation for all grooved channels is approximately 8.73%. As shown in Figure 5.3, at *Re* less than 400, the pressure drop in B-VGCH and 45°-IGCH is lower than in SCH while, for F-VGCH, it is remarkably greater than SCH. For *Re* beyond 400, the pressure drop of all grooved channels is slightly greater than SCH. The difference between straight and grooved channels turns to become more noticeable with the increase of Reynolds numbers for both numerical and experimental results. As a result, the skin friction coefficient (C_f) exhibits the same behaviour with respect to the pressure drop.

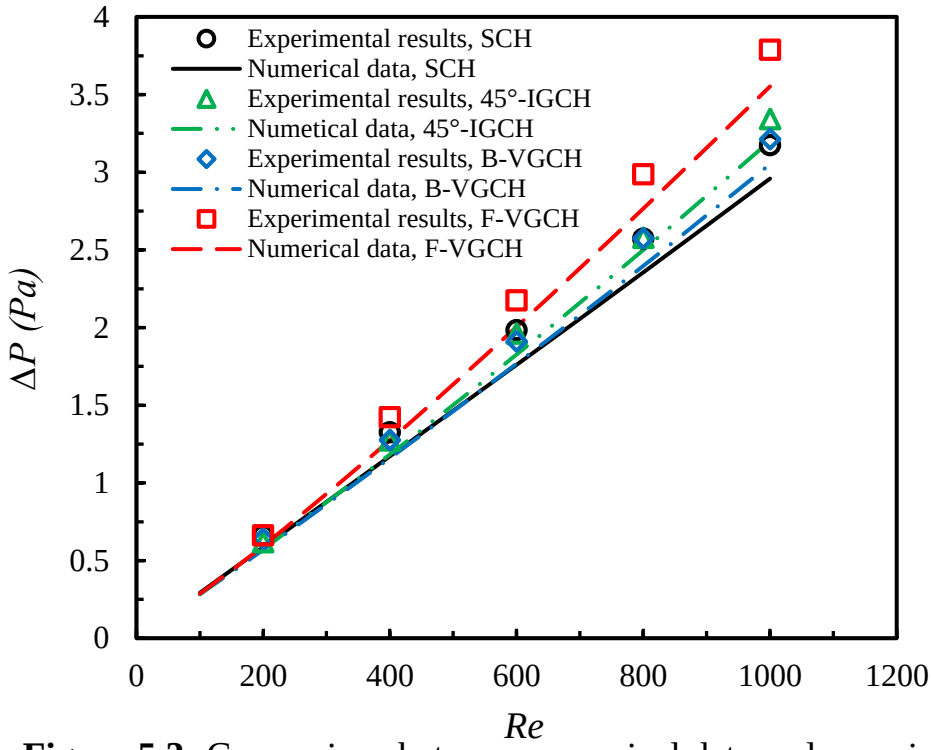

Figure 5.3: Comparison between numerical data and experimental results, Variation in pressure drop with Reynolds numbers

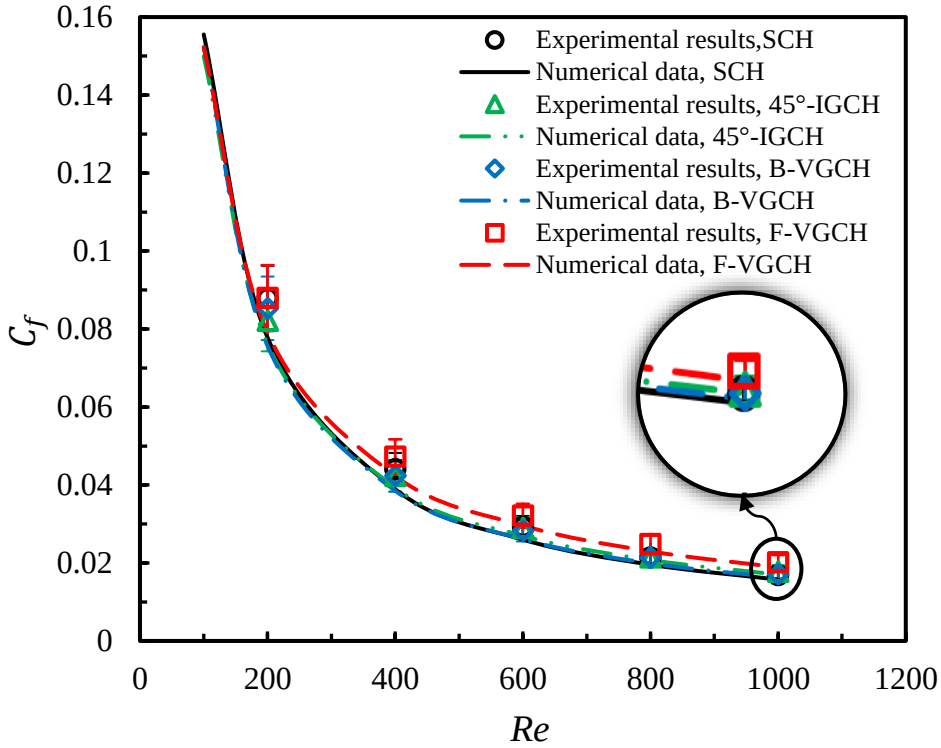

Figure 5.4: Comparison between numerical data and experimental results, Variation of skin friction coefficient with Reynolds numbers

5.3.2 The Influence of The Grooves on Heat Transfer

Figures 5.5 and 5.6 shows the comparison between the numerical data and the experimental results of surface temperature and the average Nusselt number. Three different shapes of grooved channel have been studied (45°-IGCH, F-VGCH, and B-VGCH) as well as the straight channel (SCH). It is clear that the rate of surface cooling for the grooved channels increases with increasing Reynolds numbers as compared with the straight channel for both experiments and numerical simulations results.

From Figure 5.5, the averaged Nusselt number proportionally increases with increasing Reynolds numbers for all different grooved channels. Generally, the surface temperature and the averaged Nusselt number obtained from the experimental measurements are slightly less than those of the numerical simulations for the entire range of Reynolds numbers. This is because the values of averaged Nusselt number is mainly depended on the temperature measurements which based on the inlet and outlet fluid temperatures and the surface temperature distribution, or the heat losses from walls (see Equations 4-3 to 4-6 for more details).

In a general sense, the experimental findings are quite consistent with the numerical data, and the averaged deviation of Nusselt numbers for all grooved channels is within 9.13%. Normally, this deviation of experimental measurements is attributed to the uncertainties in the measurement equipment of temperatures. Additionally, Figure 5.6 displays the analytical averaged Nusselt number for the case of thermally fully-developed laminar forced flow of Shah and London [51] and also the current results of SCH at thermally developing regime. In the case of SCH, a noteworthy convergence of results appears at the Reynolds number of 100 for the thermally fully-developed conditions, where the

channel length required to achieve the thermally fully-developed regime is 400 mm whilst the channel length used in this case (SCH) is 300 mm.

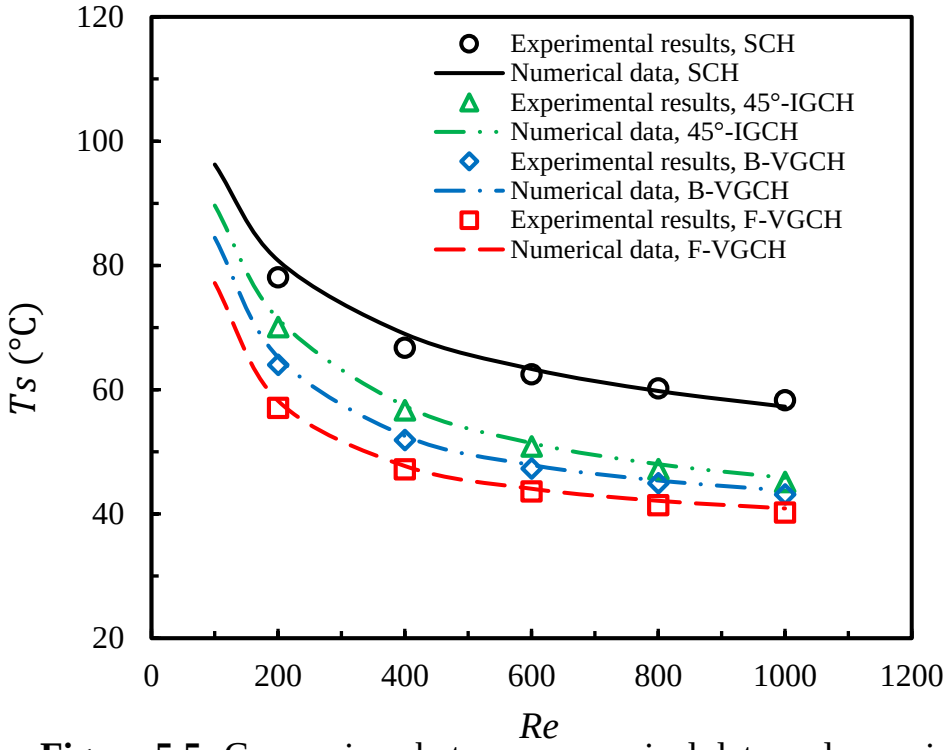

Figure 5.5: Comparison between numerical data and experimental results, Variation of surface temperature with Reynolds numbers

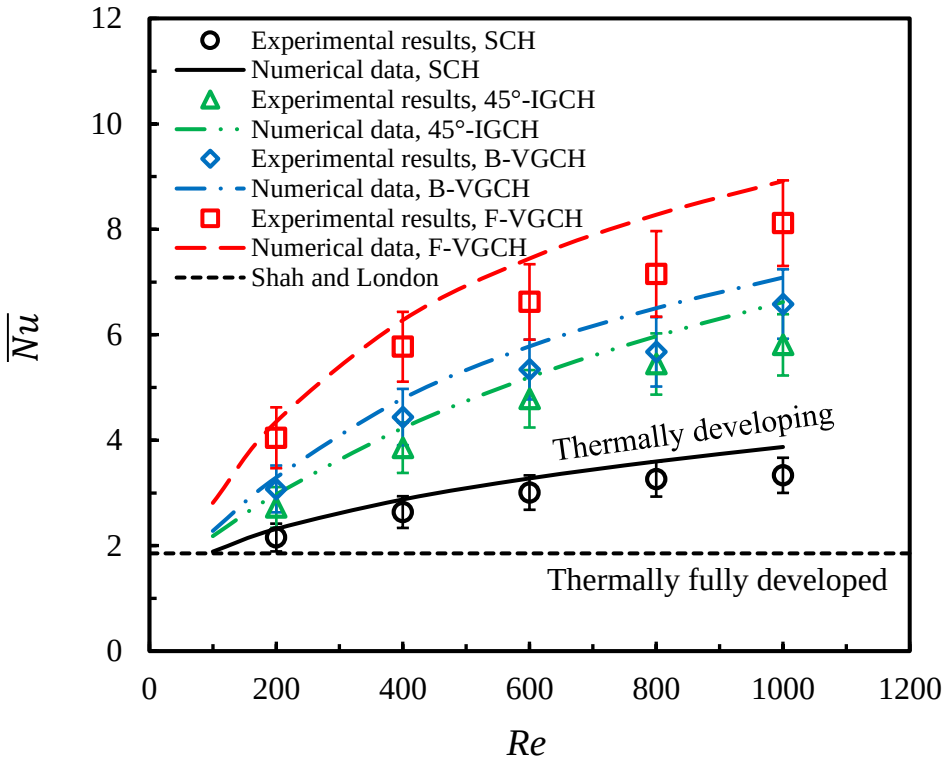

Figure 5.6: Comparison between numerical data and experimental results, Variation of average Nusselt number with Reynolds numbers

Figure 5.6 reveals that F-VGCH has the highest values of $\overline{Nu}$ followed by B-VGCH, 45-IGCH, and SCH for both numerical and experimental results.

5.3.3 The Influence of The Grooves on The *PEC*

Passive modification methods such as grooves that are employed for enhancing heat transfer are usually accompanied by an increase in losses due to effect of friction. Thus, the net enhancement gained in the grooved channels should be evaluated. As mentioned above, the grooved channels with different groove shapes can enhance the thermal performance of the rectangular channels, meanwhile, the friction losses rise in both numerical and experimental investigations.

Figure 5.7 illustrates that the numerical and the experimental findings of the performance evaluation criterion adopting in this study against Reynolds numbers. The *PEC* values calculated from Equation (3-13) depend on the comparison between the averaged Nusselt number enhancement ratio $\left(\overline{Nu}_{,G}/\overline{Nu}_{,S}\right)$ and the skin friction coefficient ratio $\left(C_{f,G}/C_{f,S}\right)$. It is noted that when the values of *PEC* are more than unity, it means there is a remarkable enhancement in the overall performance of grooved channels. It is clear from Figure 5.7 that the *PEC* increases with the rise of the Reynolds numbers for the different shapes of grooved channels in both experimental and numerical results. Meanwhile, the F-VGCH exhibits better evaluation performance followed by B-VGCH and 45°-IGCH. The variation in the amount of *PEC* between experimental and numerical results is attributed to the uncertainty of the experimental measurements as mentioned above. The *PEC* values of the numerical and experimental results are 2.18 and 2.29 at *Re* = 800 and *Re* = 1000, respectively, for F-VGCH and the average deviation for all different shapes of grooved channels is within 2.56 %. The *PEC* values

are greater than unity for all grooved channels as depicted in Figure 5.7 over the studied range of Reynolds numbers. Therefore, the utilization of grooves on the bottom surface of the rectangular channels is useful for enhancing thermal performance.

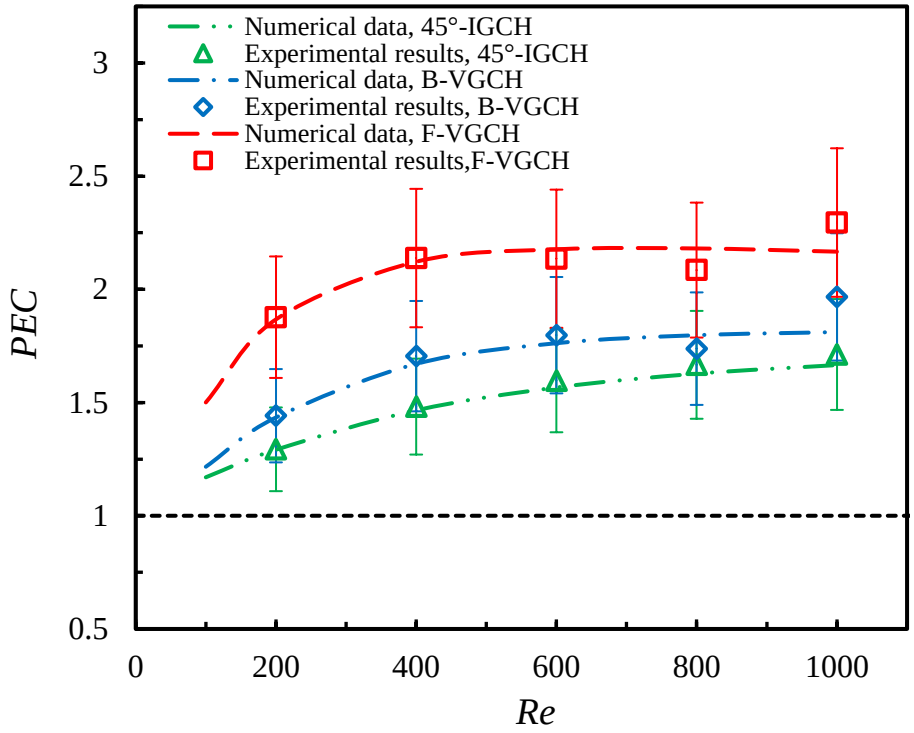

Figure 5.7: The variation in the numerical and experimental values for performance evaluation criterion versus Reynolds numbers

5.4 Numerical Results

In this section, the numerical results are systematically detailed for the laminar forced fluid flow in the rectangular channel with various shapes of the grooves. The numerical results are presented for a range of Reynolds numbers from 100 to 1000 with 15000 W/m^2 applied heat flux on the bottom surface of the grooved channels. The influence of groove shapes and groove depths is comprehensively studied as well. The characteristics of fluid flow and heat transfer are displayed in terms of pressure drop, skin friction coefficient, surface temperature, and Nusselt number. In addition, the performance evaluation criterion is exhibited in

order to evaluate the hydrothermal performance improvement in such channels.

5.4.1 The Effect of Groove Shapes

5.4.1.1 Characteristics of Fluid Flow

The effect of various groove shapes are compared with the straight channel (SCH) for groove depth of d = 2.5mm. Three different shapes of grooved channels (45°-IGCH, F-VGCH, and B-VGCH) are examined in this study as well as the straight channel (SCH). The grooves were formed on the bottom surface of the channel and arranged into five cycles, where each cycle involves five grooves formed along with the longitudinal channel direction. The flow resistance of fluid flow through the rectangular channel is raised because of the viscous flow behaviour.

Figures 5.8 and 5.9 displays the variations in the pressure drop (ΔP) and skin friction coefficient (C_f) through SCH and selected grooved channels versus Reynolds number. Generally, the values of pressure drop for both SCH and grooved channels is significantly increased with the rising of Reynolds numbers. In addition, when *Re* is lower than 200, the pressure drop across the 45°-IGCH, F-VGCH and B-VGCH is approximately similar to SCH. This indicates that channels with these grooves can decrease flow friction to a certain extent. Since, the main-stream flow moves over the grooves as fluid passes through a grooved channel, viscous resistance exists not just between the fluid and the channel walls, but also between the fluid and the fluid within the grooves. There is considerably lower friction between fluid and fluid than between fluid and solid walls. For *Re* beyond 400, the pressure drop of all grooved channels is slightly greater than SCH and the difference between straight and grooved channels turns to become more obvious with the increase of Reynolds numbers. It can also be seen from Figure 5.9 that the skin friction

coefficient (C_f) of F-VGCH is slightly higher than that of the other channels, in which the difference between them decreases as the Reynolds number decreases. For example, when Re = 1000, the relative difference between F-VGCH and SCH is 16.7%, and between F-VGCH and B-VGCH is about 14.1%, and between F-VGCH and 45°-IGCH is 9.9%. For the flow with Re = 400, the relative difference between F-VGCH and SCH is 8.1%, and between F-VGCH and B-VGCH is 9.0%, and between F-VGCH and 45°-IGCH is 7.1%. This variation in the skin friction coefficient is a result of disturbing behaviour of fluid flow inside the grooved channels, where the presence of the grooves creates kind of secondary flows that perpendicular on the downstream. The amount and direction of these secondary flows vary according to the shape of grooves and also alter with the intensity of inertia effect (the magnitude of velocity) on the flow stream. The direction of these secondary flows tilts with the direction of the grooves, and their shape changes after the end of each cycle. Thus, working to change the shape of the velocity profile and lead to mixing the fluid.

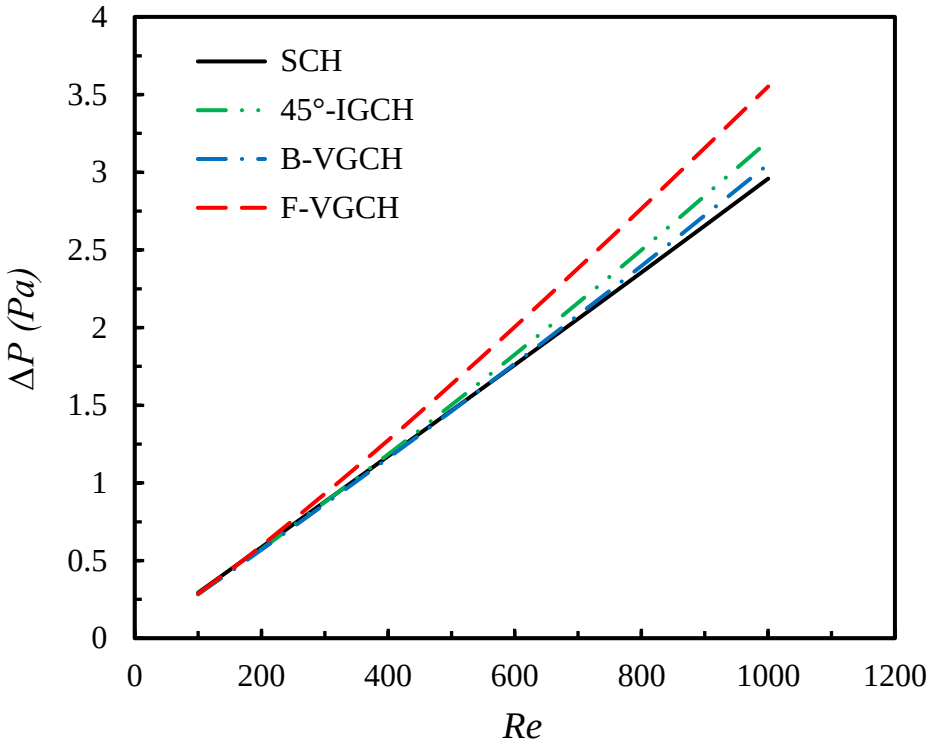

Figure 5.8: Numerical data for grooved channels and straight channel, Variation of pressure drop versus Reynolds numbers

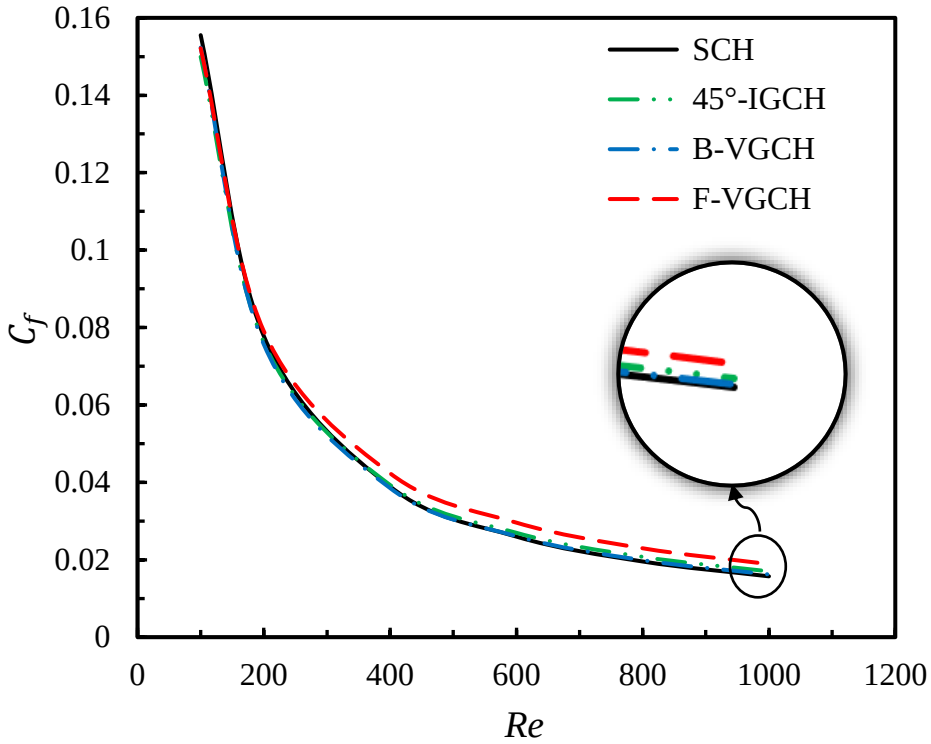

Figure 5.9: Numerical data for grooved channels and straight channel, Variation of skin friction coefficient versus Reynolds numbers

In order to interpret the behaviour and structure of fluid flow within the rectangular channels for different groove shapes, the velocity contours of flow are depicted in the axial and cross-sectional planes of grooved channels. Figures 5.10 and 5.11 illustrate the simulated velocity contours (flow features) of SCH and 45°-IGCH with d = 2.5mm groove depth at Re = 200 and 1000. The velocity contours for 45°-IGCH are presented for the axial flow plane near the bottom surface and also the cross-sectional flow plane, which is perpendicular to the main flow, at six different locations along the 45°-IGCH. The existence of these grooves encourages creating secondary flow in the streamwise direction.

As portrayed in Figure 5.10 and Figure 5.11, the first cross-sectional plane, which lies at the channel inlet, shows fully-developed velocity profile of flow. When the fluid passes over these inclined grooves, the secondary flow is generated. The direction of these secondary flows is tilted with the direction of the inclined grooves. At the end of each cycle, the secondary flows are axially reversed with cycle direction, i.e., flipping the flow direction over [54], as shown in Figure 5.10. The generated secondary flows are working to switch the shape and direction of velocity profiles from the underside (near the grooved surface) and thus enhance the mixing of fluid. The effect of grooves on the velocity profiles is marginal at low Reynolds number due to the large thickness of the boundary layer and the viscous influence of working fluid. The impact of these secondary flows increases with an increase in the Reynolds number (increasing velocity magnitude) owing to the reduction of the boundary layer thickness and the fluid momentum.

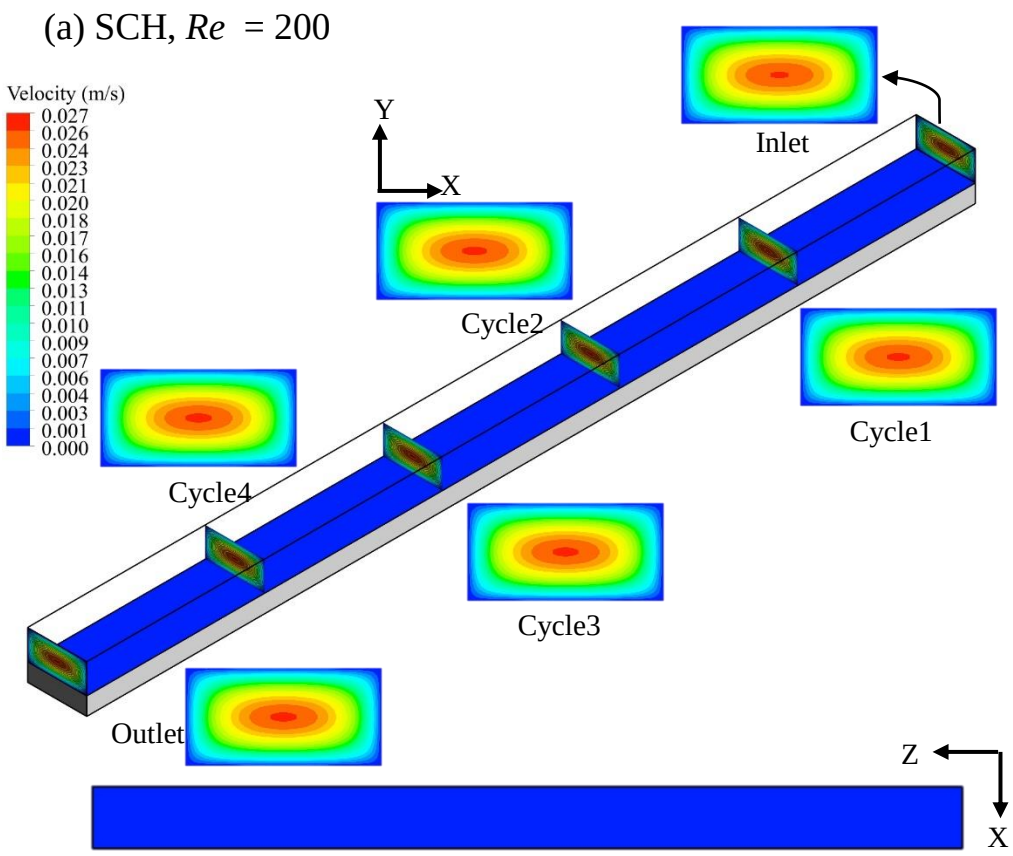

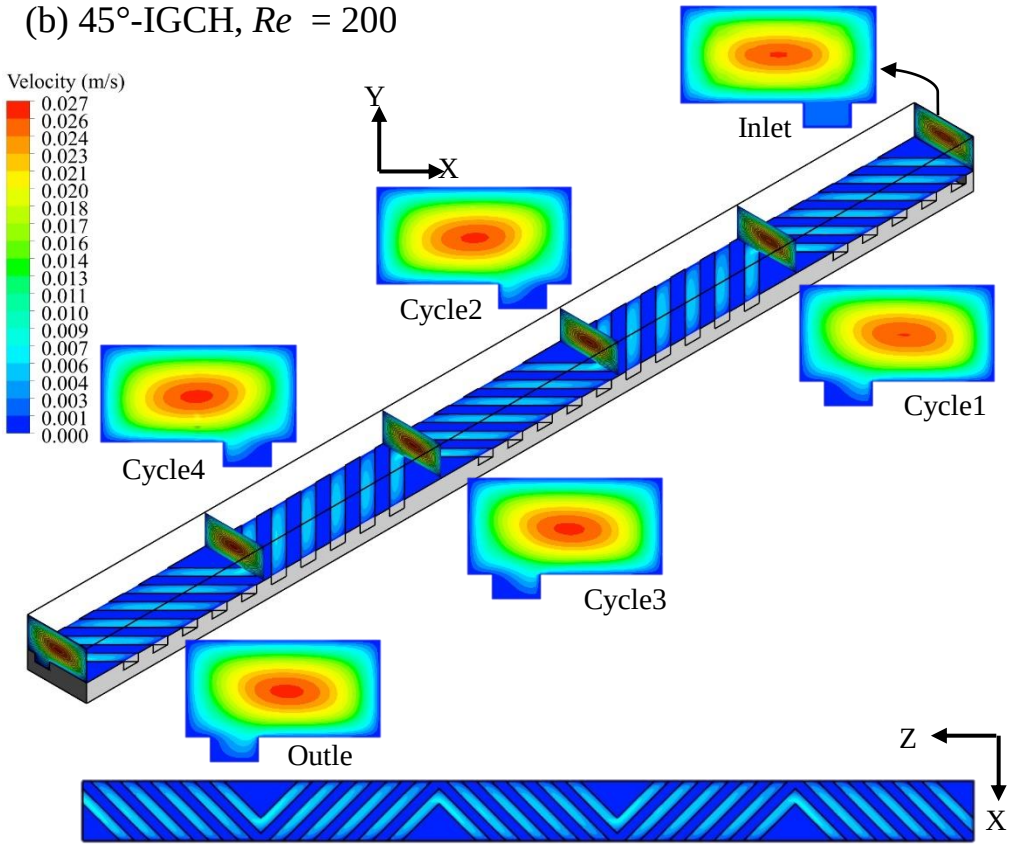

Figure 5.10: Velocity contours for (a) SCH, (B) 45°-IGCH at *Re* = 200

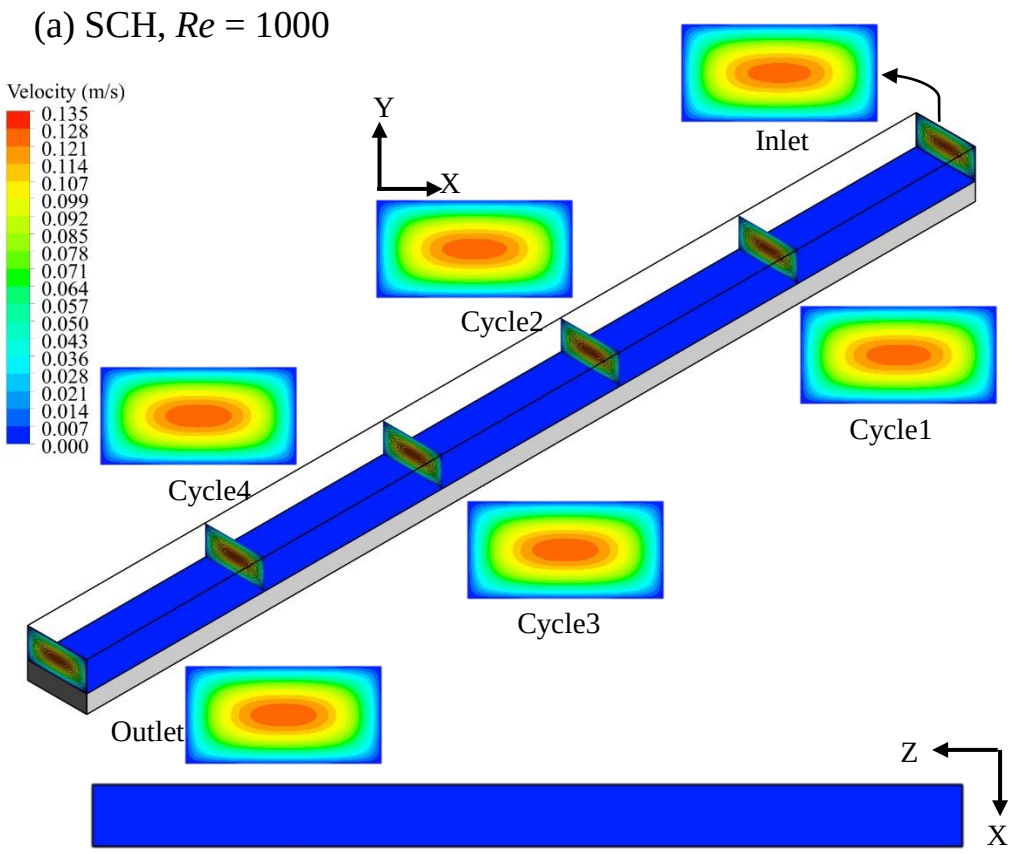

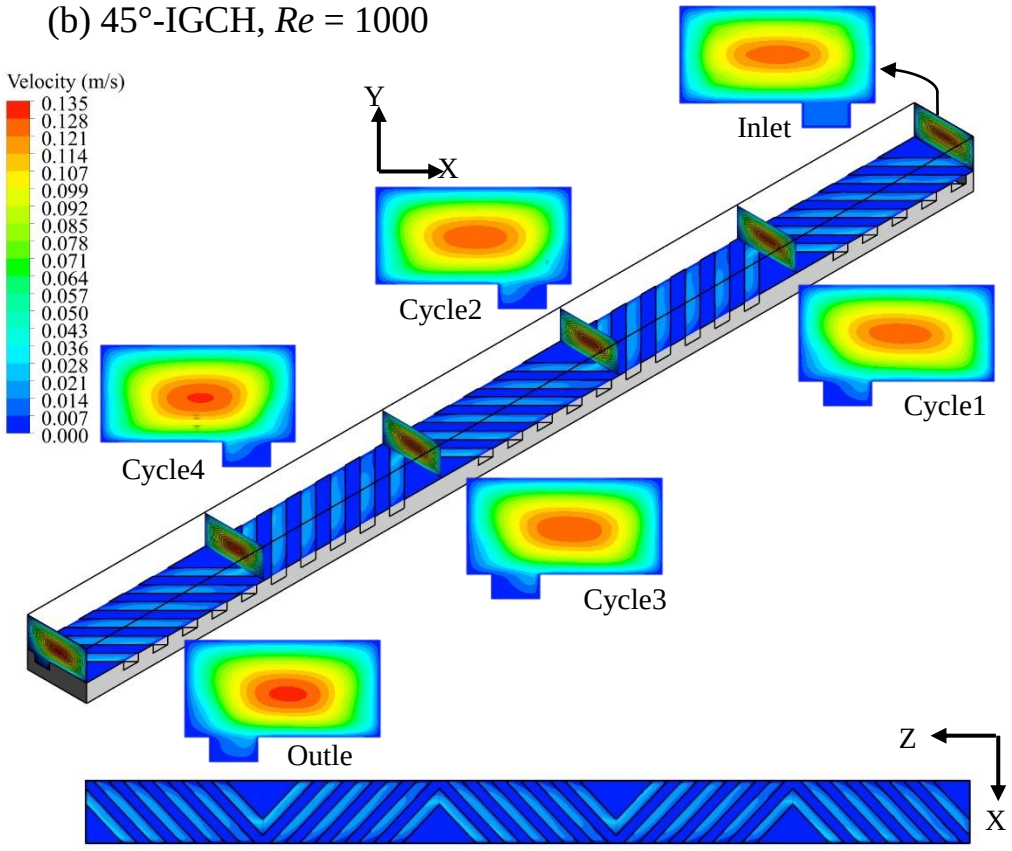

Figure 5.11: Velocity contours for (a) SCH, (B) 45°-IGCH at *Re* = 1000

Figures 5.12 and 5.13 display the simulated velocity contours of B-VGCH and F-VGCH with groove depth d = 2.5mm for Re = 200 and 1000, respectively. As expected, the first cross-sectional plane shows fully-developed velocity profile for both B-VGCH and F-VGCH because the flow at the channel inlet is hydrodynamically fully-developed as supposed. The presence of grooves makes the structure of fluid flow in the forward and backward V-grooved channels different from that in the straight channel. The fluid velocity in the zones of grooves is lower than that on the surface of grooved channel because of the suddenly expanded cross-sectional area, as depicted in Figures 5.12 and 5.13.

From the numerical results, the velocity profiles of fluid flow in these grooved channels point out that two categories of secondary flows are generated in each V-shape groove. The direction of these secondary flows alters depending on the forward and backward directions of the V-shape groove that printed on the bottom surface of channel. It is noted from Figure 5.13 (a), for B-VGCH there are two counter-rotating vortices due to the incline angle of each groove, its direction is tilted from both sides of the channel towards the center from the bottom in the streamwise direction for the axial flow. The generated secondary flows are working to switch the shape of velocity profiles from the underside, i.e., near the center of the grooved surface, and thus boost the mixing of fluid.

On the other hand, for F-VGCH, also two groups of secondary flows generated and their directions are tilted from the center of the channel towards both sides from the bottom. Consequently, more fluid mixing occurs in the B-VGCH because of the generated secondary flows, which are working to change the shape of the velocity profiles from the two sides toward the side-walls. These two streams of secondary flows that generated in the cross-sectional direction are axially reversed with the

groove directions at the end of each cycle for both B-VGCH and F-VGCH. The influence of V-grooves on the velocity profiles is marginal at low Reynolds numbers due to the large thickness of the boundary layer and viscous effect of fluid. The impact of V-grooves increases with increasing Reynolds number (increasing velocity magnitude) due to decrease in the thickness of the boundary layer and also the increasing of fluid momentum.

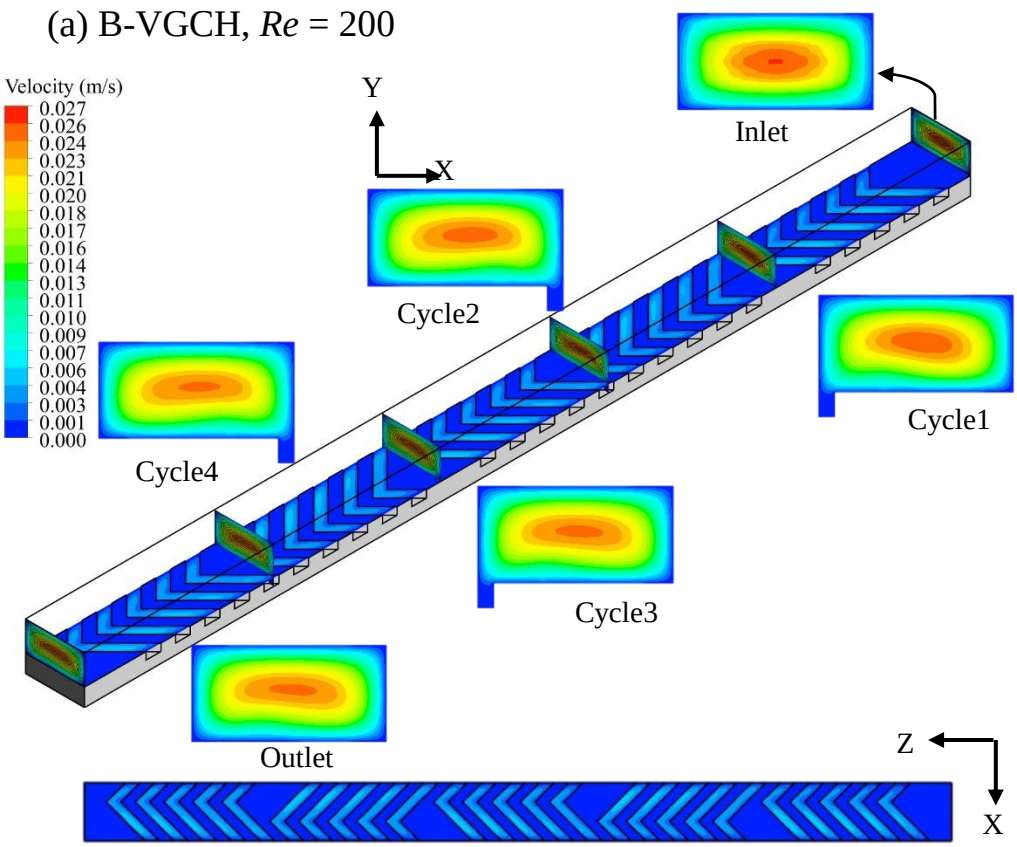

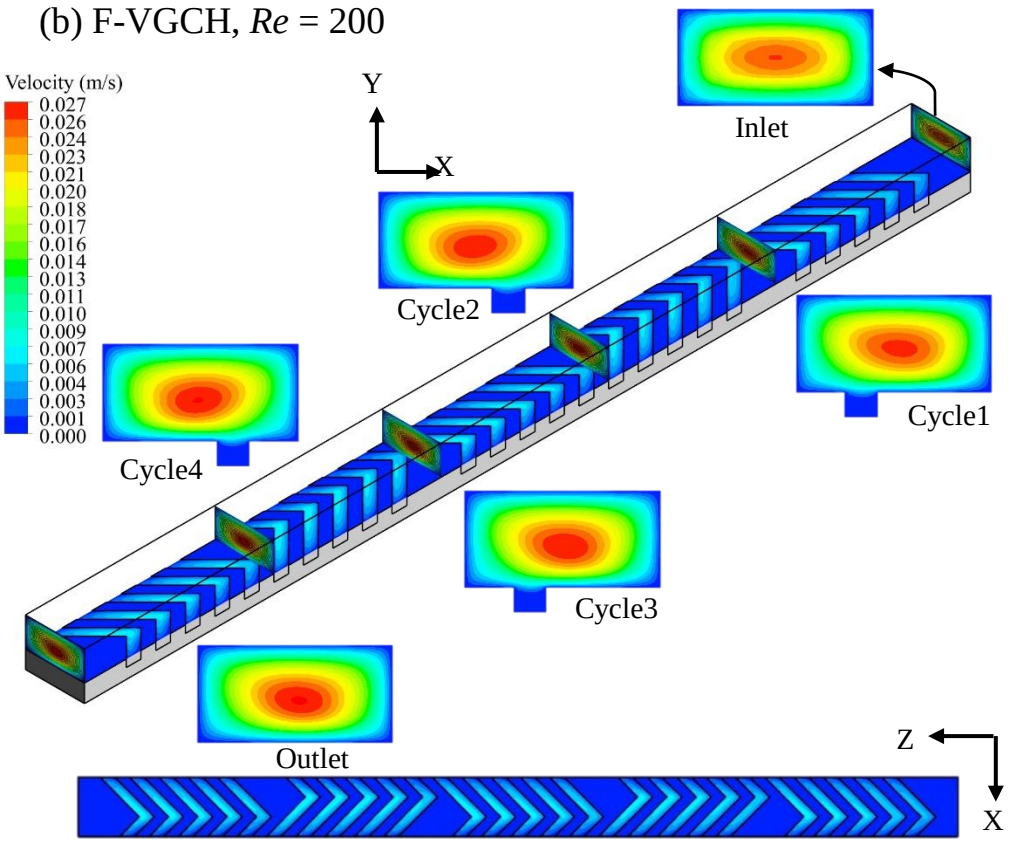

Figure 5.12: Velocity contours for (a) B-VGCH, (B) F-VGCH at *Re* = 200

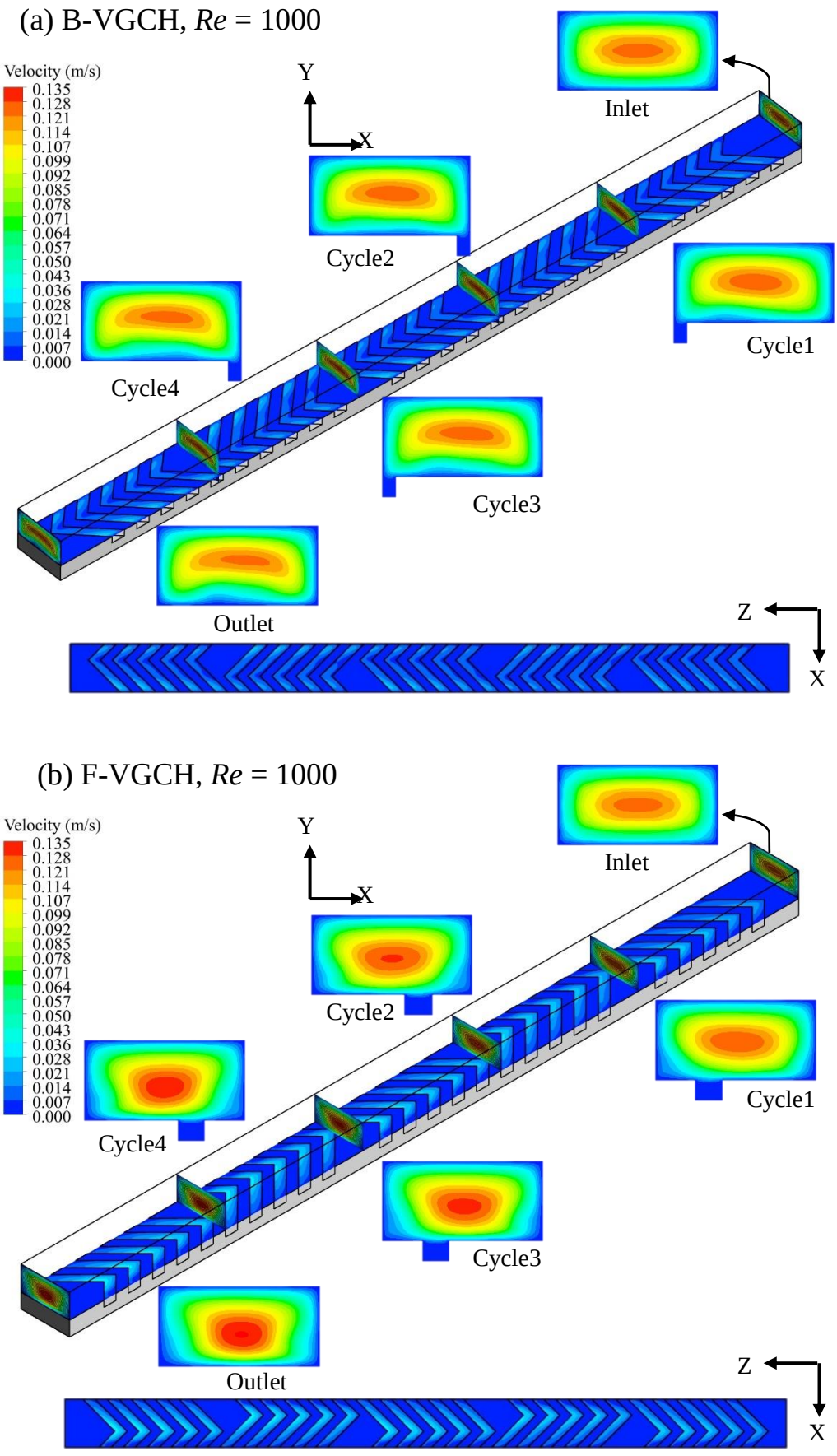

Figure 5.13: Velocity contours for (a) B-VGCH, (B) F-VGCH at *Re* = 1000

Figure 5.14 illustrates the simulated velocity contours in Y-Z plane along the channel for SCH and grooved channels at *Re* =1000. It can be seen that the velocity profile is fully developed along the SCH from inlet to outlet with a uniform distribution of velocities, while in the other grooved channels, the distribution of velocities slightly change especially in the lower half of the channel near the grooves due to secondary flow as mentioned previously.

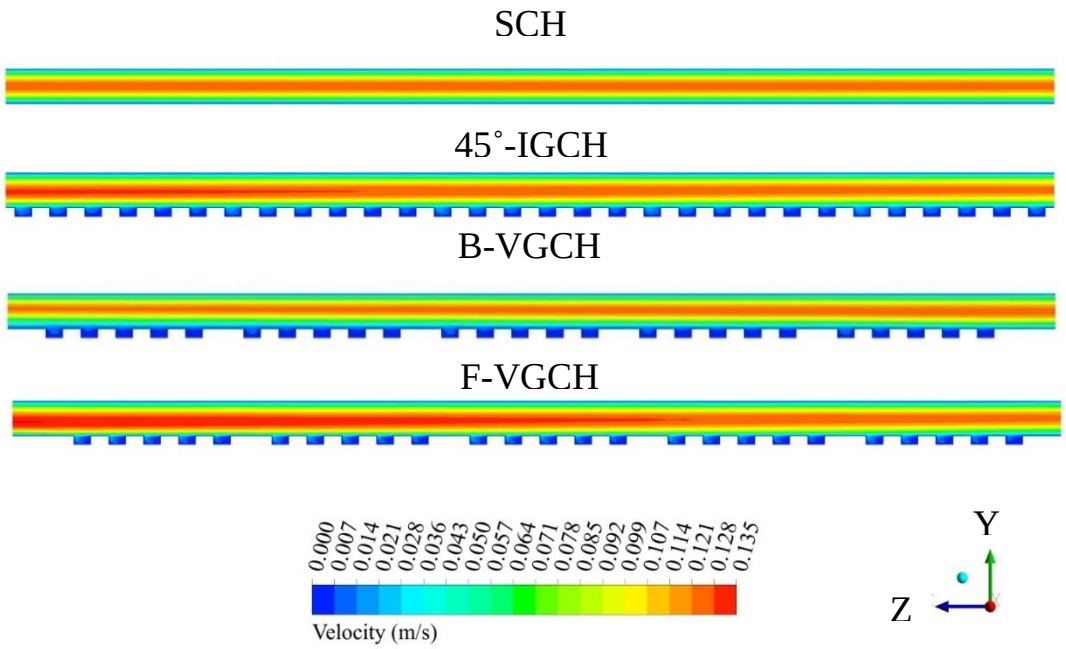

Figure 5.14: Velocity contours for SCH, 45°-IGCH, B-VGCH, and F-VGCH at Re = 1000

5.4.1.2. Characteristics of Heat Transfer

The generated secondary flows are able to enhance the fluid mixing in the streamwise direction, which means promote the mixing of cold fluid in the channel core with the hot fluid near the heated wall of the grooved channel. As a result, the thickness of the thermal boundary layer reduces and the temperature gradient at the walls of the channel increases and hence increases the heat transfer rate. Figures 5.15 and 5.16 presents the variation of surface temperature, T_s, and average Nusselt number, $\overline{Nu}$ respectively versus Reynolds numbers for both straight and grooved

channels at groove depth d = 2.5 mm. It is clearly showed that the surface temperature decreases with the rise of Reynolds numbers for different shapes of the grooved channels as compared with the straight channel. Also, the SCH (the channel without grooves) displays the highest value of T_s due to poor fluid mixing, i.e., no secondary flow is generated. From Figure 5.15, F-VGCH has the lowest value of T_s, i.e., the highest wall cooling rate, due to the high mixing of fluid then followed by B-VGCH, and 45°-IGCH. As in the case of T_s, it is obvious that the average Nusselt number increases with the increase of Reynolds numbers for all grooved channels owing to the increase of temperature gradients at the heated bottom wall of these grooved channels, as shown in Figure 5.16.

As expected, the SCH has the lowest value of ($\overline{Nu}$) as compared with the grooved channels ($\overline{Nu} = 1.89\ at\ Re = 100, and\ \overline{Nu} = 3.87\ at\ Re = 1000$). The numerical data shows that F-VGCH has the highest value of the $\overline{Nu}$, then followed by B-VGCH, and 45°-IGCH. It can be observe that F-VGCH has a great improvement in heat transfer because it has the best mixing of fluid, which increases with Reynolds numbers. For example, for groove depth d = 2.5 mm and when Re = 100, the $\overline{Nu}$ for F-VGCH, B-VGCH and 45°-IGCH are 1.49, 1.21 and 1.16, respectively, times that of basic SCH, while for Re = 1000, the $\overline{Nu}$ of F-VGCH, B-VGCH and 45°-IGCH is 2.30, 1.83 and 1.71, respectively, times that of basic SCH. In addition, Figure 5.16 displays a comparison between analytical averaged Nusselt number for thermally fully-developed laminar flow of Shah and London [51] with the current data of SCH at thermally developing region.

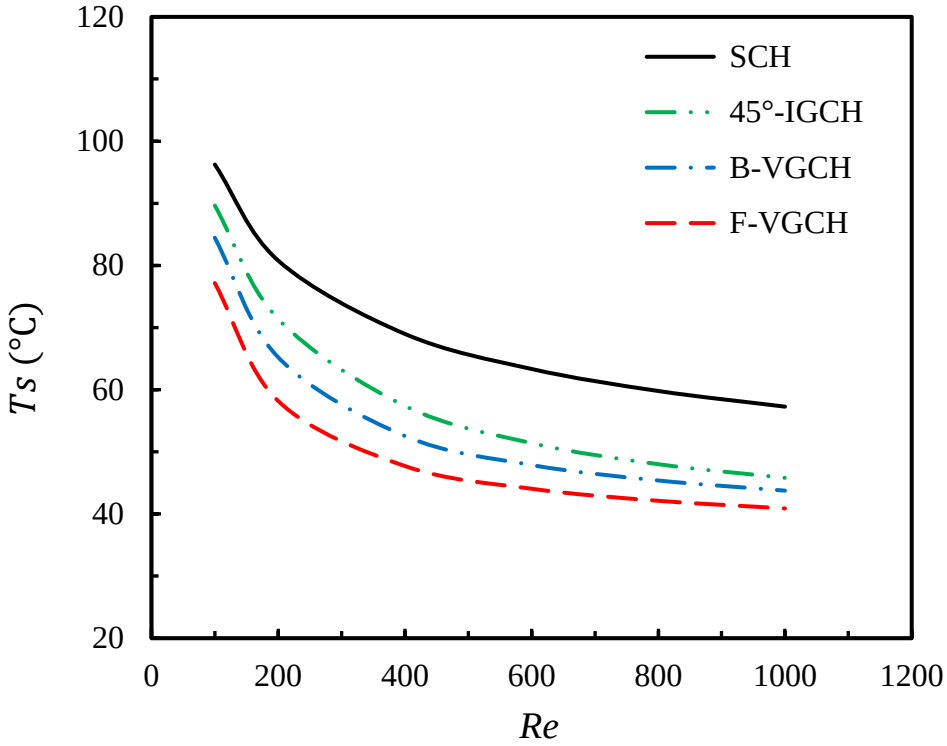

Figure 5.15: Numerical data for both grooved and straight channels, Variation of surface temperature versus Reynolds numbers

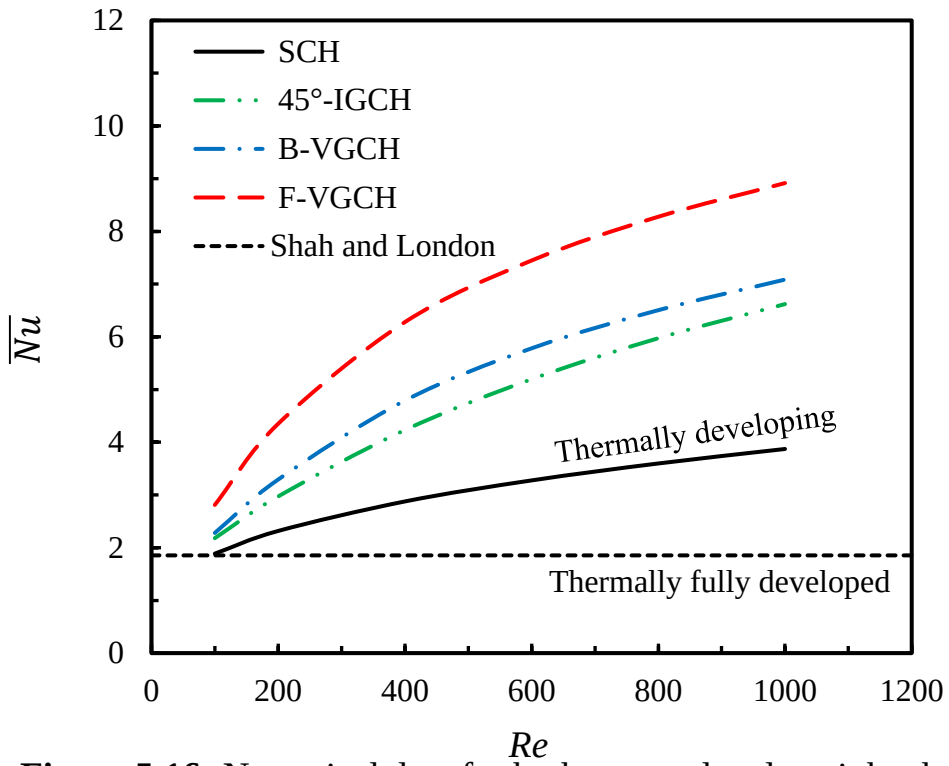

Figure 5.16: Numerical data for both grooved and straight channels, Variation of average Nusselt number versus Reynolds numbers

Figures 5.17 and 5.18 display the contours of the temperature field for SCH and 45°-IGCH with groove depth $d = 2.5mm$ at Re = 200 and 1000. The temperature distributions on the heated channel wall are presented in the axial planes and in the cross-sectional planes at each cycle, i.e., at six different locations along the grooved channel. The entry temperature profile (at the inlet plane) is identical in both channels; however, the temperature profile significantly changes in the axial direction of 45°-IGCH compared with SCH. This means that the generated secondary flow within the grooves provides an important effect on the temperature field because it can induce better fluid mixing between the hot fluid near the heated wall and the cold fluid in the core regions. This can lead to a high-temperature gradient over the heated wall of the channels. By compare the temperature contour with the velocity contour for 45°-IGCH (Figures 5.10 (b) and 5.11 (b)), it can be seen that the secondary flow regions have a higher thermal gradient than the other regions of the velocity profile. After the end of each cycle, it is axially reversed with the groove directions.

It is worthwhile that the fluid temperature in the SCH increases with channel length because the thermal boundary layer is developing along the longitudinal direction, while in the 45°-IGCH, the increase of surface temperature is less than SCH because the grooves lead to reduce the thickness of thermal boundary layer. Therefore, the rate of heat transfer through the 45°-IGCH rises as clearly depicted in the cross-sectional planes along the channel. In addition, the rate of convective heat transfer between the flowed fluid and the bottom grooved surface is significantly increased with increasing Re, as shown in Figure 5.18 (b).

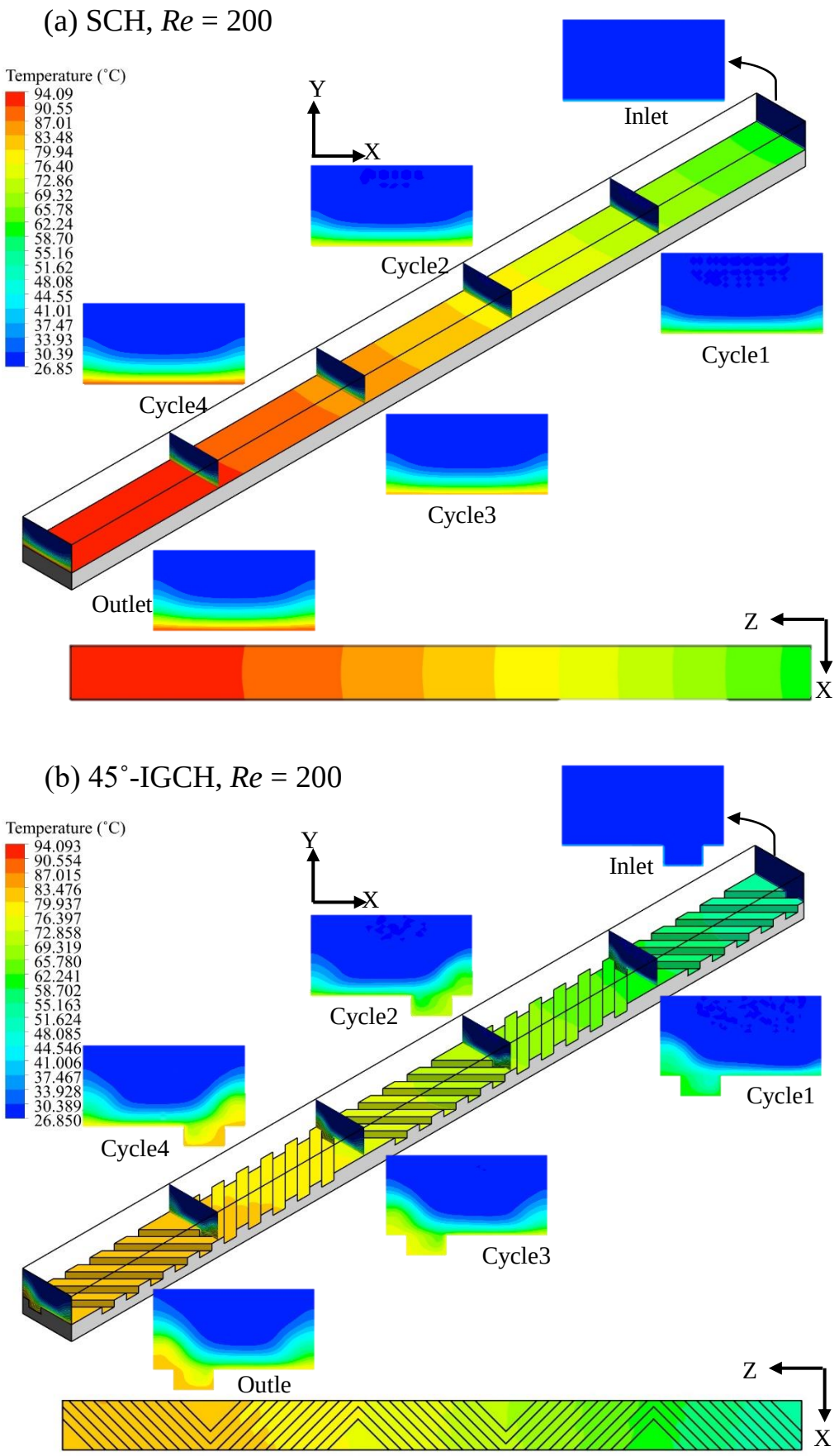

Figure 5.17: Temperature contour for (a) SCH, (B) 45˚-IGCH at *Re* = 200

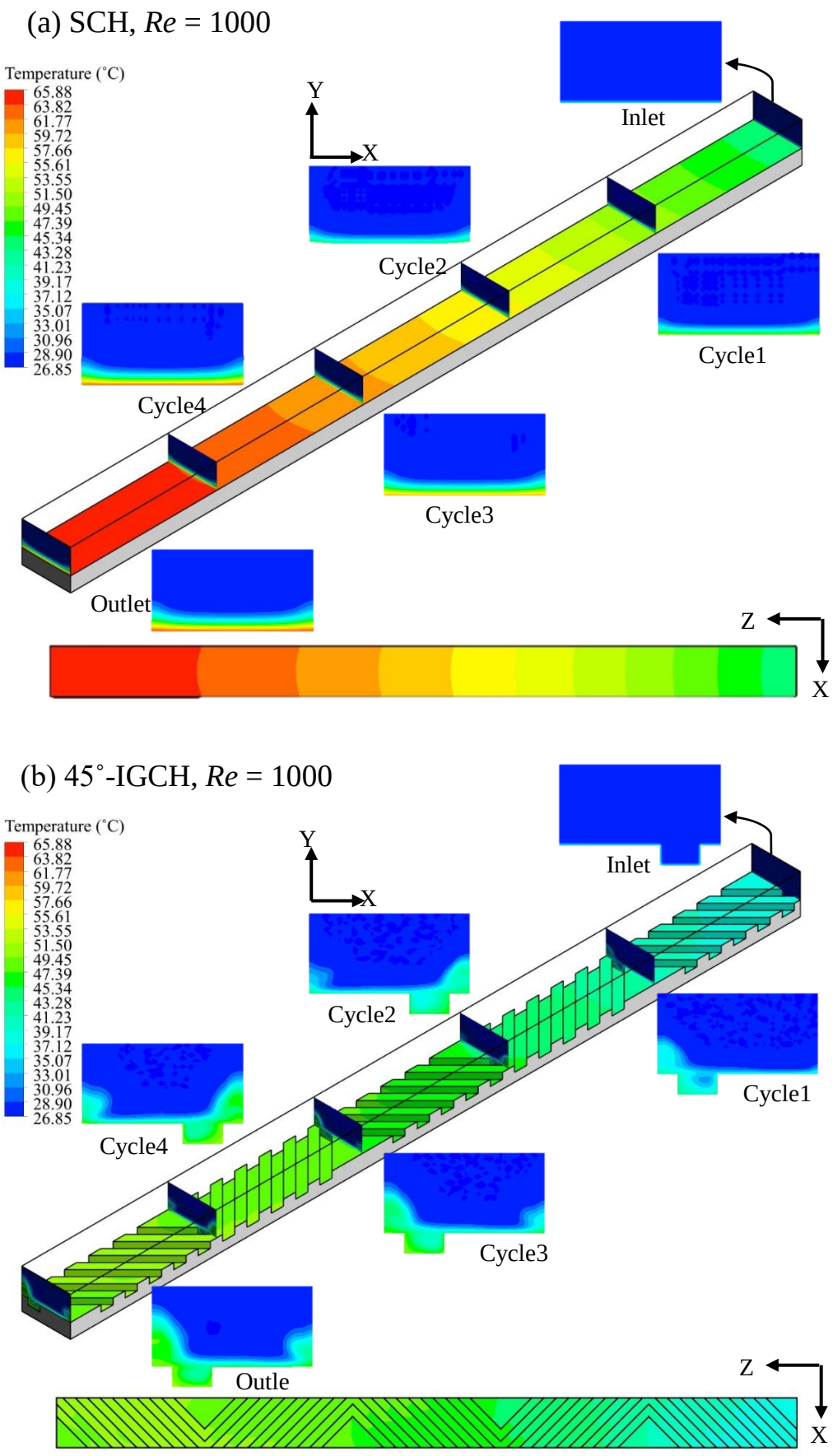

Figure 5.18: Temperature contour for (a) SCH, (B) 45°-IGCH at *Re* =1000

Figures 5.19 and 5.20 display the contours of temperature field for B-VGCH and F-VGCH with groove depth d = 2.5mm at Re = 200 and 1000. They depict temperature distributions on the grooved wall in the axial planes and bulk temperature of the fluid in the cross-sectional planes at the end of each cycle, i.e., six different locations along the grooved channels. The inlet spanwise plane temperature which exemplifies the inlet bulk fluid temperature, is the same in both V-grooved channels (B-VGCH and F-VGCH) for Re = 200 and 1000. However, there is a major change in the temperature field in B-VGCH and F-VGCH as compared with SCH along the channel. This means that the generated secondary flows possess an important impact on the temperature field because they are able to induce a noticeable fluid mixing between the hot fluid near the heated grooved surface and the cold fluid in the channel core region, leading to a high gradient in the temperature over the heated wall of channels. Returning to the figures of velocity contours for B-VGCH and F-VGCH (see Figures 5.12 and 5.13), it can be observed that the spanwise secondary flows have a significant influence on the temperature gradients. As mentioned previously the surface temperature of SCH increases along the channel due to the developing of thermal boundary layer along this direction, while in the B-VGCH and F-VGCH, the increase in the surface temperature is less than that for SCH because of the V-groove effects. The V-grooves could lead to reduce or sometimes break down the thickness of the thermal boundary layer thereby, the rate of heat transfer through the B-VGCH and F-VGCH can be enhanced. In B-VGCH, the rate of heat transfer is significantly enhanced between the heated V-grooved surface and the fluid flow downstream and its magnitude increases at the end of each cycle and with increasing travelled distance due to the amount of fluid mixing as shown in Figures 5.19 and 5.20. Furthermore, the fluid temperature gradient considerably takes place at the bottom of the grooved

surface of F-VGCH towards the side walls and then reverses and increases in its magnitude and intensity at the end of each cycle. With increasing the travelled length of the fluid flows, the rate of heat transfer increases owing to the increase of fluid mixing. It is worthwhile that, in the case of F-VGCH, the intensity of thermal gradient is greater than the other grooved channels (B-VGCH and 45°-IGCH) because the direction of reversal secondary flows tends in the opposite direction and towards the side walls particularly at the end of each cycle.

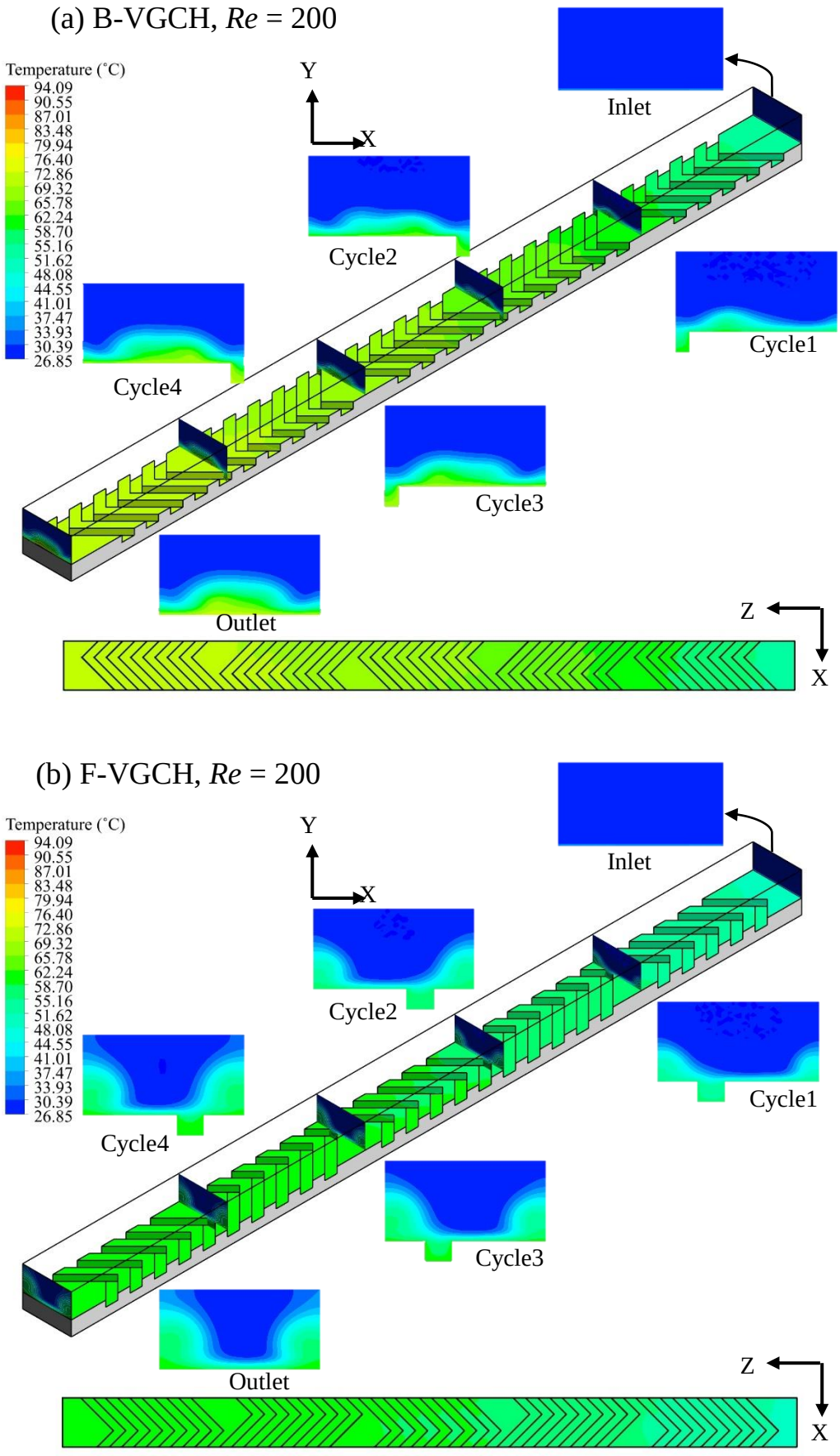

Figure 5.19: Temperature contour for (a) B-VGCH, (B) F-VGCH at *Re* = 200

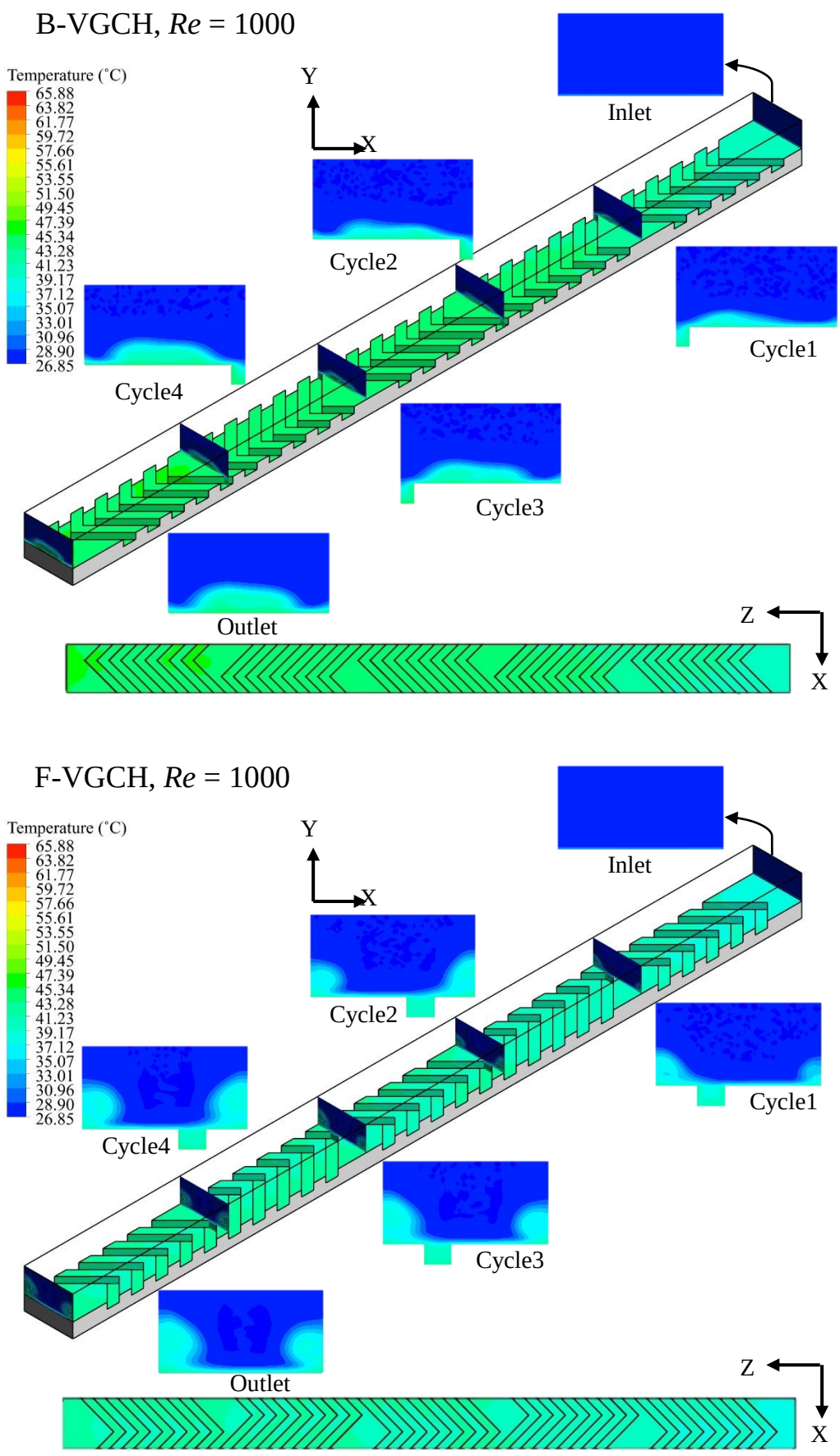

Figure 5.20: Temperature contour for (a) B-VGCH, (B) F-VGCH at *Re* = 1000

5.4.1.3 The Performance Evaluation Criterion (*PEC*)

Basically, hydrothermal performance is significantly depended on the friction coefficient and the amount of enhancement in heat transfer within the channel flow. Despite the utilization of rectangular grooved channels that involved different types of grooves leads to an enhancement of heat transfer and correspondingly an increase in the penalty of pressure drop. Therefore, it is necessary to check the performance evaluation criterion (according to equation 3-13). As mentioned above, the grooved channels with different groove shapes can enhance the thermal performance of the rectangular channels, meanwhile, the power required for pumping fluid flow rises because of increasing pressure drop.

The performance evaluation criterion (*PEC*) adopting in this study against Reynolds number, as illustrated in Figure 5.21 at d = 2.5 mm. The *PEC* goes up gradually with the increase in Reynolds numbers for 45°-IGCH due to the generated secondary flows and the reduction in the thickness of the thermal boundary layer. This actually offers an increase in the $\overline{Nu}$, which accompanied with an increase in pressure drop. When the performance evaluation criterion is greater than unity, this means that the amount of $\left(\overline{Nu}_{,G}/\overline{Nu}_{,S}\right)$ is greater than of $\left(C_{f,G}/C_{f,S}\right)$. The 45°-IGCH has the lowest thermal performance as compared with B-VGCH and F-VGCH. In addition, it is found that F-VGCH possesses the highest performance over Reynolds number range and the peak value of *PEC* is 2.18 at *Re* = 800, while for B-VGCH, the peak value of *PEC* is 1.81 at *Re* = 1000. The variation in the amount of *PEC* over Reynolds number range due to the variation of the averaged Nusselt number enhancement ratio $\left(\overline{Nu}_{,G}/\overline{Nu}_{,S}\right)$ and the skin friction coefficient ratio $\left(C_{f,G}/C_{f,S}\right)$ and also the percentage of the increment of $\left(\overline{Nu}_{,G}/\overline{Nu}_{,S}\right)$ and $\left(C_{f,G}/C_{f,S}\right)$ with the rise of Reynolds numbers.

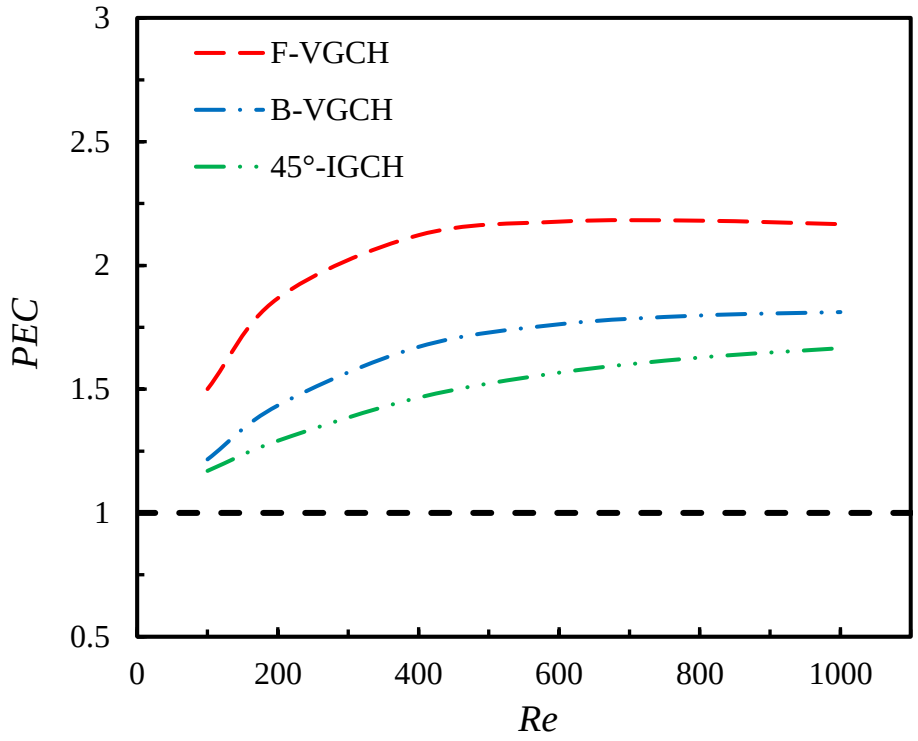

Figure 5.21: Variation of the *PEC* with Reynolds numbers for different shapes of grooved channels

5.4.2 The Effect of Groove Depths

The effect of groove depths for different shapes of grooved channels (45°-IGCH, B-VGCH, and F-VGCH) on the fluid flow and heat transfer characteristics has been considered over a wide range of Reynolds numbers of 100-1000 with 15000 W/m^2 applied heat flux on the bottom surface of grooved channels. Three different depths of grooves (d = 1.5, 2.5, and 3.5 mm) are examined in order to assess the optimal design of groove depth.

5.4.2.1 Characteristics of Fluid Flow

Figure 5.22 illustrates the variations of the skin friction coefficient C_f with Reynolds numbers for the grooved channel with three different depths printing on the bottom wall of the rectangular channels. It can be seen that the depths of grooves have a simple influence on the skin friction coefficient C_f over the entire range of Reynolds numbers. The skin friction

coefficient C_f decreases with the increase of Reynolds numbers for all groove shapes and increase with the increase of the groove depths and also the variation of the increase varied from one shape to another. This is due to the effect of the generated secondary flow that appears within the grooves and hence changing the shape of velocity profile after each cycle. At a groove depth of d = 1.5 mm (Figure 5.22 (a)), it can be seen that the highest value of the skin friction coefficient is at F-VGCH followed by 45°-IGCH and B-VGCH, respectively, and the lowest value is for SCH with high Reynolds numbers ($Re \geq 600$). Whilst at low Reynolds numbers ($Re \leq 200$), the values of skin friction coefficient of SCH are slightly greater than all other grooved channels. However, the value of skin friction coefficient for grooved channels is slightly raised with the increase of the groove depths.

For high Reynolds numbers ($Re \geq 400$) and at a groove depth of d = 3.5 mm (Figure 5.22 (c)), it can be seen that the highest value of the skin friction coefficient is for F-VGCH followed by 45°-IGCH and B-VGCH, respectively, and the lowest value for SCH. While at low Reynolds numbers ($Re \leq 200$), the values of skin friction coefficient for SCH are also slightly greater than all other grooved channels. For example, for *1.5 mm* groove depth and *Re = 100*, the $C_{f,G}/C_{f,S}$ of F-VGCH, B-VGCH and 45°-IGCH is 0.973, 0.963, and 0.964, respectively. For *Re = 1000*, the $C_{f,G}/C_{f,S}$ of F-VGCH, B-VGCH and 45°-IGCH is 1.182, 1.023 and 1.05, respectively. In addition, for *3.5 mm* groove depth and *Re = 100*, the $C_{f,G}/C_{f,S}$ of F-VGCH, B-VGCH and 45°-IGCH is 0.979, 0.962 and 0.968, respectively. Whilst for *Re = 1000*, the $C_{f,G}/C_{f,S}$ of F-VGCH, B-VGCH

and 45°-IGCH is 1.196, 1.024 and 1.118, respectively.

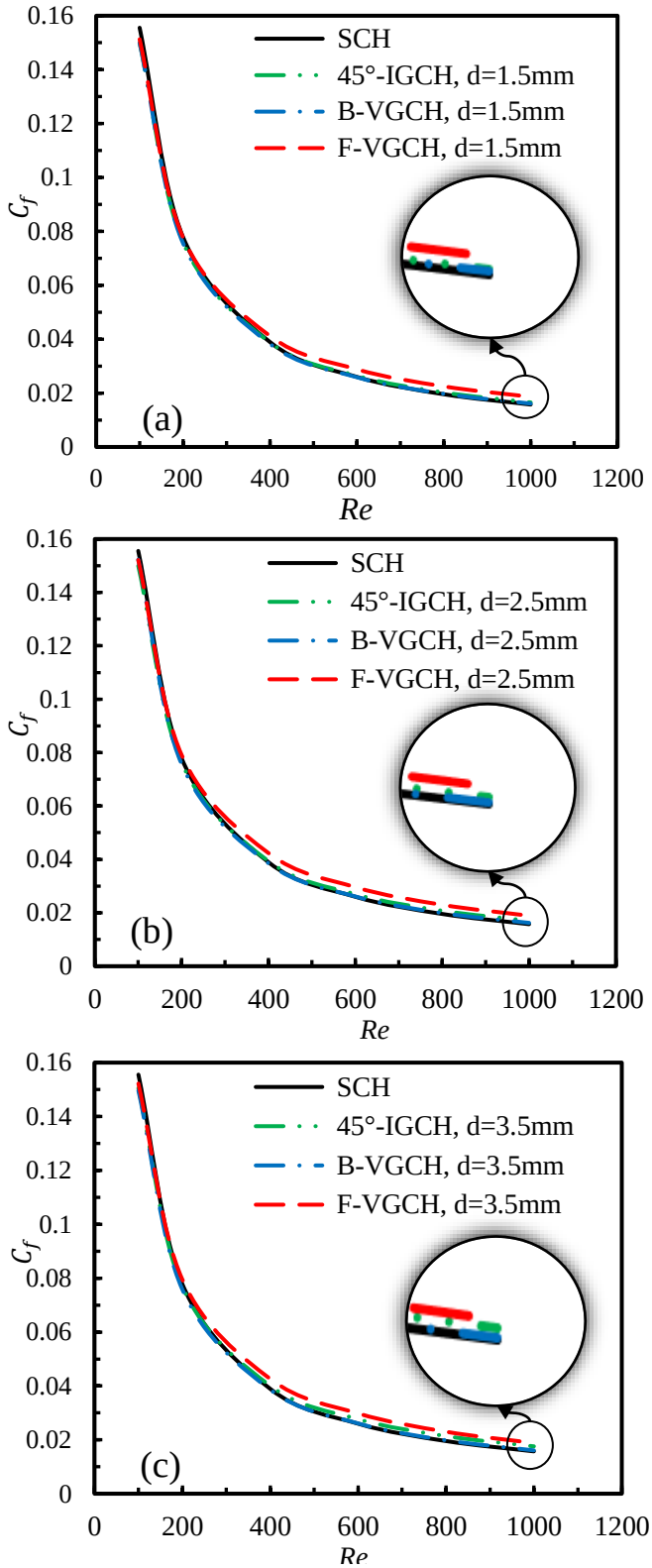

Figure 5.22: Variation of skin friction coefficient with Reynolds numbers at different groove depth: (a) d = 1.5mm, (b) d = 2.5mm, (c) d = 3.5mm

In order to explain the structure and behaviour of the fluid flow in the 45°-IGCH, Figure 5.23 provides two cross-sectional planes of velocity profile with velocity vectors, which taken place at the end of the third and fourth cycles of 45°-IGCH for 1.5 and 3.5 mm groove depths and *Re* = 1000. The axial location of each cross-sectional plane is marked by a red line, as illustrated in Figure 5.23. The velocity vectors are projected on the cross-sections on the third and fourth cycles. It can be observed that the secondary flows are stretching and folding around the grooves. In addition, the direction of these secondary flows is inclined with the tilted direction of the grooves. The secondary flows are axially reversed with the grooves in the other direction, i.e., flipping the flow direction over the grooves at the end of each cycle. These secondary flows are working to reduce the hydraulic boundary layer. As the depth of the groove increased, the intensity of secondary flows increases over the grooves. The generated secondary flows are working to change the shape of the velocity profile from the underside (near the grooved wall) and thus enhance the mixing of the fluid.

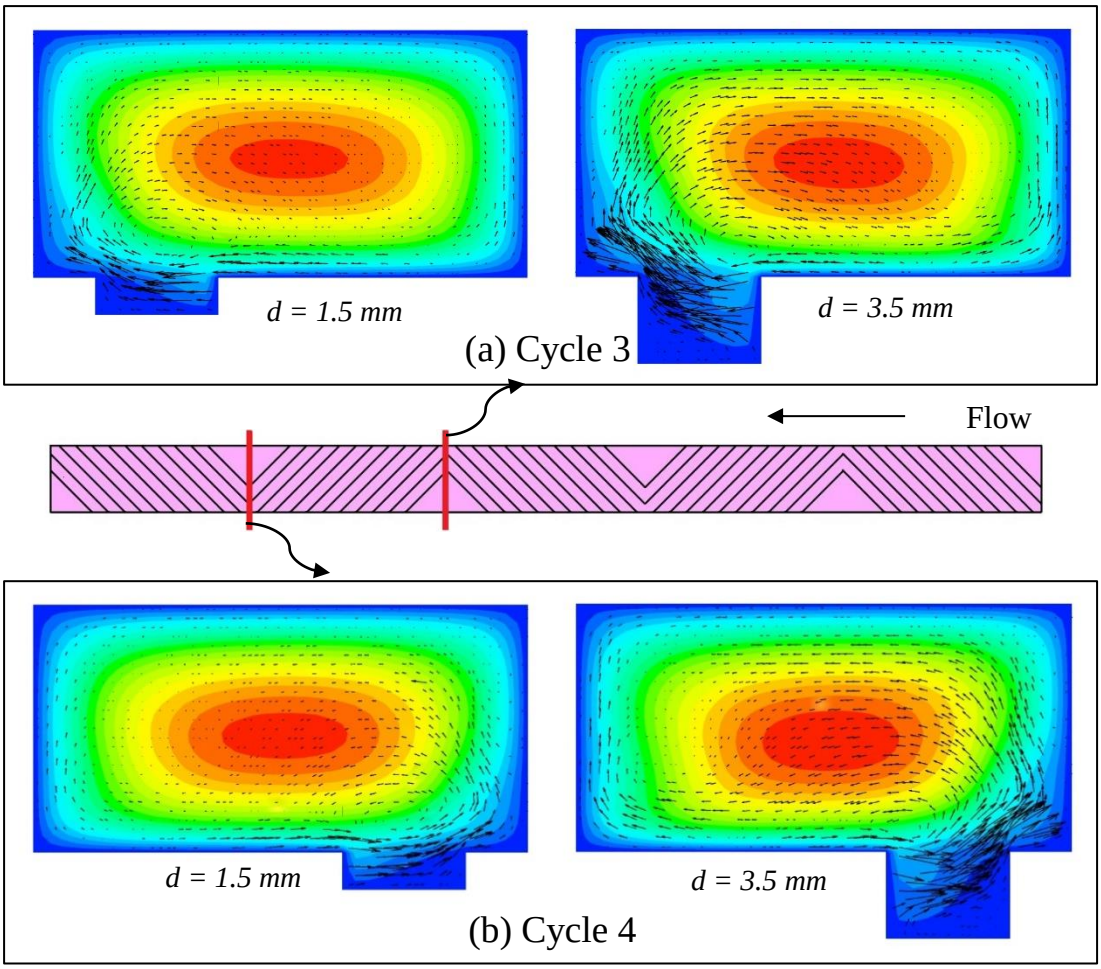

Figure 5.23: Velocity profile with velocity vectors for 45°-IGCH at *Re* = 1000. (a) After cycle No.3 at d = 1.5, and 3.5 mm, (b) After cycle No.4 at *d* = 1.5, and 3.5 mm

In order to explain the structure and behaviour of the fluid flow in the B-VGCH, Figure 5.24 provides two cross-sectional planes of velocity profile with velocity vectors, which taken at the end of the third and fourth cycles of B-VGCH for 1.5 and 3.5 mm groove depths and *Re* = 1000. The axial location of each cross-sectional plane is marked by a red line, as illustrated in Figure 5.24. The velocity vectors are projected on the cross-sectional planes on the third and fourth cycles. It can be observed that two groups of generated secondary flows inside each groove and these secondary flows stretching and folding over. In B-VGCH, there are two counter-rotating vortices around each groove that tilted its direction from both sides of the channel towards the center from the bottom in the streamwise

direction for the axial flow. As the depth of the groove increased, the intensity of secondary flows increases over the grooves. These generated secondary flows are working to reduce the hydraulic boundary layer then change the shape of the velocity profile from the underside (near the center of the grooved wall) and thus enhance the mixing of the fluid.

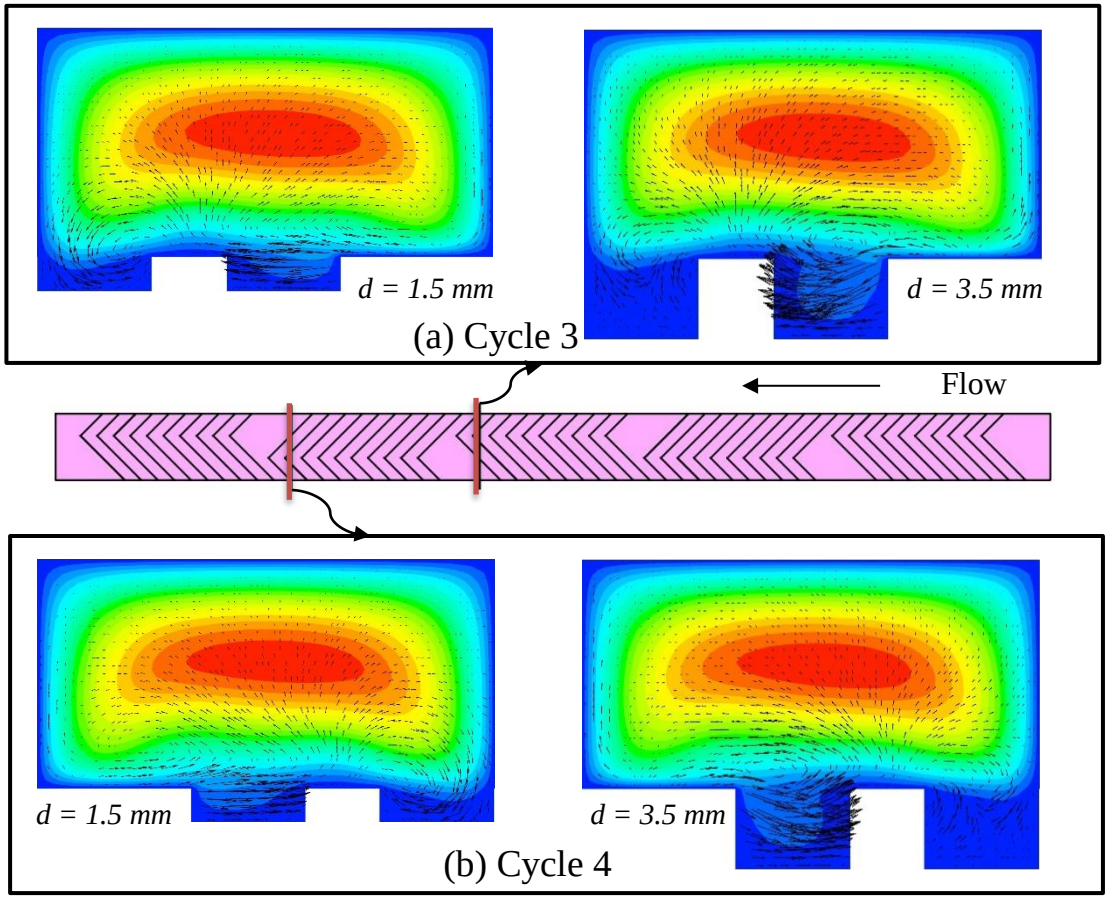

Figure 5.24: Velocity profile with velocity vectors for B-VGCH at *Re* = 1000. (a) After cycle No.3 at d = 1.5, and 3.5 mm, (b) After cycle No.4 at *d* = 1.5, and 3.5 mm

Figure 5.25 provides two cross-sectional planes of the flow velocity at the end of the third and fourth cycles for F-VGCH with 1.5, and 3.5 mm groove depths. The axial location of each cross-sectional plane is stated by a red line, as shown in Figure 5.25. The velocity vectors are projected on the cross-sectional planes on the third and fourth cycles. It can be observed that two groups of generated secondary flows are created inside

each groove and these secondary flows are stretching and folding. Therefore, the secondary flows form two counter-rotating vortices in each groove tilted their directions from the center of the channel toward both sides from the bottom surface. At the end of each cycle, these groups of the generated secondary flow are axially reversed within the opposite groove direction in other words the generated secondary flows are flipping the main flow direction over. As the depth of groove increase, the intensity of secondary flows increases as well over the grooves. These generated secondary flows are working to reduce the hydraulic boundary layer and change the velocity profiles from the two sides toward the side-walls and thus enhance the mixing of the fluid. Also, it can be seen that, in F-VGCH, a considerable fluid mixing occurs in comparison with the B-VGCH and 45˚-IGCH, as depicted in Figures 5.23, 5.24, 5.25.

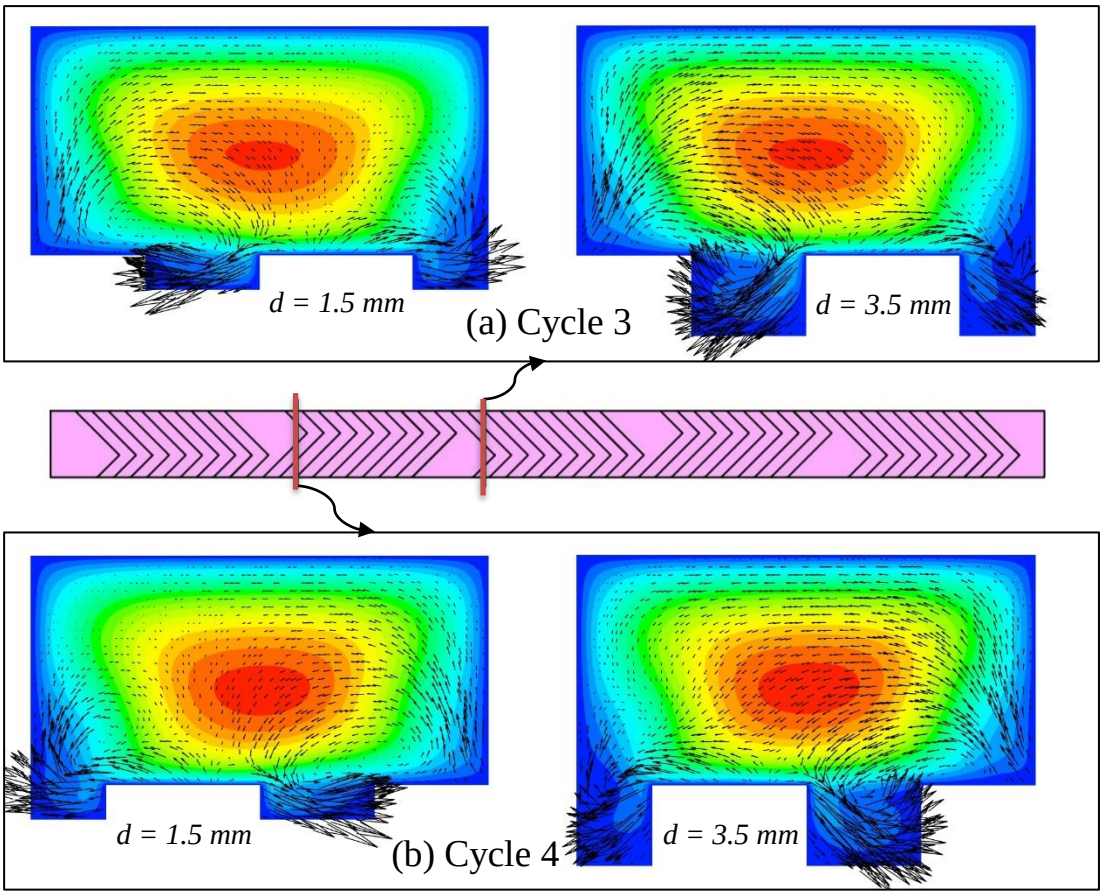

Figure 5.25: Velocity profile with velocity vectors for F-VGCH at *Re* = 1000. (a) After cycle No.3 at *d* = 1.5, and 3.5 mm, (b) After cycle No.4 at *d* = 1.5, and 3.5 mm

5.4.2.2 Characteristics of Heat Transfer

Figure 5.26 shows the variation in the averaged Nusselt number versus Reynolds numbers for grooved channels with different groove depths (*d=1.5, 2.5, and 3.5 mm*). It can be seen that the depth of grooves can notably affect the averaged Nusselt numbers over the entire range of Reynolds numbers. The averaged Nusselt number increases with the increase of groove depths for all groove shapes and the variation of increase varies from one shape to another. This is happened as a result of the generated secondary flows that appears within the grooves and hence enhances the mixing of fluid and heat transfer rate. For *1.5mm* groove depth the highest value of the averaged Nusselt number is for F-VGCH followed by B-VGCH and 45°-IGCH, respectively, where the lowest

value is for SCH, as illustrated in Figure 5.26(a). However, the value of the averaged Nusselt number for 45°-IGCH is significantly raised with the increase of the groove depths, especially at *3.5mm* groove depth (see Figure 5.26 (c)), where the value of the averaged Nusselt number becomes higher than the B-VGCH, especially at high Reynolds number (*Re* ≥ *600*). Further, the highest value of the averaged Nusselt number remains for F-VGCH compared with 45°-IGCH and B-VGCH. Therefore, it can be said that F-VGCH has great heat transfer efficiency for different groove depths because of efficient mixing of fluid, and the improvement degree is varied with the rise of the Reynolds numbers. For example, for *1.5 mm* groove depth and *Re = 100*, the $\overline{Nu}_{,G}/\overline{Nu}_{,S}$ of F-VGCH, B-VGCH and 45°-IGCH is 1.26, 1.10 and 1.06, respectively, whereas for *Re = 1000*, the $\overline{Nu}_{,G}/\overline{Nu}_{,S}$ of F-VGCH, B-VGCH and 45°-IGCH is 2.22, 1.81 and 1.43, respectively. Additionally, for *3.5 mm* groove depth and *Re = 100*, the $\overline{Nu}_{,G}/\overline{Nu}_{,S}$ of F-VGCH, B-VGCH and 45°-IGCH is 1.62, 1.27 and 1.25, respectively, whereas for *Re = 1000*, the $\overline{Nu}_{,G}/\overline{Nu}_{,S}$ of F-VGCH, B-VGCH and 45°-IGCH is 2.32, 1.75 and 1.92, respectively.

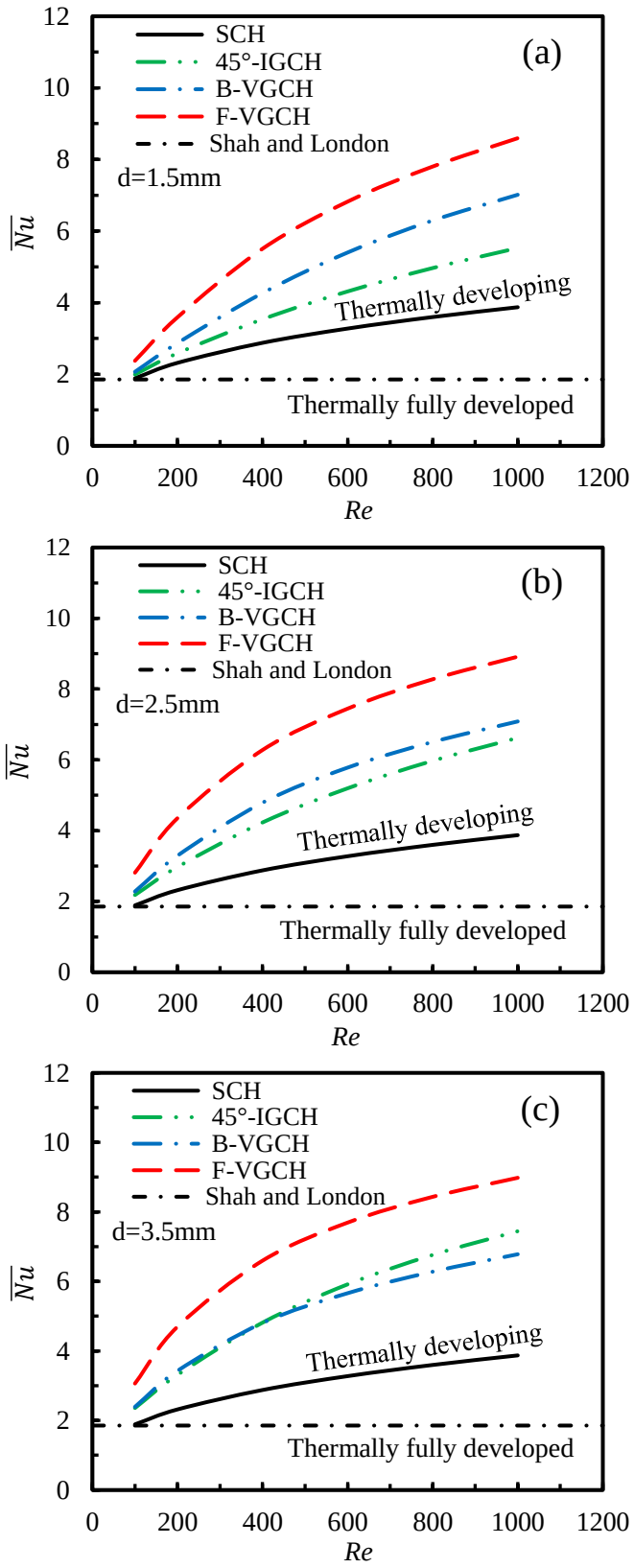

Figure 5.26: Variation of average Nusselt number with Reynolds numbers at different groove depth: (a) d = 1.5mm, (b) d = 2.5mm, (c) d = 3.5mm

5.3.2.3. The Performance Evaluation Criterion (PEC)

Figure 5.27 illustrates the variations in the *PEC* versus Reynolds numbers for different groove depths that printed on the bottom wall of the grooved channels. The variation in the groove depths is significantly affected the performance evaluation criterion over the entire range of Reynolds number. According to Figure 5.27, it can be noted that the PEC for all V-grooved channels with different groove depths and Reynolds number is higher than unity, which means there is a remarkable enhancement in the heat transfer $\left(\overline{Nu}_{,G}/\overline{Nu}_{,S}\right)$ as compared with the penalty of skin friction coefficient ratio $\left(C_{f,G}/C_{f,S}\right)$. For 1.5 mm groove depths, 45°-IGCH provides the lowest performance evaluation criterion over Reynolds numbers range compared with the other grooved channels, while, the maximum value of *PEC* is 1.404 at *Re* = 1000. As the groove depths increase, the *PEC* of 45°-IGCH is significantly changed with Reynolds number and the maximum value of *PEC* become 1.852 at *Re* = 1000 , while the *PEC* of B-VGCH with 3.5 mm groove depth is lower than that of 1.5 and 2.5 mm groove depths. Therefore, it is not necessary the *PEC* increases with increasing the groove depth because both the average Nusselt number augmentation and the skin friction coefficient are proportional with the groove depths. It can be seen that the maximum *PEC* occurs at F-VGCH compared with the other grooved channels at different groove depths because the augmentation of the averaged Nusselt number is higher than the increase of skin friction coefficient and the peak value of F-VGCH is 2.244 at *Re* = 600 and *d* = 3.5 mm. Therefore, it can be said that the F-VGCH provides the best performance evaluation criterion.

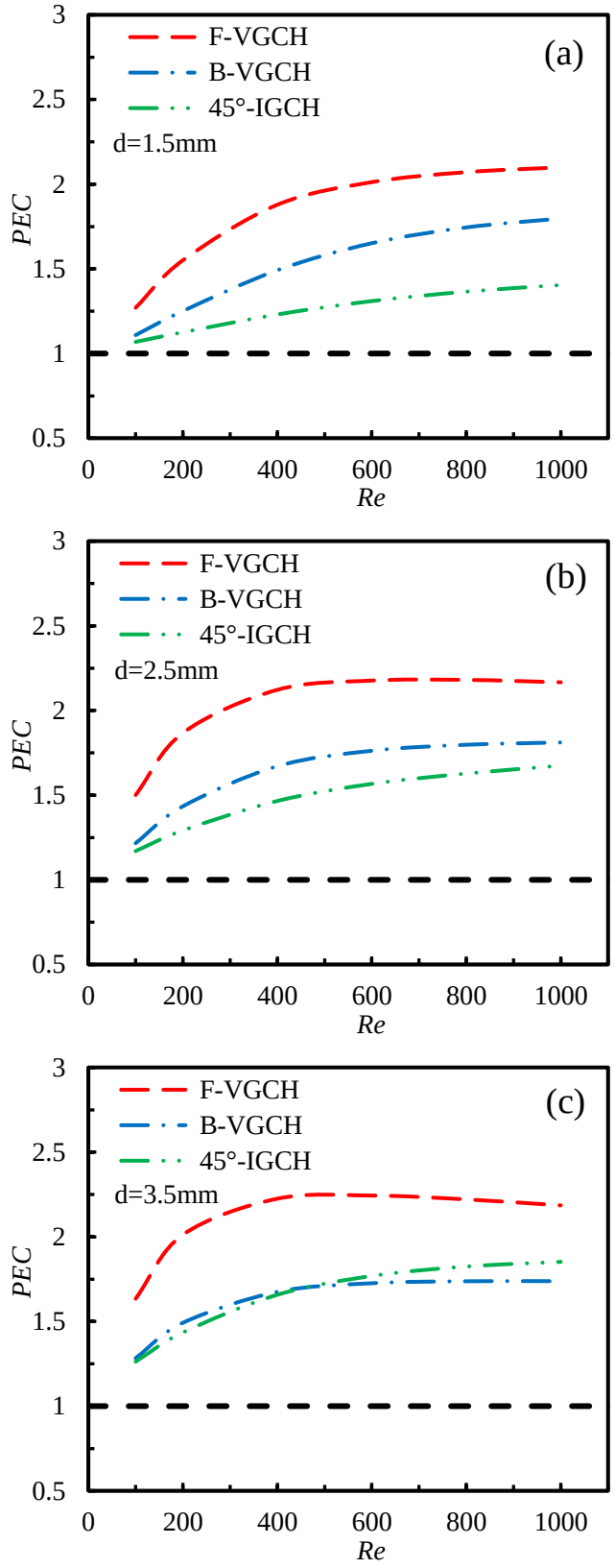

Figure 5.27: Variation of average performance evaluation criterion with Reynolds numbers at different groove depth: (a) d = 1.5mm, (b) d = 2.5mm, (c) d = 3.5mm

CHAPTER SIX

CONCLUSIONS AND RECOMMENDATIONS

CHAPTER SIX
CONCLUSIONS AND RECOMMENDATIONS

6.1 Conclusions

A combined experimental and numerical studies have been performed to investigate the convective heat transfer characteristics of fully-developed laminar forced flow in a rectangular channel fitted with inclined and V-shaped grooves. Three different shapes of grooved channel were systematically examined to assess hydrothermal performance in the range of Reynolds numbers of 100-1000 with 15000 W/m^2 applied heat flux on the bottom surface of grooved channels. Moreover, a numerical model was executed to simulate steady-state laminar flow and heat transfer in the rectangular V-grooved channels to be identical to those used in the performed experiments. The conservation equations (continuity, momentum and energy) were solved by using a commercial software package ANSYS FLUENT-CFD Version 2020R1 Code with the necessary boundary conditions to simulate the experimental setup. A comparison between the experimental results and the numerical data was achieved and it showed a good agreement between them and the averaged deviation of skin friction coefficient and average Nusselt numbers for all grooved channels is within 8.73% and 9.13% respectively. The conclusions can be drawn from this study as follows:

1. At low Reynolds numbers (less than 200); the skin friction coefficient in the grooved channels is approximately lower than that of straight channel. This indicated that the channels with these groove shapes can reduce the friction of flow at a certain level.
2. The forward V-shape grooved channel (F-VGCH) has a relatively high efficiency of heat transfer for different groove depths because

of efficient mixing of fluid compared with 45°-IGCH and B-VGCH and the peak value of the average Nusselt numbers is 8.98 at *Re = 1000* and groove depth 3.5 mm.

3. The 45°-inclined grooved channel (45°-IGCH) shows a significant enhancement in heat transfer at high values of Reynolds numbers and groove depths and the value of average Nusselt number enhancement is 1.92 at *Re = 1000* and *d =3.5 mm* with reasonable penalty of pressure-drop.
4. Finally, the use of forward V-shape grooved channel offers the highest *PEC* as compared with other shapes of grooved channels and the peak value of *PEC* is 2.244 at *Re* = 600 and *d* = 3.5 mm.

6.2. Recommendations for Future Works

According to the numerical data and experimental results of the present study, the following recommendations may be useful for the future work in this field:

1. The current study can be extended to investigate the effect of cycle number and the number of grooves in each cycle on the performance evaluation criterion for these grooved channels.
2. The study can be extended to investigate the geometrical effects such as, groove-to-groove space and the aspect ratio of channel, on the performance evaluation criterion for these grooved channels.
3. The current study can also be extended by using unconventional fluids, for example nanofluids or non-Newtonian fluids, to enhance the rate of heat transfer in these grooved channels in both flow regimes (laminar and turbulent).
4. The unsteady flow regime may be demonstrated for future consideration.

References

[1] A. E. Bergles, R. L. Webb, and G. H. Junkan, ‘Energy conservation via heat transfer enhancement’, *Energy*, vol. 4, no. 2. pp. 193–200, 1979, doi: 10.1016/0360-5442(79)90120-8.

[2] A. B. Ganorkar, ‘Review of heat transfer enhancement in different types of extended surfaces’, *International Journal of Science and Technology*, vol. 3, no. 4. pp. 3304–3313, 2011.

[3] S. G. Kandlikar, ‘Fundamental issues related to flow boiling in minichannels and microchannels’, *Experimental Thermal and Fluid Science*, vol. 26, no. 2–4. pp. 389–407, 2002, doi: 10.1016/S0894-1777(02)00150-4.

[4] B. Farhanieh, Č. Herman, and B. Sundén, ‘Numerical and experimental analysis of laminar fluid flow and forced convection heat transfer in a grooved duct’, *Int. J. Heat Mass Transf.*, vol. 36, no. 6, pp. 1609–1617, 1993, doi: 10.1016/S0017-9310(05)80070-5.

[5] A. Yutaka, N. Hiroshi, and M. Faghri, ‘Heat transfer and pressure drop characteristics in a corrugated duct with rounded corners’, *Int. J. Heat Mass Transf.*, vol. 31, no. 6, pp. 1237–1245, Jun. 1988, doi: 10.1016/0017-9310(88)90066-X.

[6] B. W. Webb and S. Ramadhyani, ‘Conjugate heat transfer in a channel with staggered ribs’, *Int. J. Heat Mass Transf.*, vol. 28, no. 9, pp. 1679–1687, 1985, doi: 10.1016/0017-9310(85)90142-5.

[7] K. M. Kelkar and S. V. Patankar, ‘Numerical Prediction of Flow and Heat Transfer in a Parallel Plate Channel With Staggered Fins’, *J. Heat Transfer*, vol. 109, no. 1, pp. 25–30, Feb. 1987, doi: 10.1115/1.3248058.

[8] H. Huang, Y. Bian, Y. Liu, F. Zhang, H. Arima, and Y. Ikegami, ‘Numerical and experimental analysis of heat transfer enhancement and pressure drop characteristics of laminar pulsatile flow in grooved channel with different groove lengths’, *Appl. Therm. Eng.*, vol. 137, pp. 632–643, 2018, doi: 10.1016/j.applthermaleng.2018.04.013.

[9] E. H. Ridouane and A. Campo, ‘Heat transfer and pressure drop characteristics of laminar air flows moving in a parallel-plate channel with transverse hemi-cylindrical cavities’, *Int. J. Heat Mass Transf.*, vol. 50, no. 19–20, pp. 3913–3924, 2007, doi: 10.1016/j.ijheatmasstransfer.2007.02.004.

[10] H. A. Lafta, ‘Numerical investigation of flow and heat transfer in a channel with different configurations and alternately order obstacles’, *Univ. Thi-Qar J.*, vol. 13, no. 1, pp. 57_73-57_73, 2018.

[11] S. Kandlikar, S. Garimella, D. Li, S. Colin, and M. R. King, *Heat transfer and fluid flow in minichannels and microchannels*. elsevier, 2005.

[12] J. T. Yang, W. F. Fang, and K. Y. Tung, ‘Fluids mixing in devices with connected-groove channels’, *Chemical Engineering Science*, vol. 63, no. 7. pp. 1871–1881, 2008, doi:

10.1016/j.ces.2007.12.027.

[13] J. T. Yang, K. J. Huang, and Y. C. Lin, ‘Geometric effects on fluid mixing in passive grooved micromixers’, *Lab Chip*, vol. 5, no. 10, pp. 1140–1147, 2005, doi: 10.1039/b500972c.

[14] C. Li and T. Chen, ‘Simulation and optimization of chaotic micromixer using lattice Boltzmann method’, *Sensors Actuators, B Chem.*, vol. 106, no. 2, pp. 871–877, 2005, doi: 10.1016/j.snb.2004.09.006.

[15] H. Wang, P. Iovenitti, E. Harvey, and S. Masood, ‘Numerical investigation of mixing in microchannels with patterned grooves’, *J. Micromechanics Microengineering*, vol. 13, no. 6, pp. 801–808, 2003, doi: 10.1088/0960-1317/13/6/302.

[16] M. J. Pattison, ‘SECONDARY FLOWS’, in *A-to-Z Guide to Thermodynamics, Heat and Mass Transfer, and Fluids Engineering*, Begellhouse, 2015.

[17] D. J. Acheson, ‘Elementary Fluid Dynamics’, *J. Acoust. Soc. Am.*, vol. 89, no. 6, pp. 3020–3020, Jun. 1991, doi: 10.1121/1.400751.

[18] J. R. Holton, ‘An introduction to dynamic meteorology’, *Am. J. Phys.*, vol. 41, no. 5, pp. 752–754, 1973, doi: doi.org/10.1119/1.1987371.

[19] J. M. Kay, R. M. Nedderman, and R. M. Nedderman, *Fluid mechanics and transfer processes*. CUP Archive, 1985.

[20] L. Prandtl, ‘Essentials of fluid dynamics: with applications to hydraulics, aeronautics, meteorology and other subjets’, 1953, doi: DOI: 10.1002/qj.49707934225.

[21] A. D. Stroock, S. K. W. Dertinger, A. Ajdari, I. Mezić, H. A. Stone, and G. M. Whitesides, ‘Chaotic mixer for microchannels’, *Science (80-.).*, vol. 295, no. 5555, pp. 647–651, 2002, doi: 10.1126/science.1066238.

[22] Q. Zhao, D. Yuan, J. Zhang, and W. Li, ‘A review of secondary flow in inertial microfluidics’, *Micromachines*, vol. 11, no. 5, p. 461, 2020, doi: doi.org/10.3390/mi11050461.

[23] ANSYS, ‘Ansys Fleunt Teory Guide, Release 17.1’, *Tech. Rep. April , ANSYS*, 2016.

[24] B. Sundén and T. Sköldheden, ‘Heat transfer and pressure drop in a new type of corrugated channels’, *Int. Commun. Heat Mass Transf.*, vol. 12, no. 5, pp. 559–566, Sep. 1985, doi: 10.1016/0735-1933(85)90079-X.

[25] C. Herman and E. Kang, ‘Heat transfer enhancement in a grooved channel with curved vanes’, *Int. J. Heat Mass Transf.*, vol. 45, no. 18, pp. 3741–3757, 2002, doi: 10.1016/S0017-9310(02)00092-3.

[26] S. Eiamsa-ard and P. Promvonge, ‘Thermal characteristics of turbulent rib-grooved channel flows’, *Int. Commun. Heat Mass Transf.*, vol. 36, no. 7, pp. 705–711, 2009, doi: 10.1016/j.icheatmasstransfer.2009.03.025.

[27] A. D. Stroock and G. J. McGraw, ‘Investigation of the staggered herringbone mixer with a simple analytical model’, *Philos. Trans. R. Soc. A Math. Phys. Eng. Sci.*, vol. 362, no. 1818, pp. 971–986, 2004, doi: 10.1098/rsta.2003.1357.

[28] N. S. Lynn and D. S. Dandy, ‘Geometrical optimization of helical flow in grooved micromixers’, *Lab Chip*, vol. 7, no. 5, pp. 580–587, 2007, doi: 10.1039/b700811b.

[29] S. I., T. G., B. G., and V. J., ‘Optimization of a Bottom Grooved Micromixer Design’, in *Proceedings of the 8th International Conference on Multi-Material Micro Manufacture*, 2011, pp. 196–200, doi: 10.3850/978-981-07-0319-6_233.

[30] T. J. Kwak, Y. G. Nam, M. A. Najera, S. W. Lee, J. R. Strickler, and W. J. Chang, ‘Convex grooves in staggered herringbone mixer improve mixing efficiency of laminar flow in microchannel’, *PLoS One*, vol. 11, no. 11, 2016, doi: 10.1371/journal.pone.0166068.

[31] M. E. Taslim, T. Li, and D. M. Kercher, ‘Experimental Heat Transfer and Friction in Channels Roughened With Angled, V-Shaped and Discrete Ribs on Two Opposite Walls’, in *Volume 4: Heat Transfer; Electric Power; Industrial and Cogeneration*, Jun. 1994, vol. 78866, p. V004T09A018, doi: 10.1115/94-GT-163.

[32] P. Promvonge and S. Kwankaomeng, ‘Periodic laminar flow and heat transfer in a channel with 45° staggered V-baffles’, *Int. Commun. Heat Mass Transf.*, vol. 37, no. 7, pp. 841–849, 2010, doi: 10.1016/j.icheatmasstransfer.2010.04.002.

[33] W. Peng, P. X. Jiang, Y. P. Wang, and B. Y. Wei, ‘Experimental and numerical investigation of convection heat transfer in channels with different types of ribs’, *Appl. Therm. Eng.*, vol. 31, no. 14–15, pp. 2702–2708, 2011, doi: 10.1016/j.applthermaleng.2011.04.040.

[34] P. Promvonge, W. Jedsadaratanachai, S. Kwankaomeng, and C. Thianpong, ‘3D simulation of laminar flow and heat transfer in V-baffled square channel’, *Int. Commun. Heat Mass Transf.*, vol. 39, no. 1, pp. 85–93, 2012, doi: 10.1016/j.icheatmasstransfer.2011.09.004.

[35] B. V. Ravi, P. Singh, and S. V. Ekkad, ‘Numerical investigation of turbulent flow and heat transfer in two-pass ribbed channels’, *Int. J. Therm. Sci.*, vol. 112, pp. 31–43, 2017, doi: 10.1016/j.ijthermalsci.2016.09.034.

[36] W. Jedsadaratanachai and A. Boonloi, ‘Effects of blockage ratio and pitch ratio on thermal performance in a square channel with 30° double V-baffles’, *Case Stud. Therm. Eng.*, vol. 4, pp. 118–128, 2014, doi: 10.1016/j.csite.2014.08.002.

[37] P. Promvonge and S. Skullong, ‘Heat transfer in solar receiver heat exchanger with combined punched-V-ribs and chamfer-V-grooves’, *Int. J. Heat Mass Transf.*, vol. 143, p. 118486, 2019, doi: 10.1016/j.ijheatmasstransfer.2019.118486.

[38] D. Jansangsuk, C. Khanoknaiyakarn, and P. Promvonge, ‘Experimental study on heat transfer and pressure drop in a channel with triangular v-ribs’, *Proc. Int. Conf. Energy Sustain. Dev. Issues*

Strateg. ESD 2010, 2010, doi: 10.1109/esd.2010.5598855.

[39] C. W. Leung, S. Chen, T. T. Wong, and S. D. Probert, 'Forced convection and pressure drop in a horizontal triangular-sectional duct with V-grooved (i.e. orthogonal to the mean flow) inner surfaces', *Appl. Energy*, vol. 66, no. 3, pp. 199–211, 2000, doi: 10.1016/S0306-2619(99)00130-0.

[40] P. Promvonge, P. Tongyote, and S. Skullong, 'Thermal behaviors in heat exchanger channel with V-shaped ribs and grooves', *Chem. Eng. Res. Des.*, vol. 150, pp. 263–273, 2019, doi: 10.1016/j.cherd.2019.07.025.

[41] T. Alam, R. P. Saini, and J. S. Saini, 'Experimental investigation on heat transfer enhancement due to V-shaped perforated blocks in a rectangular duct of solar air heater', *Energy Convers. Manag.*, vol. 81, pp. 374–383, 2014, doi: 10.1016/j.enconman.2014.02.044.

[42] Fanghao Yang, M. Alwazzan, Wenming Li, and Chen Li, 'Single- and Two-Phase Thermal Transport in Microchannels With Embedded Staggered Herringbone Mixers', *J. Microelectromechanical Syst.*, vol. 23, no. 6, pp. 1346–1358, Dec. 2014, doi: 10.1109/JMEMS.2014.2313314.

[43] J. Marschewski, R. Brechbühler, S. Jung, P. Ruch, B. Michel, and D. Poulikakos, 'Significant heat transfer enhancement in microchannels with herringbone-inspired microstructures', *International Journal of Heat and Mass Transfer*, vol. 95. pp. 755–764, 2016, doi: 10.1016/j.ijheatmasstransfer.2015.12.039.

[44] P.-S. Lee and C.-J. Teo, ‘Heat Transfer Enhancement in Microchannels Incorporating Slanted Grooves’, in *ASME 2008 First International Conference on Micro/Nanoscale Heat Transfer, Parts A and B*, Jan. 2008, vol. PART A, no. 65, pp. 819–823, doi: 10.1115/MNHT2008-52374.

[45] J. D. Anderson and J. Wendt, *Computational fluid dynamics*, vol. 206. Springer, 1995.

[46] F. M. White, ‘Fluid Mechanics 8th in SI units’, *Journal of Visual Languages & Computing*, vol. 11. p. 864, 2000.

[47] T. L. Bergman, A. Lavine, F. P. Incropera, and D. P. Dewitt, *Fundamentals of heat and mass transfer*. John Wiley & Sons New York, 2017.

[48] R. L. Webb and N.-H. Kim, *Principles of Enhanced Heat Transfer*. Taylor and Francis, NY, 2005.

[49] J. P. Holman, *Experimental methods for engineers*. 2001.

[50] S. J. Kline, ‘McClintock (1953)’, *Descr. Uncertainties Single-Sample*.

[51] Shah R and London A, ‘Laminar flow forced convection heat transfer and flow friction in straight and curved ducts. A summary of analytical solutions’, *Stanford Univ*. 1971.

[52] T. D. Bennett, ‘Laminar convection in rectangular ducts of fully

developed flow', *Int. J. Heat Mass Transf.*, vol. 156, 2020, doi: 10.1016/j.ijheatmasstransfer.2020.119846.

[53] P. S. Lee and S. V. Garimella, 'Thermally developing flow and heat transfer in rectangular microchannels of different aspect ratios', *Int. J. Heat Mass Transf.*, vol. 49, no. 17–18, pp. 3060–3067, 2006, doi: 10.1016/j.ijheatmasstransfer.2006.02.011.

[54] W. M. Abed, R. D. Whalley, D. J. C. Dennis, and R. J. Poole, 'Numerical and experimental investigation of heat transfer and fluid flow characteristics in a micro-scale serpentine channel', *Int. J. Heat Mass Transf.*, vol. 88, pp. 790–802, 2015, doi: 10.1016/j.ijheatmasstransfer.2015.04.062.

APPENDICES

Appendix A

Appendix A
CALIBRATION OF MEASURING INSTRUMENTS

A1. Calibration of the Temperature Recorders and Thermocouples

Calibration of the temperature recorders and thermocouples was carried out by immersing the tip of these 10 thermocouples together with accurate mercury bulb thermometer inside a mixture of distilled water and crushed ice. At the ice bath temperature and in the same water at boiling temperature, the water temperature was recorded in the range of (0 °C and 100 °C) respectively. The calibration curve is shown in Figure (A.1). The maximum error of reading found about ±1.98 %.

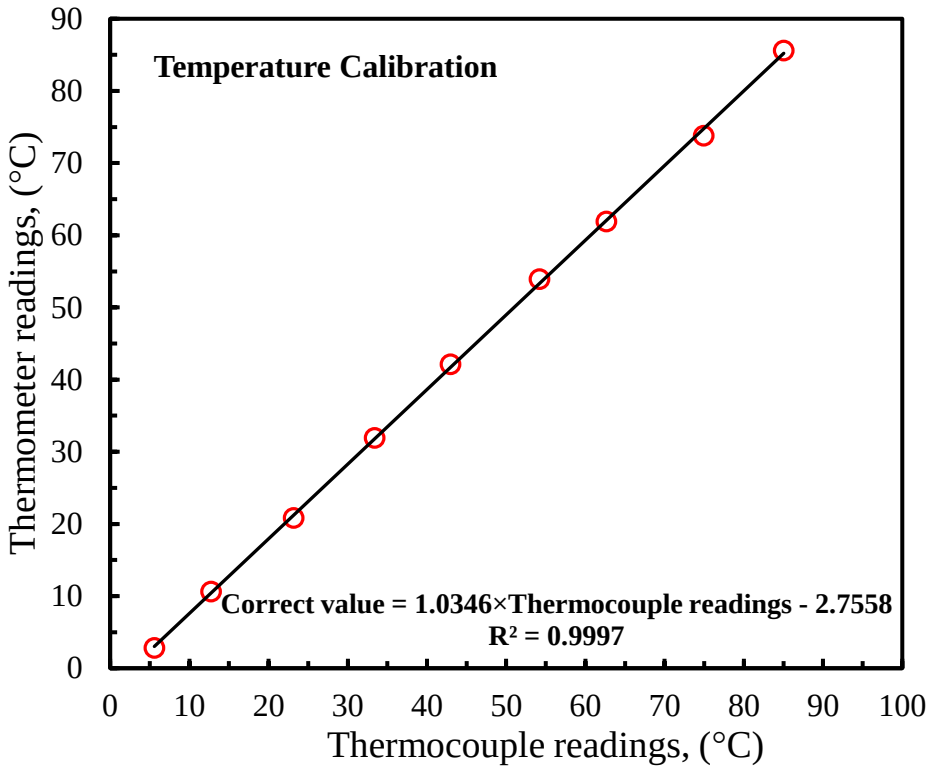

Figure (A.1) Calibration curve of thermocouples

A2. Calibration of the Flow Meters

The digital flowmeter is calibrated with a standard precision-machined acrylic flowmeter for water of accuracy (±0.25 FS) in the range of flow rate from 0.2 L/min to 2.0 L/min. An accuracy of ±5% is found in the flow rate calibration experiments. Flow meter calibration curve is shown in Figure (A.2).

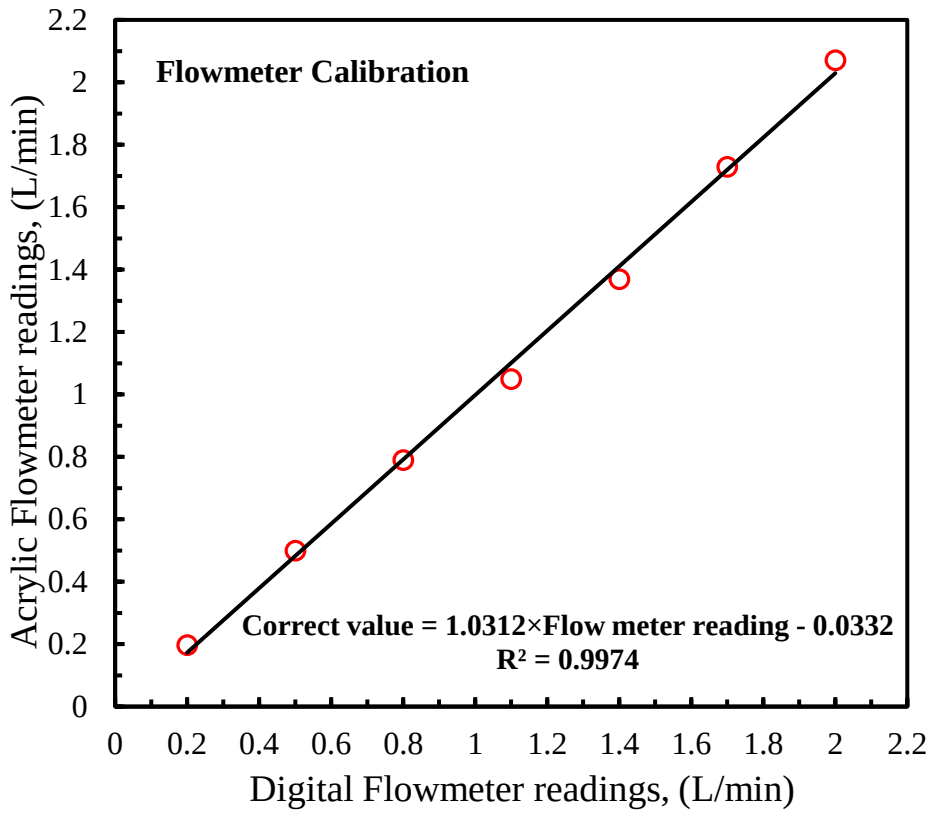

Figure (A.4) Calibration curve of Digital Flowmeter

A3. Calibration of AC Power Monitor

The AC Power Monitor was calibrated in the laboratories of engineering college, department of electrical engineering at University of Anbar. Current calibration curve is shown in Figure (A.3) and the calibration curve of voltage is shown in Figure (A.4). Maximum error of reading found about of ± 4.9% and ±0.07% for current and voltage respectively.

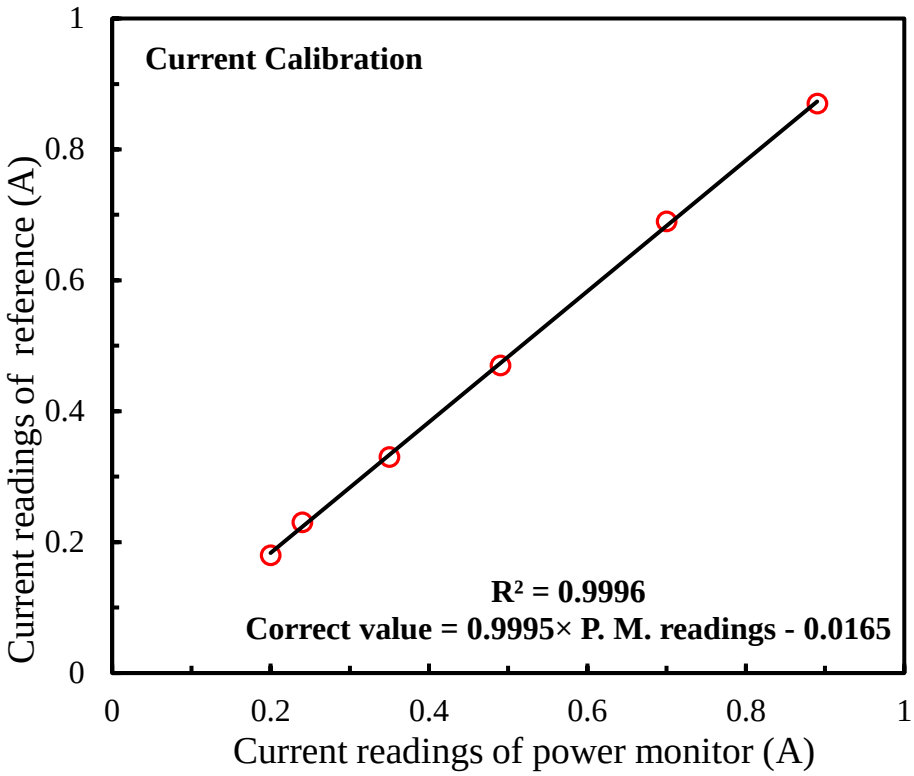

Figure (A.3) Calibration curve of power monitor Current

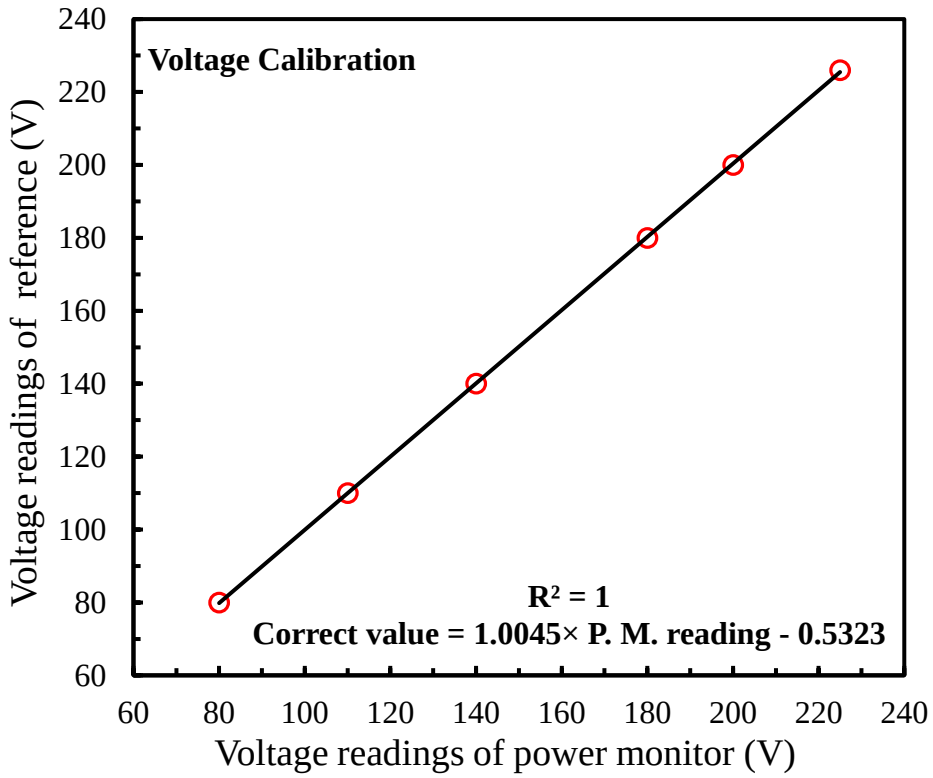

Figure (A.4) Calibration curve of power monitor Voltage

Appendix B

Appendix B
UNCERTAINTIES ANALYSIS PROCEDURE

The uncertainties for key different parameters are given in below table.

Table B.1: Uncertainty values for measured parameters.

No.	Parameter	Uncertainty values
1	The height of channel, H	±0.1mm
2	The width of channel, W	±0.1mm
3	The length of channel, L	±1mm
4	Inlet bulk temperature, $T_{b,in}$	±1.98%
5	Outlet bulk temperature, $T_{b,out}$	±1.98%
6	Surface temperature, $T_{S,av}$	±1.98%
7	Mass flow rate, $\dot{m}$	±5%
8	Pressure drop, ΔP	±9.2%.

Surface Area:

The uncertainty of the surface area for a grooved channel is calculated as:

$$A_s = WL \qquad (B.1)$$

Partial derivation with respect to W and L gives,

$\frac{\partial A_s}{\partial W} = L$ and $\frac{\partial A_s}{\partial L} = W$; Substituting these partial derivations in Eq. 4.8 gives,

$$U_{A_s} = \pm\sqrt{\left(\frac{\partial A_s}{\partial W}U_W\right)^2 + \left(\frac{\partial A_s}{\partial L}U_L\right)^2} = \sqrt{(LU_W)^2 + (WU_L)^2} \qquad (B.2)$$

In relative form,

$$\frac{U_{A_s}}{A_s} = \pm\sqrt{\left(\frac{U_W}{W}\right)^2 + \left(\frac{U_L}{L}\right)^2} \qquad (B.3)$$

Putting the values of W = 20mm, L = 300mm, $A_s = WL = 6000\,mm^2$, $U_W = 0.1mm$, $U_L = 1mm$ in Eqs. $(B.2)$ and $(B.3)$ the absolute and relative uncertainties in surface area are estimated to be $(U_{A_s}) = \pm 36.06$ and $U_{A_s}/A_s = \pm 0.6\%$ respectively. Other parameters are similarly calculated.

Cross Sectional Area:

The cross sectional area is calculated as follows:

$$A_c = WH \qquad (B.4)$$

Partial derivation with respect to W and H gives,

$\frac{\partial A_c}{\partial W} = H$ and $\frac{\partial A_c}{\partial H} = W$; Substituting these partial derivations in Eq. 4.8 gives,

$$U_{A_c} = \pm\sqrt{\left(\frac{\partial A_c}{\partial W}U_W\right)^2 + \left(\frac{\partial A_c}{\partial H}U_H\right)^2} = \sqrt{(HU_W)^2 + (WU_H)^2} \qquad (B.5)$$

Putting the values of $U_W = 0.1mm$, $U_H = 0.1mm$ W = 20mm, and H = 10mm in Eq. (B.5)

$$U_{A_c} = \sqrt{(10 \times 0.1)^2 + (20 \times 0.1)^2} = \pm 2.24mm^2$$

Perimeter:

The Perimeter is calculated as follows:

$$p = 2(W + H) = 2W + 2H \qquad (B.6)$$

Partial derivation with respect to W and H gives,

$\frac{\partial p}{\partial W} = 2$ and $\frac{\partial p}{\partial H} = 2$; Substituting these partial derivations in Eq. 4.8 gives,

$$U_p = \pm\sqrt{\left(\frac{\partial p}{\partial W}U_W\right)^2 + \left(\frac{\partial p}{\partial H}U_H\right)^2} = \sqrt{(2U_W)^2 + (2U_H)^2} \qquad (B.7)$$

Putting the values of $U_W = 0.1mm$, $U_H = 0.1mm$ in Eq. (B.5)

$$U_P = \sqrt{(2 \times 0.1)^2 + (2 \times 0.1)^2} = \pm 0.28mm$$

Hydraulic Diameter:

The hydraulic diameter was defined as follows:

$$D_h = 4\frac{A_c}{p} \qquad (B.8)$$

Partial derivation with respect to A_c and P gives,

$\frac{\partial D_h}{\partial A_c} = \frac{4}{p}$ and $\frac{\partial D_h}{\partial P} = \frac{-4A_c}{p^2}$; Substituting these partial derivations in Eq. 4.8 gives,

$$U_{D_h} = \pm\sqrt{\left(\frac{\partial D_h}{\partial A_c}U_{A_c}\right)^2 + \left(\frac{\partial D_h}{\partial P}U_P\right)^2} = \sqrt{\left(\frac{4}{P}U_{A_c}\right)^2 + \left(\frac{-4A_c}{P^2}U_P\right)^2} \qquad (B.9)$$

Putting the values of $P = 60mm$, $A_c = 200mm^2, U_P = 0.28mm,$ and $U_{A_c} = 2.24mm^2$

$$U_{D_h} = \pm\sqrt{\left(\frac{4}{60} \times 2.24\right)^2 + \left(\frac{-4\times200}{60^2} \times 0.28\right)^2} = \pm 0.162mm$$

Reynolds Number:

Reynolds number can be defined as follows:

$$Re = \frac{\dot{m}D_h}{\mu\, A_C} \qquad (B.10)$$

$\frac{\partial Re}{\partial \dot{m}} = \frac{D_h}{\mu\, A_C} = \frac{Re}{\dot{m}}$, $\frac{\partial Re}{\partial D_h} = \frac{\dot{m}}{\mu\, A_C} = \frac{Re}{D_h}$, and $\frac{\partial Re}{\partial A_c} = \frac{-\dot{m}D_h}{\mu\, {A_C}^2} = \frac{-Re}{A_c}$

Substituting these partial derivations in Eq. 4.8 gives,

$$U_{Re} = \pm\sqrt{\left(\frac{\partial Re}{\partial \dot{m}} U_{\dot{m}}\right)^2 + \left(\frac{\partial Re}{\partial D_h} U_{D_h}\right)^2 + \left(\frac{\partial Re}{\partial A_c} U_{A_c}\right)^2} \qquad (B.11)$$

$$\frac{U_{Re}}{Re} = \pm\sqrt{\left(\frac{U_{\dot{m}}}{\dot{m}}\right)^2 + \left(\frac{U_{D_h}}{D_h}\right)^2 + \left(\frac{-U_{A_c}}{A_c}\right)^2}$$

$$= \sqrt{\left(\frac{0.000645}{0.0129}\right)^2 + \left(\frac{0.162}{13.333}\right)^2 + \left(\frac{-2.24}{200}\right)^2} = \pm 5.26\%$$

The skin friction coefficient:

The skin friction coefficient is evaluated as:

$$C_f = \Delta P \frac{D_h}{2\rho_f U_m^2 L} = \frac{\Delta P \rho_f {A_C}^2}{2\,\dot{m}^2} \frac{D_h}{L} \qquad (B.12)$$

Where $U_m^2 = \frac{\dot{m}^2}{\rho_f{}^2 {A_C}^2}$

$\frac{\partial C_f}{\partial \Delta P} = \frac{\rho_f {A_C}^2 D_h}{2\,\dot{m}^2 L} \times \frac{\Delta P}{\Delta P} = \frac{C_f}{\Delta P}$

$\frac{\partial C_f}{\partial D_h} = \frac{\rho_f {A_C}^2 \Delta P}{2\,\dot{m}^2 L} \times \frac{D_h}{D_h} = \frac{C_f}{D_h}$

$\frac{\partial C_f}{\partial A_C} = \frac{\rho_f A_C D_h \Delta P}{\dot{m}^2 L} \times \frac{2A_C}{2A_C} = \frac{2\,C_f}{A_C}$

$\frac{\partial C_f}{\partial \dot{m}} = \frac{-\rho_f {A_C}^2 D_h \Delta P}{\dot{m}^3 L} \times \frac{2}{2} = \frac{-2\,C_f}{\dot{m}}$

$\frac{\partial C_f}{\partial L} = \frac{-\rho_f {A_C}^2 D_h \Delta P}{2\,\dot{m}^2 L^2} = \frac{-C_f}{L}$ Substituting these partial derivations in Eq. 4.8 gives,

$$U_{C_f} =$$

$$\pm\sqrt{\left(\frac{\partial C_f}{\partial \Delta P} U_{\Delta P}\right)^2 + \left(\frac{\partial C_f}{\partial D_h} U_{D_h}\right)^2 + \left(\frac{\partial C_f}{\partial A_C} U_{A_c}\right)^2 + \left(\frac{\partial C_f}{\partial \Delta P} U_{\dot{m}}\right)^2 + \left(\frac{\partial C_f}{\partial L} U_L\right)^2}$$

$$(B.13)$$

$$\frac{U_{C_f}}{C_f} = \pm\sqrt{\left(\frac{U_{\Delta P}}{\Delta P}\right)^2 + \left(\frac{U_{D_h}}{D_h}\right)^2 + \left(\frac{2U_{A_C}}{A_C}\right)^2 + \left(\frac{-2U_{\dot{m}}}{\dot{m}}\right)^2 + \left(\frac{-U_L}{L}\right)^2} \qquad (B.14)$$

$$\frac{U_{C_f}}{C_f} = \pm\sqrt{\left(\frac{0.3484}{3.787}\right)^2 + \left(\frac{0.162}{13.333}\right)^2 + \left(\frac{2\times2.24}{200}\right)^2 + \left(\frac{-2\times0.000645}{0.0129}\right)^2 + \left(\frac{-1}{300}\right)^2}$$

$$\frac{U_{C_f}}{C_f} = \pm 9.55\%$$

The heat absorbed:

The heat absorbed by flowing water is estimated by the following:

$$Q_{out} = \dot{m}\, C_{P,f}\left(T_{b,out} - T_{b,in}\right) \qquad (B.15)$$

The uncertainty of Q_{out} is expressed by:

$$U_{Q_{out}} = \pm\sqrt{\left(\frac{\partial Q_{out}}{\partial \dot{m}} U_{\dot{m}}\right)^2 + \left(\frac{\partial Q_{out}}{\partial \Delta T_b} U_{\Delta T_b}\right)^2} \qquad (B.16)$$

Where, $\frac{\partial Q_{out}}{\partial \dot{m}} = C_{P,f}\Delta T_b = \frac{Q_{out}}{\dot{m}}$; and $\frac{\partial Q_{out}}{\partial \Delta T_b} = \dot{m}\, C_{P,f} = \frac{Q_{out}}{\Delta T_b}$

The relative uncertainty of Q_{out} is evaluated as:

$$\frac{U_{Q_{out}}}{Q_{out}} = \pm\sqrt{\left(\frac{U_{\dot{m}}}{\dot{m}}\right)^2 + \left(\frac{U_{\Delta T_b}}{\Delta T_b}\right)^2} \qquad (B.17)$$

Where

$$\frac{U_{\Delta T_b}}{\Delta T_b} = \pm\sqrt{\left(\frac{U_{T_{b,in}}}{T_{b,in}}\right)^2 + \left(\frac{U_{T_{b,out}}}{T_{b,out}}\right)^2} = \pm\sqrt{\left(\frac{0.5415}{27.351}\right)^2 + \left(\frac{0.5517}{27.8685}\right)^2} = \pm 2.8\%$$

$$\frac{U_{Q_{out}}}{Q_{out}} = \pm\sqrt{\left(\frac{0.000645}{0.0129}\right)^2 + \left(\frac{0.01448}{0.5173}\right)^2} = \pm 5.73\%$$

Nusselt number:

The average Nusselt number can be given as:

$$\overline{Nu} = \bar{h}\frac{D_h}{k_f} = \frac{Q_{out}\, D_h}{k_f\, A_s\, (T_{S,av} - T_{b,av})} \qquad (B.18)$$

The uncertainty in Nusselt number is evaluated as:

$$U_{\overline{Nu}} = \pm\sqrt{\left(\frac{\partial \overline{Nu}}{\partial Q_{out}} U_{Q_{out}}\right)^2 + \left(\frac{\partial \overline{Nu}}{\partial D_h} U_{D_h}\right)^2 + \left(\frac{\partial \overline{Nu}}{\partial A_s} U_{A_s}\right)^2 + \left(\frac{\partial \overline{Nu}}{\partial T_{S,av}} U_{T_{S,av}}\right)^2 + \left(\frac{\partial \overline{Nu}}{\partial T_{b,av}} U_{T_{b,av}}\right)^2} \qquad (B.19)$$

Where

$$\frac{\partial \overline{Nu}}{\partial Q_{out}} = \frac{D_h}{k_f\, A_s\, (T_{S,av} - T_{b,av})} = \frac{\overline{Nu}}{Q_{out}}$$

$$\frac{\partial \overline{Nu}}{\partial D_h} = \frac{Q_{out}}{k_f\, A_s\, (T_{S,av} - T_{b,av})} = \frac{\overline{Nu}}{D_h}$$

$$\frac{\partial \overline{Nu}}{\partial A_s} = \frac{Q_{out}\, D_h}{k_f\, {A_s}^2\, (T_{S,av} - T_{b,av})} = \frac{-\overline{Nu}}{A_s}$$

$$\frac{\partial \overline{Nu}}{\partial T_{S,av}} = \frac{-Q_{out}\, D_h}{k_f\, A_s\, (T_{S,av} - T_{b,av})^2} = \frac{-\overline{Nu}}{T_{S,av} - T_{b,av}}$$

$$\frac{\partial \overline{Nu}}{\partial T_{b,av}} = \frac{-Q_{out}\, D_h}{k_f\, A_s\, (T_{S,av} - T_{b,av})^2} = \frac{\overline{Nu}}{T_{S,av} - T_{b,av}}$$

The relative uncertainty of Nusselt number is

$$\frac{U_{\overline{Nu}}}{\overline{Nu}} = \pm\sqrt{\left(\frac{U_{Q_{out}}}{Q_{out}}\right)^2 + \left(\frac{U_{D_h}}{D_h}\right)^2 + \left(\frac{-U_{A_s}}{A_s}\right)^2 + \left(\frac{-U_{T_{S,av}}}{T_{S,av} - T_{b,av}}\right)^2 + \left(\frac{U_{T_{b,av}}}{T_{S,av} - T_{b,av}}\right)^2} \qquad (B.20)$$

Where

$$\frac{U_{T_{b,av}}}{T_{b,av}} = \pm\sqrt{\left(\frac{U_{T_{b,in}}}{T_{b,in}}\right)^2 + \left(\frac{U_{T_{b,out}}}{T_{b,out}}\right)^2} = \pm\sqrt{\left(\frac{0.5415}{27.351}\right)^2 + \left(\frac{0.5517}{27.8685}\right)^2} =$$

$\pm 2.8\%$

$$\frac{U_{\overline{Nu}}}{\overline{Nu}} =$$

$$\pm\sqrt{\left(\frac{1.599}{27.914}\right)^2+\left(\frac{0.162}{13.333}\right)^2+\left(\frac{-36.06}{6000}\right)^2+\left(\frac{-0.7959}{40.1975-27.6099}\right)^2+\left(\frac{0.7731}{40.1975-27.6099}\right)^2}$$

$$\frac{U_{\overline{Nu}}}{\overline{Nu}} = \pm 10.599\%$$

Appendix C

Appendix C
CODE PROGRAM OF MEASURING INSTRUMENTS

C1. Code program of the Flow Meters

This digital meter has a flow sensor, turbine wheel, which rotates as the water flows from the inlet opening to the outlet opening. The turbine wheel has a magnet, which gives pulses to the Hall Effect Sensor. The flow sensor connects to the microcontroller board (Arduino Uno R3) and LCD display (LCD 16X2 Blue Backlight 5V with l2C) in order to display results and readings with a high-quality Hall Effect Sensor. The connection diagram shown in figure (C.1) and the details of programming code are depicted below:

```
#include <Wire.h <
#include <LiquidCrystal_I2C.h<
LiquidCrystal_I2C lcd(0x27,20,4);

int sensorInterrupt = 0;  // interrupt 0
int sensorPin       = 2; //Digital Pin 2
int solenoidValve = 5; // Digital pin 5
unsigned int SetPoint = 400; //400 milileter

float calibrationFactor = 90 ;

volatile byte pulseCount =0  ;
float flowRate = 0.0;
unsigned int flowMilliLitres =0;
unsigned long totalMilliLitres = 0;
unsigned long oldTime = 0;

void setup()
}
 lcd.init();                    // initialize the lcd
    lcd.backlight;()
  Serial.begin;(9600)
  pinMode(solenoidValve , OUTPUT);
  digitalWrite(solenoidValve, HIGH);
  pinMode(sensorPin, INPUT);
```

```
 digitalWrite(sensorPin, HIGH);

attachInterrupt(sensorInterrupt, pulseCounter, FALLING);

{

void loop()
}

  if((millis() - oldTime) > 1000)
 }

   detachInterrupt(sensorInterrupt);


   flowRate = ((1000.0 / (millis() - oldTime)) * pulseCount) / calibrationFactor;


   oldTime = millis;()


   flowMilliLitres = (flowRate / 60) * 1000;
totalMilliLitres += flowMilliLitres;
   unsigned int frac;

    lcd.clear;()
   Serial.print("Flow rate: ");
  lcd.print("F.R:");
  lcd.print(flowMilliLitres, DEC);
   Serial.print(flowMilliLitres, DEC);  // Print the integer part of the variable
   Serial.print("mL/Second");
   lcd.print("mL/Sec");
   Serial.print("\t")          ;

//    Print the cumulative total of litres flowed since starting
    lcd.setCursor;(0,1)
    lcd.print("vol.");
   Serial.print("Output Liquid Quantity: ") ;
   lcd.print(totalMilliLitres,DEC)       ;
  Serial.print(totalMilliLitres,DEC);
   lcd.print("mL");
   Serial.println("mL") ;
  Serial.print("\t")     ;

   if (totalMilliLitres > 40)
}
     SetSolinoidValve;()
{

//Reset the pulse counter so we can start incrementing again
```

```
   pulseCount = 0;

 //    Enable the interrupt again now that we've finished sending output
   attachInterrupt(sensorInterrupt, pulseCounter, FALLING);
{
{

//Insterrupt Service Routine

void pulseCounter()
}
 //  Increment the pulse counter
  pulseCount;++
{

void SetSolinoidValve()
}
  digitalWrite(solenoidValve, LOW);
{
```

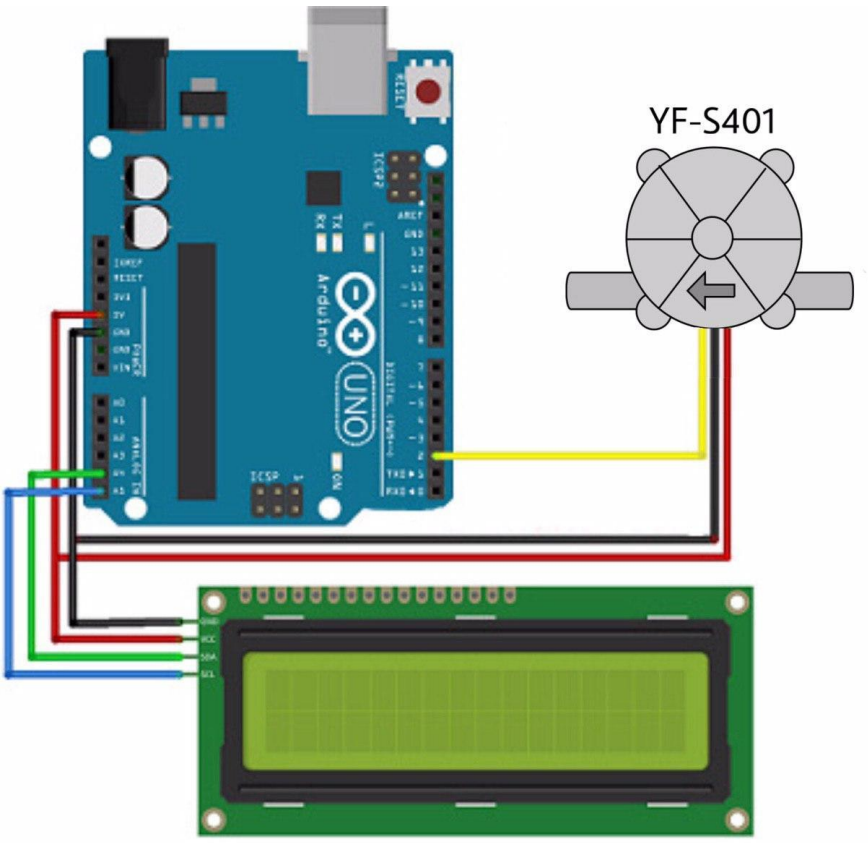

Figure (C.1) The connection diagram of Digital Flowmeter

الخلاصـــــه

تمت دراسة خصائص نقل الحرارة بالحمل للجريان الطباقي القسري كامل النمو في قناة مستطيلة مزودة بحزوز مائلة وعلى شكل حرف "V" من خلال الأساليب العددية و التجريبية. تم اختبار ثلاث اشكال مختلفة من القنوات المحززة بشكل منهجي لقياس الاداء الحراري ضمن نطاق رقم رينولدز يتراوح بين 100 الى 1000 بفيض حراري مسلط ثابت بمقدار 15000 واط / م^2 على الجدار المحزز السفلي للقناة وباستخدام الماء كسائل عمل. ايضاً تم تنفيذ نموذج عددي لمحاكاة التدفق الطباقي للحالة المستقرة في نقل الحرارة داخل القنوات المحززة (المائلة وعلى شكل حرف "V") حيث تكون مطابقة لتلك المستخدمة في التجارب العملية. تم حل المعادلات الحاكمة الرئيسية باستخدام حزمة البرنامج التجاري ANSYS FLUENT-CFD اصدار 2020R1 مع تطبيق شروط الحدود اللازمة للمحاكاة والمطابقة للتجارب العملية. تم اجراء مقارنة بين نتائج التجارب العملية مع بيانات المحاكاة العددية حيث اظهرت توافق جيد بينهما حيث كان متوسط الانحراف لمعامل احتكاك ومتوسط أرقام نسلت لجميع القنوات المحززة في حدود 8.73٪ و 9.13٪ على التوالي

أظهرت النتائج أن متوسط عدد نسلت ومقدار هبوط الضغط في جميع القنوات المحززة تزداد بزيادة رقم رينولدز بالمقارنة مع القناة الملساء المستقيمة في كل من نتائج التجارب العملية ونتائج المحاكاة العددية. عند أرقام رينولدز المنخفضة (أقل من 200) ؛ يكون معامل الاحتكاك في القنوات المحززة تقريبًا أقل من معامل الاحتكاك في القناة الملساء المستقيمة. يشير هذا إلى أن القنوات التي تحتوي على أشكال مختلفه من الحزوز، يمكن أن تقلل من الاحتكاك عند مستوى معين للتدفق. تتميز القناة ذات الحزوز على شكل حرف "V" الأمامية (F-VGCH) بكفاءة عالية نسبيًا في نقل الحرارة عند أعماق مختلفة من الحزوز بسبب الخلط الفعال للموائع مقارنة بـ -45° IGCH و B-VGCH وقيمة الذروة لمتوسط أرقام نسلت هي 8.98 عند رقم رينولدز يساوي 1000 و عمق الأخدود 3.5 ملم. تُظهر القناة ذات الحزوز المائلة بزاوية 45 درجة (-45° IGCH) تحسينًا كبيرًا في نقل الحرارة عند القيم العالية لرقم رينولدز مع مقدار معقول لانخفاض الضغط. أخيرًا ، يوفر استخدام القناة ذات الحزوز على شكل V الأمامية أعلى قيمة لمعيار تقييم الأداء (*PEC*) بالمقارنة مع الأشكال الأخرى للقنوات المحززة، وتبلغ قيمة الأعلى لمعيار تقييم الأداء (*PEC*) 2.244 عند رقم رينولدز (*Re*) يساوي 600 وعمق اخدود (*d*) يساوي 3.5 ملم.

جمهوريـــــــــة العـــــــــراق
وزارة التعليم العالي والبحث العلمي
جـامعـــة الأنبـــار- كـلـية الـهـندســة
قســـــــم الـهندســـــة الميكانيكيـــة

دراسة عددية وعملية للاداء الهيدروحراري لقناة محززة على شكل حرف "V"

رسـالة مقدمـة إلى مجـلس
كـليـة الـهندسـة – جـامعـة الأنبـار
وهي جزء من متطلبات نيل درجة الماجستير
في علوم الـهندسـة الميكانيكيـة
مـن قِبـل

سيف مهند ثابت
(بكالوريوس هندسة ميكانيكية – 2017)

بإشراف
أ.م.د. وليد محمد عبد

1442 2021